

# **Interfacing a Single Atom with Single Photons**

**Victor Leong**

*M.A.(Cantab), University of Cambridge, UK*

Department of Physics & Centre for Quantum Technologies  
National University of Singapore

This dissertation is submitted for the degree of  
*Doctor of Philosophy*

August 2016



## **Declaration**

I hereby declare that the thesis is my original work and it has been written by me in its entirety. I have duly acknowledged all the sources of information which have been used in the thesis.

The thesis has also not been submitted for any degree in any university previously.

A handwritten signature in black ink, appearing to be 'Victor Leong', written in a cursive style.

---

Victor Leong

June 2016



## Acknowledgements

This thesis is only made possible because of the painstaking investments from many people to transform me from a newbie who has never touched a proper laser nor held a soldering iron into someone who can actually do some physics without breaking everything in the lab. *Probably*. Though this thesis bears my sole name on the cover, it really is a testament to the work of all its contributors within the quantum optics group here at the Centre of Quantum Technologies.

First and foremost, credit belongs to my supervisor Christian Kurtsiefer for his leadership and guidance over the years, and being an all-in-one wise physicist, electronics guru, and affable boss.

Lots of gratitude to Syed Abdullah Aljunid and Gleb Maslennikov for teaching me everything I know when I first joined the lab. Thanks to Syed, for inducting me into the wonderful world of programming in C, Bash, awk, and sed (those one-liner code snippets are simply unparalleled time savers); and Gleb, for being patient and encouraging in his typical Russian style. Besides, they did such a great job in building the current iteration of the setup that I have never had to open up the vacuum system over the entire course of my PhD.

Thanks to Matthias Steiner and Sandoko Kosen for running the single atom setup with me, sharing the workload, alleviating the boredom, and providing insights and solutions when I often have none. The joint experiments would also have been impossible without the four-wave mixing crew: Gurpreet Kaur Gulati, Bharath Srivathsan, Mathias Seidler, and Alessandro Cerè.

I am often easily distracted, and the rest of the group members have had to endure my inane rants and over-inquisitiveness (aka plain *kaypoh*-ness) about their work. To Poh Hou Shun, Tan Peng Kian, Lee Jianwei, Wilson Chin, Nguyen Chi Huan, Shi Yicheng, Janet Lim, Adrian Nugraha Utama, Shen Lijiong; as well as past group members Nick Lewty, Siddarth Koduru Joshi, Ng Tien Tjue, Kadir Durak, Victor Javier Huarcaya Azanon etc.: thanks for indulging me amid your own busy schedules, and entertaining me with discussions that usually turn out to be incredibly instructive for me.

A very special mention goes to Brenda Chng, who has spent five long years tolerating my being in the office space beside her. More than helping me out in various ways and contributing to the collective knowledge of Mankind through research, she does all the admin sh\*t nobody wants to do and keeps the entire lab running. In return, her requests for my assistance are usually met with incessant complaints and, at best, grudging compliance. Go for your PhD soon...

...and finally, an experimentalist must acknowledge the setups, the recipients of much tender loving care (when things work, i.e. not often) and cursing and swearing (when things don't, i.e. very often). Thanks for soldiering on throughout the experiments, and for bearing fruit to all the results contained within this little tome.

# Summary

In this work we present the interfacing of a single atom with single photons. We trap a single  $^{87}\text{Rb}$  atom at the focus of a free-space optical dipole trap, and achieve efficient atom-light coupling via strong focusing with a pair of aspheric lenses. Single photons are generated by heralding on one photon of a time-correlated photon pair, generated via four-wave mixing (FWM) in a cloud of cold  $^{87}\text{Rb}$  atoms.

The interfacing is demonstrated in two ways. First, we generate single photons from the single atom by exciting it with a short intense light pulse, and collecting the spontaneously emitted photons. We then interfere them with the heralded single photons generated by FWM at a 50:50 beam-splitter, and observe the Hong-Ou-Mandel (HOM) interference. We observe an interference visibility of  $62 \pm 4\%$  (without accidental corrections) and  $93 \pm 6\%$  (with accidental corrections); the high visibility demonstrates the compatibility between the single atom and FWM systems. We also study the effect of varying the temporal overlap between the photons on the observed two-photon interference, and obtain the well-known HOM dip.

Next, we send the heralded single photons generated by FWM directly to the single atom, and investigate the scattering dynamics for photons with exponentially rising and decaying temporal profiles. Although the two photon shapes have identical power spectra, they display different transient atomic excitations. We observe a peak excitation of  $2.77 \pm 0.12\%$  for the rising photon, which is a factor of  $1.56 \pm 0.11$  higher than the value of  $1.78 \pm 0.09\%$  for the decaying photon, consistent with a time-reversal argument. Although we observe a dependence of the overall extinction on the probe photon bandwidth, we measure similar extinction values for both photon shapes with the same decay time:  $4.21 \pm 0.18\%$  and  $4.40 \pm 0.20\%$  for decaying and rising photons, respectively.



# List of Publications & Conferences

The main results of this thesis have been reported in the following articles:

1. **VICTOR LEONG**, SANDOKO KOSEN, BHARATH SRIVATHSAN, GURPREET KAUR GULATI, ALESSANDRO CERÈ, AND CHRISTIAN KURTSIEFER. Hong-Ou-Mandel Interference Between Triggered and Heralded Single Photons from Separate Atomic Systems. *Phys. Rev. A* **91**, 063829 (2015).
2. **VICTOR LEONG**, MATHIAS ALEXANDER SEIDLER, MATTHIAS STEINER, ALESSANDRO CERÈ, AND CHRISTIAN KURTSIEFER. Time-resolved Scattering of a Single Photon by a Single Atom. arXiv:1604.08020 (2016).

The results have also been presented at the following international conferences:

1. **[Poster]** Hong-Ou-Mandel Interference between Photons from a Single Atom and an Atomic Ensemble. *24th International Conference on Atomic Physics (ICAP)*, Washington DC, USA (2014).
2. **[Talk]** Hong-Ou-Mandel Interference Between Triggered and Heralded Single Photons from Separate Atomic Systems. *46th Annual Meeting of the APS Division of Atomic, Molecular and Optical Physics (DAMOP)*, Columbus, OH, USA (2015).
3. **[Invited Talk and Proceedings]** Controlling the Interference of Single Photons Emitted by Independent Atomic Sources. *Proc. SPIE 9615, Quantum Communications and Quantum Imaging XIII*, 96150Q, San Diego, CA, USA (2015).
4. **[Talk]** Time-resolved Scattering of a Single Photon by a Single Atom. *Spring Meeting of the Deutsche Physikalische Gesellschaft (DPG)*, Hannover, Germany (2016).



# Table of contents

<b>Summary</b>	<b>vii</b>
<b>List of Publications &amp; Conferences</b>	<b>ix</b>
<b>List of figures</b>	<b>xv</b>
<b>1 Introduction</b>	<b>1</b>
<b>2 Basics of the Setups</b>	<b>5</b>
2.1 Single Atom Setup . . . . .	5
2.1.1 Overview . . . . .	5
2.1.2 Magneto-Optical Trap . . . . .	9
2.1.3 Far-Off-Resonant Optical Dipole Trap (FORT) . . . . .	11
2.1.4 Preparing the Trapped Atom . . . . .	16
2.2 Four-Wave Mixing . . . . .	18
2.2.1 Working Principle . . . . .	18
2.2.2 Setup . . . . .	20
2.2.3 Single Photon Properties . . . . .	22
2.3 Common instruments . . . . .	23
2.3.1 Coherent Light Sources . . . . .	24
2.3.2 Avalanche Photodetectors (APDs) . . . . .	26
2.3.3 Electronics . . . . .	27
<b>3 Hong-Ou-Mandel Interference Experiment</b>	<b>31</b>
3.1 Introduction . . . . .	31
3.1.1 Idea of the Experiment . . . . .	32
3.2 Theory . . . . .	33
3.2.1 A Little Intuition . . . . .	33

3.2.2	Coincident Photon Detection at the Beam-Splitter Outputs . . . . .	35
3.2.3	Exponentially Decaying Photons . . . . .	36
3.2.4	Quantum Beats . . . . .	37
3.3	Single Photons from the Single Atom . . . . .	38
3.3.1	Idea . . . . .	38
3.3.2	Generating the Short Excitation Pulse . . . . .	38
3.3.3	The Single Photon from the Single Atom . . . . .	41
3.3.4	Optimizing the Pulse Parameters . . . . .	43
3.4	HOM Experimental Setup . . . . .	46
3.4.1	Single Atom and FWM Setups . . . . .	46
3.4.2	HOM Interferometer . . . . .	48
3.4.3	Rates and Efficiencies . . . . .	51
3.5	Running the Experiment . . . . .	52
3.5.1	Choosing the Length of the Excitation Window . . . . .	52
3.5.2	Experimental Sequence . . . . .	55
3.5.3	Monitoring the Photon Decay Times . . . . .	56
3.6	Results . . . . .	56
3.6.1	Synchronized Photons: $\Delta T = 0$ . . . . .	57
3.6.2	HOM Dip . . . . .	60
3.6.3	Quantum Beats . . . . .	61
3.6.4	Different decay times . . . . .	62
3.7	Conclusion . . . . .	63
<b>4</b>	<b>Scattering Dynamics with Single Photons</b>	<b>65</b>
4.1	Introduction . . . . .	65
4.1.1	Idea of the Experiment . . . . .	67
4.2	Theory . . . . .	68
4.2.1	A Two-Level Atom and a Single-Photon Fock State . . . . .	68
4.2.2	Exponential Temporal Envelopes . . . . .	69
4.2.3	Forward and Back-Scattered Photons . . . . .	71
4.3	Preparing Exponentially Rising Probe Photons . . . . .	72
4.3.1	Working Principle . . . . .	72
4.3.2	Implementation . . . . .	75
4.4	Experimental Setup . . . . .	76
4.4.1	Optical Path of the Probe Photons . . . . .	76

4.4.2	Optical Switch for the Probe Photons . . . . .	78
4.5	Preliminary Characterizations . . . . .	79
4.5.1	Timing References . . . . .	80
4.5.2	Collection and Detection Efficiencies . . . . .	81
4.5.3	FWM Rates and Efficiencies . . . . .	83
4.5.4	Transmission of a Weak Coherent Field . . . . .	84
4.6	Running the Experiment . . . . .	87
4.6.1	Experimental Sequence . . . . .	87
4.6.2	Monitoring the Probe Photon Decay Times . . . . .	90
4.6.3	Monitoring the FWM Rates & Efficiencies . . . . .	91
4.7	Results . . . . .	91
4.7.1	Forward Direction: Scattering Dynamics, Overall Extinction . . . . .	91
4.7.2	Excitation Probability . . . . .	95
4.7.3	Extinction vs Decay Time . . . . .	98
4.8	Conclusion . . . . .	99
<b>5</b>	<b>Conclusion &amp; Outlook</b>	<b>101</b>
<b>Appendix A</b>	<b>Energy Levels of <math>^{87}\text{Rb}</math></b>	<b>105</b>
<b>Appendix B</b>	<b>Alignment Procedure</b>	<b>109</b>
B.1	Probe, Collection, Dipole Trap . . . . .	109
B.2	Magneto-Optical Trap (MOT) . . . . .	111
B.2.1	Preparing the MOT Beams . . . . .	111
B.2.2	Aligning the MOT . . . . .	113
B.3	Trapping the Single atom . . . . .	114
<b>Appendix C</b>	<b>Timestamp Correction</b>	<b>117</b>
<b>Appendix D</b>	<b>Calibrating APD Efficiencies</b>	<b>119</b>
<b>Appendix E</b>	<b>Ratio of Means vs Mean of Ratios</b>	<b>121</b>
<b>Appendix F</b>	<b>Setup Photographs</b>	<b>125</b>
<b>References</b>		<b>129</b>



# List of figures

1.1	Schematic of the atom-light interface. A single $^{87}\text{Rb}$ atom is trapped using an optical dipole trap at the focus of a confocal aspheric lens pair. The lenses focus incident light onto the atom, and also collect the atomic emission. . . .	2
2.1	Simplified schematic of the single atom setup. A single $^{87}\text{Rb}$ atom is trapped in free space using an optical dipole trap (wavelength 980 nm) at the focus of a confocal aspheric lens pair within an ultra-high vacuum chamber. The lenses also focus the probe light onto the atom, and collect the output light in the forward (transmission) and backward (reflection) directions. $\lambda/4$ : quarter-wave plate, AL: aspheric lens, BS: beamsplitter, DM: dichroic mirrors, F: interference filters. . . . .	6
2.2	<b>(Left)</b> Photo of the lens holder. On each side of the holder, an aspheric lens sits in the groove at the center, and is clamped in place by four titanium screws. <b>(Right)</b> IR camera image of the atomic fluorescence showing the strongly focused beam profile between the lens pair. The beam is tuned on resonance with an atomic transition in Rb. IR camera image is taken from [1].	7
2.3	Illustration of the core of the single atom setup, including the magnetic field coils and laser beams for the MOT, the cuvette (attached to a vacuum chamber) containing the aspheric lenses, and the FORT and probe beam paths. The inset is a zoom-in near the center of the lens system. For clarity, the lens holder is not shown. Figure credit: [1] . . . . .	9
2.4	Typical fluorescence signal measured by an APD in the forward or backward direction, with the MOT always turned on. The signal jumps between two discrete levels: a lower background level, and a higher level corresponding to having one atom in the trap. . . . .	13

- 2.5 Normalized second-order correlation function  $g^{(2)}(\tau)$  as a function of the time delay  $\tau$  between detection events in the forward and backward directions. We identify the time delay of the minimum  $g^{(2)}$  value as  $\tau = 0$ , and use it to offset the horizontal axis for experimental delays caused by optical and electrical lines. The data is not corrected for background counts. The anti-bunching dip at  $g^{(2)}(0) = 0.26 < 0.5$  (marked by dashed line) suggests the presence of only a single atom. The smooth line is a fit using a sinusoidal term with an exponentially decaying envelope. (Inset) At large  $\tau$ ,  $g^{(2)}(\tau) \rightarrow 1$ . 15
- 2.6 **(a)** Energy level scheme of the FWM process. We fix the detuning  $\Delta_1 = 30$  MHz, while  $\Delta_2 \sim 4$  MHz is a optimizable parameter. **(b)** Basic schematic of the FWM setup. Two pump beams (795 nm, 762 nm) are overlapped inside a cold cloud of  $^{87}\text{Rb}$  atoms in a MOT, generating signal (776 nm) and idler (780 nm) photon pairs. The detection of a signal photon heralds the presence of a single photon in the idler mode. DM: Dichroic mirrors, F: interference filters, P: polarizers. . . . . 19
- 2.7 The MOT apparatus of the FWM setup, showing the vacuum chamber, MOT beams, and quadrupole field coils. The two horizontal pairs of beams (in the x-z plane) are  $60^\circ$  apart; the vertical pair passes through the coils (along the y axis). Figure credit: [2] . . . . . 20
- 2.8 Histogram of coincidence events as a function of the time delay between the detection of signal and idler photons, with the signal photons serving as the herald. An exponential fit (solid line) indicates an idler photon decay time of  $\tau_f = 6.7$  ns. The error bars represent Poissonian statistics. . . . . 23
- 2.9 Partially uncovered ECDL box. . . . . 23
- 2.10 A typical laser setup. The HWP just after the ECDL minimizes losses through the anamorphic prism pair. A portion of the laser output is diverted to the FM spectroscopy setup, either with a beam sampler (as shown) or with a HWP and PBS. The retro-reflecting beams passing through the Rb cell are separated via a slight angular displacement (as shown) or with a QWP and PBS. We typically use a 150 mm lens pair to focus the beam onto the AOM, and apertures to transmit only the correct first order diffracted beam. More details can be found in the main text. AOM, EOM: acousto- and electro-optic modulators,  $\lambda/2$ ,  $\lambda/4$ : half- and quarter-wave plates (HWP and QWP, respectively), PBS: polarizing beam-splitter. . . . . 25
- 2.11 Exterior (**left**) and interior (**right**) of a home-made APD unit. Photo credit: [3] 27

3.1	(a) Schematic representation of the Hong-Ou-Mandel interference experiment. Single photons are obtained by heralding on one photon of a time-correlated photon pair generated via FWM. The heralding event triggers the generation of a single photon by a single atom. The single photons from each setup interfere at a 50:50 beam-splitter, and are detected by APDs at the outputs. (b) Simplified level scheme of the FWM process. The signal photon serves as the herald, and the idler photon is used for the interference experiment. (c) Level scheme for the single atom in the dipole trap and electronic transition used for exciting the single atom. . . . .	33
3.2	Four possible outcomes of two photons entering a 50:50 beam-splitter simultaneously. If both photons are indistinguishable, the probability amplitudes of outcomes 2 and 3 cancel out, and both photons will exit the beam-splitter from the same (but random) side; this is the HOM effect. Image: [4] . . . .	34
3.3	Schematic of the generation of the short excitation pulse. The open rectangles in the beam path are half-wave plates used to control the power splitting ratio at the PBS, and also optimize the alignment of the beam polarization to the polarization-maintaining input fibers of the EOMs. The depiction of the AOM double-pass setup has been simplified. More details are found in the main text. PBS: Polarizing beam-splitter, PD: photodiode, AOM: acousto-optic modulator, EOM: electro-optic modulator. . . . .	39
3.4	The 3 ns optical pulse, as measured by an APD with low jitter time (Micro Photon Devices PDM PD-050-CTC-FC). The data is recorded over many pulses, attenuated such that the number of detected photons per pulse $\ll 1$ . The timing resolution is 125 ps, limited by the timestamp unit. . . . .	40
3.5	Working principle of the short pulse generator. Two slightly delayed copies of the input pulse is generated, and the width of the output pulse is defined by the relative delay of the leading edge of the two copies. . . . .	40
3.6	Photograph of the temperature-stabilized enclosure for the EOM, with the outer cover flipped open. The EOM sits within a trench in the inner aluminium block. The temperature is monitored by a thermistor, and stabilized using Peltier elements via an external PID loop. . . . .	41
3.7	Experimental sequence for the pulsed excitation of the single atom. When the trigger gate is opened during the excitation window (of width $\Delta t_{\text{exc}}$ ), an incoming trigger signal generates an excitation pulse. . . . .	42

- 3.8 Spontaneous emission from the single atom, measured in the backward direction, for  $\langle N \rangle = 700$  photons. The recorded APD counts are normalised to the total number of excitation pulses sent to the atom. Without the atom in the trap, we observe that a portion of the excitation pulse is back-reflected into the collection mode by various components in the optical path, but this should not affect the experiment significantly. The time-bin size is 1 ns, and the error bars reflect Poissonian statistics. The detection times are offset to account for delays introduced by optical and electrical delay lines. . . . . 43
- 3.9 Coincidence measurement between two APDs at the outputs of a 50:50 beam-splitter, with the single photons generated by the single atom via triggered excitation as the input. We observe regular peaks  $8 \mu\text{s}$  apart, corresponding to the interval between excitation pulses sent to the atom. The lack of coincidence events at zero time delay is the signature of single photons; the residual of coincidence events there ( $\sim 10\%$  of the average of the other peaks) is consistent with the expected number of accidental coincidences contributed by background noise in the measurement. . . . . 44
- 3.10 Rabi oscillations in the excitation probability  $P_e$  as we vary the average pulse photon number  $\langle N \rangle$ . The solid line shows a fit to the form  $P_e = A \sin^2(B\sqrt{\langle N \rangle})$ , where  $A$  and  $B$  are free parameters. Vertical error bars are represent Poissonian statistics, while horizontal bars represent the drifts in  $\langle N \rangle$  during the measurement. . . . . 45
- 3.11 Schematic of the full HOM experimental setup, consisting of the FWM setup (top left), single atom setup (bottom left), and the HOM interferometer (right). One output port of the HOM 50:50 beam-splitter is connected to another 50:50 fiber beam-splitter, with detectors  $D_{b1}$  and at  $D_{b2}$  the outputs; these two detectors are collectively referred to as  $D_b$ . AOM, EOM: acousto- and electro-optic modulators, DM: dichroic mirrors, P: polarizers, F: interference filters, NDF: neutral density filter,  $\lambda/2$ ,  $\lambda/4$ : half- and quarter-wave plates, (P)BS: (polarizing) beam splitters,  $D_a$ ,  $D_{b1}$ ,  $D_{b2}$ ,  $D_f$ ,  $D_t$ : avalanche photodetectors. 46

- 3.12 APD measurements at the backward collection arm for the pulsed excitation of the single atom. **(a)**: As a reference, we include the red curve, taken from Fig. 3.8, which is measured with the atom and with a OD 3.7 filter in the forward collection arm. The blue curve is measured without the filter. There is a 5 m fiber between the collection lens and APD  $D_f$ . **(b)**: Both curves are measured with a OD 0.16 filter in the forward collection arm, and a longer 9 m fiber. Compared to (a), the noise floor is suppressed, and the strong back-reflection peaks are delayed to  $t > 87$  ns. The small initial peak (blue curve in (a)) is also eliminated by slightly tilting the optical components that reflected a significant amount of light. In both figures, the time-bin width is 1 ns, and the APD counts are normalised to the peak of the curve taken with the trapped atom. The detection times are offset to account for delays introduced by optical and electrical delay lines. . . . . 48
- 3.13 Verifying the spatial mode-matching of the HOM interferometer. **(a)** The interferometer inputs are replaced with a frequency-locked laser split by a fiber beam-splitter, with one arm going through a short free-space coupling link. **(b)** Photodetector signal at one of the HOM interferometer outputs showing interference fringes under the passive instability of the free-space link. . . . . 50
- 3.14 Temporal profile of the single photons generated by the single atom (open circles) and FWM (filled circles) sources. The coherence times are obtained from exponential fits (solid lines). The APD counts are sorted into 500 ps wide time-bins, and normalized such that the area under both curves are equal. 51
- 3.15 Heralding efficiency of the FWM source  $\eta_{\text{fwm}}$  at different idler decay times  $\tau_f$  during the HOM experiment. Error bars reflect the standard deviation in the distribution of the measured values. . . . . 52
- 3.16 The measured survival and excitation probabilities as a function of the excitation window  $\Delta t_{\text{exc}}$ . . . . . 53
- 3.17 Experimental sequence of the HOM interference experiment for the single atom setup (top) and the FWM setup (bottom). The two sequences run asynchronously. When the trigger gate is opened during the 100 ms measurement window, an incoming trigger signal generates an excitation pulse. . . . . 54

- 3.18 Coincidence probability between  $D_a$  and  $D_b$  measured at  $\Delta T = 0$ . The filled and open circles represent the cases where the photons have orthogonal (non-interfering) and parallel (interfering) polarizations, respectively. The data is sorted into 10 ns wide time-bins and normalized to the total number of trigger events  $N_t$ . The solid lines represent  $G_{\text{acc}} + A \cdot G(\Delta t_{ab})$  [see Eq. (3.20), (3.21)], where  $G_{\text{acc}}$  is a constant offset describing the accidental coincidences, and  $A$  is a scaling factor. Error bars represent Poissonian statistics. . . . . 58
- 3.19 Coincidence probability for interfering photons  $G_{||}$  between  $D_a$  and  $D_b$ , measured for several values of  $\Delta T$ . The data is sorted into 10 ns wide time-bins and normalized to the total number of trigger events  $N_t$ . As  $|\Delta T|$  increases, the coincidence events are concentrated around two separate peaks at  $\Delta t_{ab} = \pm|\Delta T|$ . The solid lines represent  $G_{\text{acc}} + A \cdot G_{||}(\Delta t_{ab})$ , where  $G_{||}(\Delta t_{ab})$  is given by the solution of Eq. (3.10),  $G_{\text{acc}}$  is a constant offset describing the accidental coincidences, and  $A$  is a scaling factor. Error bars represent Poissonian statistics. . . . . 59
- 3.20 Normalized coincidence probability  $P_{||}/P_{\perp} = 1 - V$ , corrected for accidental coincidences, showing the HOM dip. The solid line shows expected values obtained from Eq. (3.18). Vertical error bars represent Poissonian statistics, while horizontal bars reflect the uncertainty in the calibration of  $\Delta T$  due the APD timing jitter. . . . . 60
- 3.21 Quantum beats in the coincidence probability  $G_{||}$  between  $D_a$  and  $D_b$ . The data is sorted into 2 ns wide time-bins and normalized to the total number of trigger events  $N_t$ . The finer time resolution allows us to resolve the temporal structure of the beat. The solid line is a fit to the form described by Eq. (3.24), with the free parameters being a scaling factor, an accidentals offset, and the detuning  $\delta$ . The obtained beat frequency of  $\delta/2\pi = 75.7 \pm 0.7$  MHz is consistent with the frequency difference between the two photons. Error bars represent Poissonian statistics. . . . . 61
- 3.22 Measured ratios  $P_{1,1}/P_{2,0}$  at different idler photon decay times  $\tau_f$ . The solid line represents the expected values of  $1 - V/1 + V$ , where  $V$  is the HOM interference visibility. Vertical error bars represent Poissonian statistics, while horizontal bars represent the standard deviation in the distribution of measured  $\tau_f$  values. . . . . 63

- 4.1 **(a)** Illustration of the time-reversal symmetry between spontaneous decay and perfect single-photon excitation. The spontaneous decay process emits an exponentially decaying photon in a spatial mode corresponding to the atomic dipole transition. Perfect single-photon excitation requires an exponentially rising photon propagating towards the atom with the same spatial mode. **(b)** Calculated excitation probability  $P_e(t)$  for both exponentially rising (red solid curve) and decaying (blue dashed curve) photon shapes, assuming perfectly matched bandwidths and spatial modes (see §4.2.2). The rising photon leads to perfect excitation, with a maximum  $P_e(t)$  value of 1; for the decaying photon, the maximum value is 0.56. . . . . 66
- 4.2 Concept of the scattering experiment. An incident single photon excites a two-level atom in free space. The time evolution of the atomic excited state population  $P_e(t)$  can be inferred by measuring the photons at the forward and backward detectors  $D_f$  and  $D_b$ . . . . . 67
- 4.3 **(a)**: Inverting an exponentially rising photon. If such a photon is sent to an asymmetric resonant bandwidth-matched cavity, the waveforms of the direct reflection and the leakage of the cavity mode through mirror  $M_1$  destructively interfere and completely cancel out, thus no light is reflected and the photon is completely loaded into the cavity. The photon subsequently exits the cavity with an exponentially decaying temporal profile. **(b)**: If the signal photon from FWM is sent to such a cavity prior to its detection, the shape of the heralded idler (probe) photon is transformed from an exponential decay to an exponential rise. R: reflectivity of cavity mirror. . . . . 73
- 4.4 Cavity setup for controlling the temporal shape of the probe photon. The heralding photons are sent to an asymmetric bandwidth-matched cavity, and the reflected light is then collected into another single-mode fiber. An auxiliary 780 nm laser is used to stabilize the cavity length using the Pound-Drever-Hall (PDH) technique. The acousto-optic modulator (AOM) in the auxiliary beam path brings the cavity into or out of resonance with the input light. PBS: polarizing beam-splitter,  $\lambda/4$ : quarter-wave plate, L: lens, DM: dichroic mirror, F: interference filter. . . . . 75

4.5	Schematic of the full setup for the scattering experiment, consisting of the FWM setup (top left), the cavity setup for controlling the temporal profile of the probe photon (top right), and the single atom setup (bottom). AOM: acousto-optic modulators, DM: dichroic mirrors, P: polarizers, F: interference filters, $\lambda/4$ : quarter-wave plates, (P)BS: (polarizing) beam splitters, $D_b$ , $D_f$ , $D_h$ : avalanche photodetectors. . . . .	77
4.6	Coincidence probability between $D_h$ and $D_f$ , plotted on a semi-log scale to highlight the 600 ns AOM window and the two different offset levels: a lower level mainly caused by dark counts at $D_f$ , and a higher level corresponding to the accidentals offset in our experimental data. The latter is primarily due to light from the FWM setup which is uncorrelated to the heralding photons. The time-bin size is 2 ns, and the probe photon decay time is $\tau_p \approx 13.5$ ns. The detection times here have not been offset to account for electrical and optical delays. . . . .	79
4.7	Coincidence histograms between the heralding detector $D_h$ and the forward detector $D_f$ for exponentially decaying (red curve) and rising (blue curve) probe photons of decay time $\tau_p = 13.3$ ns. We choose between the decaying and rising temporal shapes by setting the cavity detuning to 70 MHz or zero (on resonance) with respect to the heralding photon central frequency, respectively. The time-bin width is 1 ns. Due to imperfections of the cavity setup (spatial alignment, bandwidth matching, etc.), there is a residual tail in the measured profile at $t_i < 0$ ( $t_i > 0$ ) for the decaying (rising) shape. A common offset of 879 ns is applied to account for delays introduced by optical and electrical delay lines, and the reference point $t_i = 0$ is marked in the zoomed-in region (see inset). . . . .	80
4.8	The measured scattering rate $R_{sc}$ at the backward APD $D_b$ as a function of the probe power $P_{probe}$ , showing the saturation behaviour of the single atom as the probe power is increased. Error bars represent Poissonian statistics. The large scatter of the data points at higher $P_{probe}$ values is likely due to parameter drifts which were not characterized. . . . .	82
4.9	Heralding rates and efficiencies of the FWM source at different probe photon decay times $\tau_p$ during the scattering experiment. Error bars reflect the standard deviation in the distribution of the measured values. . . . .	83
4.10	Experimental sequence for measuring the transmission of a weak coherent field. . . . .	85

- 4.11 Transmission of a weak coherent field as a function of the detuning of the probe from the bare atomic transition, showing a maximum extinction of 8.5% on resonance at  $\delta/2\pi = 72$  MHz. Error bars represent Poissonian statistics. . . . . 86
- 4.12 Experimental sequence of the scattering experiment for the single atom setup (top) and the FWM setup (bottom). The two sequences run asynchronously. When the trigger gate is opened during the 100 ms measurement window, a heralding event at  $D_h$  triggers the activation of the probe photon AOM for 600 ns. . . . . 88
- 4.13 Signal handling scheme for the scattering experiment. Each heralding detection event at  $D_h$  generates a trigger signal. After the atom is optically pumped and the sequence is at the measurement window, the single atom setup sends a “ready” signal to the AND gate; the admitted trigger signals are then recorded, and used to trigger the AOM and the gate unit. The gate unit transmits clicks from  $D_b$  and  $D_f$  to the timestamp unit within a  $2 \mu\text{s}$  window from the trigger. The inset shows these events on a timeline starting from a trigger signal arriving at the AND gate. . . . . 90
- 4.14 Coincidence histograms between the heralding detector  $D_h$  and the forward detector  $D_f$  for exponentially decaying (**left**) and rising (**right**) probe photons. Black circles ( $G_{f,0}$ ): reference measurements performed without the trapped atom. Red diamonds ( $G_f$ ): data recorded with the atom present. The decay time is  $\tau_p = 13.3 \pm 0.1$  ns obtained from a fit of  $G_{f,0}$  for the decaying photon. The time-bin width is  $\Delta t = 2$  ns. Error bars representing Poissonian statistics are smaller than the symbol size. Detection times are offset by 879 ns to account for delays introduced by electrical and optical lines. . . . . 92
- 4.15 Differences in the detection probabilities per unit time  $\delta(t_i) = R_{f,0}(t_i) - R_f(t_i)$ , measured in the forward direction for exponentially decaying (**left**) and rising (**right**) probe photons.  $R_{f,0}(t_i)$  and  $R_f(t_i)$  are individually corrected for accidentals. The time-bin width is 2 ns. Error bars represent Poissonian statistics. Detection times are offset by 879 ns to account for delays introduced by electrical and optical lines. Solid lines are analytical solutions described by Eq. (4.18) for  $\tau_p = 13.3$  ns and  $\Lambda = 0.033$ . . . . . 93

- 4.16 Ratio of the detection probabilities per unit time  $R_f(t_i)/R_{f,0}(t_i)$ , measured in the forward direction for exponentially decaying (**left**) and rising (**right**) probe photons.  $R_{f,0}(t_i)$  and  $R_f(t_i)$  are individually corrected for accidentals. The time-bin width is 2 ns. Error bars represent Poissonian statistics. Detection times are offset by 879 ns to account for delays introduced by electrical and optical lines. Solid lines are analytical solutions based on Eq. (4.17) for  $\tau_p = 13.3$  ns and  $\Lambda = 0.033$ . . . . . 95
- 4.17 Atomic excited state population  $P_e(t_i)$  for exponentially decaying (**left**) and rising (**right**) probe photons. Results are obtained from the measurements in the forward (red open circles, time-bin width 2 ns) and backward (green filled diamonds, time-bin width 5 ns) directions, and are corrected for accidental coincidences. Error bars represent Poissonian statistics. Detection times in the forward (backward) directions are offset by 879 ns (891 ns) to account for delays introduced by electrical and optical lines. Solid lines are calculated from Eq. (4.9) and (4.11) for  $\tau_p = 13.3$  ns and  $\Lambda = 0.033$ . . . . . 96
- 4.18 Overall extinction values for exponentially decaying probe photons of different decay times  $\tau_p$ . Vertical error bars represent Poissonian statistics, while horizontal error bars reflect the standard deviation in the distribution of the measured  $\tau_p$  values. Black dashed line represents a fit to Eq. (4.15), which yields  $\Lambda = 0.0303$ . Blue solid line represents Eq. (4.15) calculated with  $\Lambda = 0.033$ , which best describes the observations for  $\tau_p = 13.3$  ns presented in previous sections. . . . . 99
- A.1 Transitions of  $^{87}\text{Rb}$  used in the single atom and four-wave mixing (FWM) systems. . . . . 106
- A.2 Energy levels of the  $^{87}\text{Rb}$  atom for the D1 and D2 lines, showing the hyperfine and Zeeman manifolds. The number above each  $m_F$  level is the calculated AC Stark shift, in MHz, per mK of dipole trap depth; the AC Stark shift scales linearly with the trap depth. For each hyperfine level, we also state the approximate Landé g-factor and the Zeeman shift per Gauss per  $m_F$ . Other values are taken from [5]. . . . . 107
- B.1 Simplified sketch of the MOT beams. (**Left**) Front view of the cuvette, showing the vertical MOT beams. (**Right**) Top view, showing the horizontal MOT beams. PBS: polarizing beam-splitter, QWP: quarter-wave plate. . . . . 111

B.2	Sketch of the beam paths marked by atomic fluorescence, as seen on the IR camera images. Orange, red, and blue lines represent the probe beam, vertical MOT beams and horizontal MOT beam, respectively. For the side view, the camera is aligned to a weak probe beam sent through the aspheric lens (AL). When the MOT beam passes through the focus of the AL, the fluorescence fills the lens homogeneously. . . . .	113
B.3	IR camera image of the side view of the cuvette, showing a small cloud of cold atoms (labelled MOT) through the aspheric lens (AL). The alignment has yet to be optimized for obtaining a bright and stable atom cloud. . . . .	114
C.1	Autocorrelation histogram of recorded timestamp signals from an APD, with a random light source (a fluorescent lamp) as the input. The results with and without correcting for unequal timestamp bins are shown. The inset displays a portion of the same data at a finer time resolution. For a random input, the measured counts should be uniform across all detection time delays; the uncorrected version shows periodic peaks every 2 ns, a consequence of the bins being unequal. The corrected version shows a more uniform distribution and a smaller spread in counts. The rising slope during the first 200 ns is due to the timestamp dead time. The time bin width is 125 ps, which is the nominal resolution of the timestamp unit. . . . .	118
C.2	Distribution of recorded counts from Fig. C.1 across the 16 timestamp “bins”, with and without correction. The correction provides a uniform distribution, as expected for a random input. . . . .	118
D.1	Schematic of the APD calibration setup. The 810 nm input laser is split at a 50:50 beam-splitter (BS); one output arm goes to a fixed photodiode, while the other is attenuated by a stack of 6 neutral density filters (NDF) before being sent to the APD being tested. To avoid etalon effects, the NDFs are slightly tilted with respect to the beam. . . . .	119
F.1	The single atom setup. . . . .	125
F.2	Vaccum chamber, cuvette (within the magnetic field coil structure), and surrounding optics of the single atom setup. . . . .	126
F.3	Close-up of the cuvette at the single atom setup. Photo credit: Alessandro Cerè.	126
F.4	Close-up of the cuvette at the FWM setup, showing the quadrupole field coils.	127
F.5	The master record of all our experimental parameters. . . . .	127

F.6 Entanglement of wires is much easier than the entanglement of qubits... . . . 128

F.7 Precision alignment required... . . . . . 128

# Chapter 1

## Introduction

Research in quantum information science has seen tremendous growth in the past decades, and buzzwords containing the ‘quantum’ prefix have become increasingly familiar in popular discussions of computing, networks, encryption, and so on.

The intrigue surrounding these fields revolve around their central workhorse: the quantum bit, or *qubit*, which is a unit of quantum information. Unlike its classical counterpart, the state of a qubit can either be 1 or 0 *or any coherent superposition of the two*. Moreover, multiple quantum particles can share a property known as *entanglement*, a quantum correlation with no classical counterpart; simply put, if two particles are entangled, their state can only be expressed as an inseparable whole, and each particle cannot be fully described individually.

These unique quantum properties open the door to many exciting prospects, including quantum computation using Shor’s algorithm that can potentially break the widely-used RSA cryptographic scheme [6], quantum cryptography with *unbreakable* cryptographic codes [7], metrology with precisions beyond the so-called quantum limit [8], and simulations of quantum many-body systems that are challenging to perform classically [9].

To be practically useful, quantum systems need to scaled up [10]. One approach simply focuses on increasing the number of qubits. D-Wave, arguably the most famous name in commercial quantum computing, already produces machines operating up to 1000 qubits [11], even though its performance advantage over conventional computers, or if it indeed is a quantum computer at all, is still being debated [12, 13].

Another proposal envisions a ‘quantum internet’, consisting of a distributed network of quantum systems that serve as stationary nodes, and photons that serve as ‘flying’ qubits that carry quantum information between the nodes [14]. As such, efficient interaction with light at the single-photon level is crucial for the feasibility of this scheme, and much research effort has been devoted to developing suitable building blocks for such a network. So far,

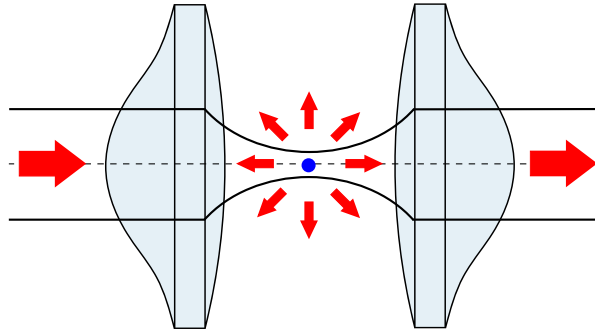


**Figure 1.1:** Schematic of the atom-light interface. A single  $^{87}\text{Rb}$  atom is trapped using an optical dipole trap at the focus of a confocal aspheric lens pair. The lenses focus incident light onto the atom, and also collect the atomic emission.

promising progress has been demonstrated for various systems, including superconducting circuits [15], quantum dots [16, 17], colour centers in diamond [18], trapped ions [19, 20], neutral atoms [21–23], etc.

### A Single $^{87}\text{Rb}$ Atom in Free Space

Among the numerous candidates listed above, the work presented in this thesis focuses on a single neutral  $^{87}\text{Rb}$  atom in a free-space optical dipole trap. Single neutral atoms are relatively simple and well-understood, and the excellent isolation from environmental noise provides long lifetimes of the typically fragile quantum states [24]. As the interaction of light with a single atom is inherently weak, many single-atom systems utilize cavity quantum electrodynamic (QED) effects, by placing the atom within an optical resonator to enhance the strength of the light field [25, 26].

Instead of a cavity, we choose to achieve an efficient atom-light coupling<sup>1</sup> via strong focusing in free space using aspheric lenses (see Fig. 1.1). The focusing strength of the lenses determine how well we can focus incident light onto the atom and collect the atomic emission. Although the atom-light interaction is weaker compared to typical cavity QED systems, the main motivation for pursuing this approach is twofold.

First, a cavity would impose a different set of boundary conditions on the atom-cavity system and change the way the atom interacts with incoming light fields, including giving rise to phenomena such as vacuum Rabi splitting [26] and one-atom lasing [27]. Therefore, such a system would be unsuitable for exploring the physics of the ‘bare’ atom-light interaction, which is still of fundamental interest in the fields atomic physics and quantum optics.

<sup>1</sup> Because ‘strong coupling’ has a specific meaning in several related fields, especially cavity QED, we avoid using this term.

Second, scaling up cavity-based systems can be challenging due to the demands in connecting multiple high-finesse cavities while managing losses [28, 29], and typically require active stabilization (e.g. of the cavity length) to maintain the atom-light coupling. In contrast, free-space lens systems are simpler to construct and operate, thus providing a promising avenue towards scalable quantum networks.

### **Towards Single-Photon Interactions**

This thesis builds upon the past achievements within our research group, where we have performed a series of experiments based on the single  $^{87}\text{Rb}$  atom in free space.

Despite early predictions that such free-space strong focusing techniques are not sufficiently efficient [30]<sup>2</sup>, we observe an extinction of 9.8% and a phase shift of  $1^\circ$  for a weak coherent beam ( $\sim 10^4$  photons  $\text{s}^{-1}$ ), demonstrating that substantial atom-light interaction can be achieved even without the enhancement of a cavity [28, 31].

Next, using weak coherent pulses, we explored temporal pulse shaping techniques to increase the excitation probability of the atom. Approaching the single-photon limit with an average of  $\langle N \rangle \approx 2$  photons per pulse, we show that exponentially rising pulses excite the atom more efficiently than rectangular pulses, with a maximum excitation probability of  $\approx 5\%$  [32].

We are now ready to pursue experiments at the single-photon level, and this serves as the starting point for this thesis. To demonstrate the compatibility of the single-atom system with quantum information protocols, we have to use ‘proper’ single photons, i.e. single-photon Fock states instead of attenuated coherent pulses with  $\langle N \rangle = 1$ . For efficient interaction, it is essential to match the polarization, frequency and temporal profile of the single photon to the relevant atomic transition; this places stringent demands on our ability to generate single photons with compatible properties. Here, we utilize a tunable source of narrowband photon pairs generated via four-wave mixing (FWM) to obtain heralded single photons. The FWM source has been developed within our group over the past several years, and its capabilities are reported in Refs. [33–36].

---

<sup>2</sup> Ref. [30] models the focusing of a circularly polarized Gaussian beam by an ideal lens, and assumes that the lens produces a parabolic (instead of spherical) wavefront, and does not change the light polarization. Both assumptions break down in the strong focusing regime.

## Interfacing with Single Photons

There are two general ways with which the single atom can interface with single photons: *directly*, by sending the photons to the atom, or *indirectly*, by separately generating another single photon from the atom, and interfering the two photons.

For the indirect interaction, we generate a single photon from the atom by exciting it with a short intense light pulse, and collecting the spontaneously emitted photon. We then send both photons to a 50:50 beam-splitter, and observe the Hong-Ou-Mandel (HOM) interference effect. Direct interaction is achieved by sending the single photons to the single atom and performing a scattering experiment; here we investigate the scattering dynamics for exponentially rising and decaying photon temporal envelopes.

Because the atomic excitation with a single photon is much weaker than for an intense light pulse, observing the direct scattering is experimentally more challenging. As such, we carry out the HOM experiment first to evaluate the interaction between the single atom and FWM systems; it serves as a platform for us to understand the connection between the two separate setups, as well as the suitability of the FWM photons for direct interaction with the single atom.

## Thesis Outline

This thesis is organised as follows: Chapter 2 describes the basic operation of the single atom and FWM setups. Chapter 3 presents HOM interference experiment, and Chapter 4 reports on the scattering dynamics of single photons by the single atom. Finally, in Chapter 5 we conclude the thesis, and discuss the outlook of the experiment.

# Chapter 2

## Basics of the Setups

This chapter presents the sources of the two key ingredients of our experiments: the single atom setup that traps a single  $^{87}\text{Rb}$  atom in free-space and performs the efficient atom-light coupling, and the four-wave mixing (FWM) setup that produces the heralded single photons that interact with the single atom. The two setups are physically located in adjacent rooms, approximately 15 m apart.

The exact way in which the two setups are combined to carry out the experiments will be covered in the later chapters. Here, we will introduce each setup and describe how they perform their core functions, then discuss some of the experimental apparatus that are common to both setups.

### 2.1 Single Atom Setup

#### 2.1.1 Overview

The schematic of the single atom setup is shown in Fig. 2.1. A single  $^{87}\text{Rb}$  atom is trapped using a free-space far-off-resonant optical dipole trap (FORT, wavelength 980 nm) at the focus of a confocal aspheric lens pair within an ultra-high vacuum (UHV) chamber. We achieve efficient atom-light coupling via strong focusing with the lens pair: they focus the probe light onto the atom, and also collect the atomic emission in the forward (transmission) and backward (reflection) directions.

To load the dipole trap, we first have to cool the atoms to below the dipole trap depth, which is  $\sim 2$  mK in our setup. We use a magneto-optical trap (MOT) [37] to produce a cloud of  $^{87}\text{Rb}$  atoms which is sufficiently cold and dense to load single atoms into the dipole trap.

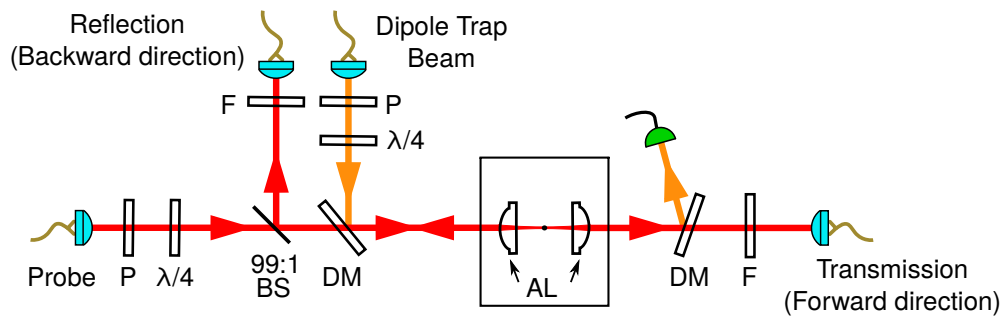


**Figure 2.1:** Simplified schematic of the single atom setup. A single  $^{87}\text{Rb}$  atom is trapped in free space using an optical dipole trap (wavelength 980 nm) at the focus of a confocal aspheric lens pair within an ultra-high vacuum chamber. The lenses also focus the probe light onto the atom, and collect the output light in the forward (transmission) and backward (reflection) directions.  $\lambda/4$ : quarter-wave plate, AL: aspheric lens, BS: beamsplitter, DM: dichroic mirrors, F: interference filters.

After preparing the trapped single atom in the ground state of an effective two-level system, it is ready to take part in the actual experiment.

The following sections elaborate on the technical details of the setup.

### Confocal Aspheric Lens Pair

We focus our probe light to a diffraction-limited spot with minimal spherical aberrations using aspheric lenses. Compared to multi-element microscope objectives, aspheric lenses are much cheaper, and their compact size allows us to place them within a small cuvette, thus greatly simplifying the vacuum setup<sup>1</sup>.

We use moulded glass aspheric lenses (LightPath Technologies 350230-B) with a numerical aperture of 0.55 and an effective focal length of 4.51 mm at the design wavelength of 780 nm. They have a clear aperture of 4.95 mm, a working distance of 2.91 mm, and are anti-reflection coated for 600–1050 nm.

For a confocal arrangement, the lens pair is mounted on a monolithic aluminium holder, with the back planes separated by  $5.82 \pm 0.02$  mm (twice the working distance; the uncertainty is due to machining accuracy), and held in place by titanium screws. Fig. 2.2 shows the lens holder, as well as the strongly focused beam profile between the lens pair. We note the importance of not having any ferromagnetic materials in close proximity to the trapped atom, as they might distort the magnetic field environment that the atom experiences.

<sup>1</sup> An alternative approach places the microscope objective on the outside of the vacuum chamber, e.g. in Ref. [38]. However, in such setups, the focused light has to pass through a thick planar window, which results in aberrations.

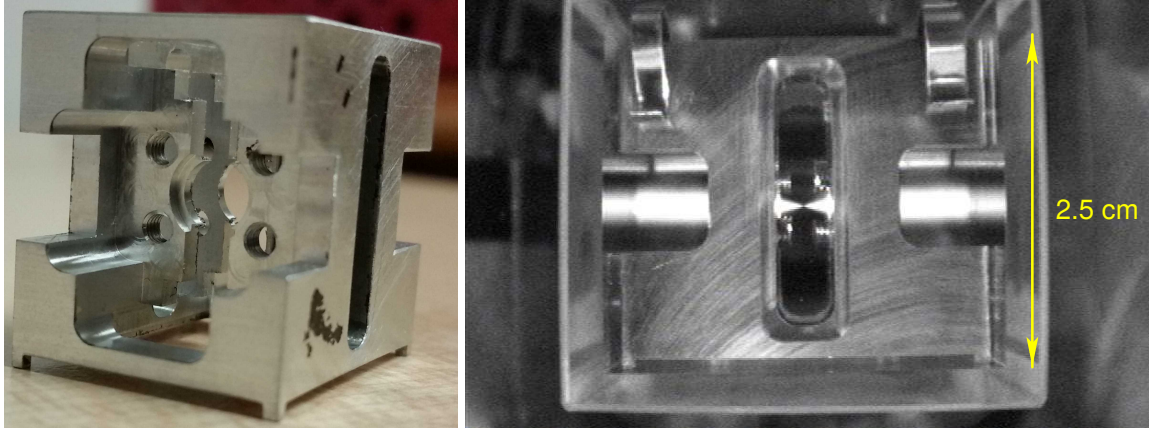


**Figure 2.2:** (Left) Photo of the lens holder. On each side of the holder, an aspheric lens sits in the groove at the center, and is clamped in place by four titanium screws. (Right) IR camera image of the atomic fluorescence showing the strongly focused beam profile between the lens pair. The beam is tuned on resonance with an atomic transition in Rb. IR camera image is taken from [1].

With this lens setup, the overlap between the spatial mode of the probe beam and the atomic dipole emission pattern was previously measured to be  $\Lambda \sim 0.03$  [32], where  $\Lambda \in [0, 1]$  and  $\Lambda = 1$  corresponds to a complete spatial mode overlap.

### Probe and Dipole Trap beams

Both the probe and dipole trap beams are focused by the aspheric lens pair. We combine both beams using a dichroic mirror (DM; all DMs in the single atom setup are designed for high transmission at 780 nm and high reflectivity at 980 nm). After passing through the vacuum chamber, the dipole trap beam is separated from the probe beam by a stack of 2 DMs, and sent to a photodiode which monitors the trap beam power.

For optimal spatial coupling between the trapped atom and the probe light, the foci of both beams must coincide. However, due to chromatic aberrations, the effective focal length of the aspheric lenses is different for the 780 nm probe and 980 nm trap light. As such, we ensure the overlapping of both beam foci by adjusting the beam divergences (see Appendix B for alignment details). From the measured divergences, the resultant focal waists are estimated using paraxial approximation to be  $\simeq 0.9 \mu\text{m}$  and  $\simeq 1.8 \mu\text{m}$  for the probe and dipole trap beams, respectively.

Both beams are circularly polarized. In principle, a polarizer and a quarter-wave plate (QWP) is sufficient to generate a circularly polarized beam. However, as the DM severely distorts the beam polarization (when it is neither S- nor P-polarized), we use multiple

waveplates (instead of a single QWP as depicted in Fig. 2.1) to compensate: a half-wave plate (HWP) and a QWP for the dipole trap beam, and a QWP-HWP-QWP combination for the probe beam. The purity of the circular polarization is limited by the quality of the waveplates; when measuring the transmitted intensity of the beam  $I$  through a rotating linear polarizer, we measure a visibility of  $(I_{\max} - I_{\min}) / (I_{\max} + I_{\min}) \approx 3$  to 5% (ideally, the visibility should be zero).

### Collection Optics

Collection modes on both sides of the vacuum chamber are overlapped with the probe beam mode and collect light emitted from the atom at 780 nm into single-mode fibers. Additionally, we collect about 50% of the transmitted probe light in the forward direction. All other wavelengths are rejected by a set of filters (depicted as F in Fig. 2.1): 1 x narrowband interference filter (Semrock MaxLine LL01-780-12.5, FWHM 3 nm) and 2 x DM. As our experiments involve detecting signals at the single-photon level, the use of multiple DMs in the setup is necessary to suppress the dipole trap light in the collection fibers.

### Vacuum Chamber

To create a MOT and to trap a single atom, we require an ultra-high vacuum (UHV) environment. The centerpiece of the vacuum system is a glass cuvette (Hellma OG glass, 3x3x7 cm, wall thickness 2.5 mm), bonded to the rest of the chamber with an Indium wire and sealed with a low vapour-pressure epoxy (Torr Seal, Varian [now Agilent]). The cuvette houses the aspheric lens pair and provides optical access from all sides. Its outer surfaces are anti-reflection coated for 500 – 1100 nm, with a transmission of 91% transmission through both walls at 780 nm.

The base pressure is maintained at  $\approx 10^{-10}$  mbar with a 20 l/s ion pump (Varian VacIon Plus 20 Starcell)<sup>2</sup>. Also attached to the chamber are a hot-cathode ionization gauge (Varian UHV-24) and a titanium sublimation pump; they are used to monitor and reduce the chamber pressure, respectively, and are typically only used during the initial chamber pump-down/bake-out and during troubleshooting.

Rubidium vapour is introduced into the chamber via evaporation from a Rb dispenser (SAES Getters RB/NF/4.8/17 FT10+10) by running a current (typically 1.8-2.3 A) through

<sup>2</sup> The base pressure deteriorates slightly with time; when the vacuum chamber was last sealed in 2010, the base pressure was  $\simeq 10^{-11}$  mbar after bake-out.

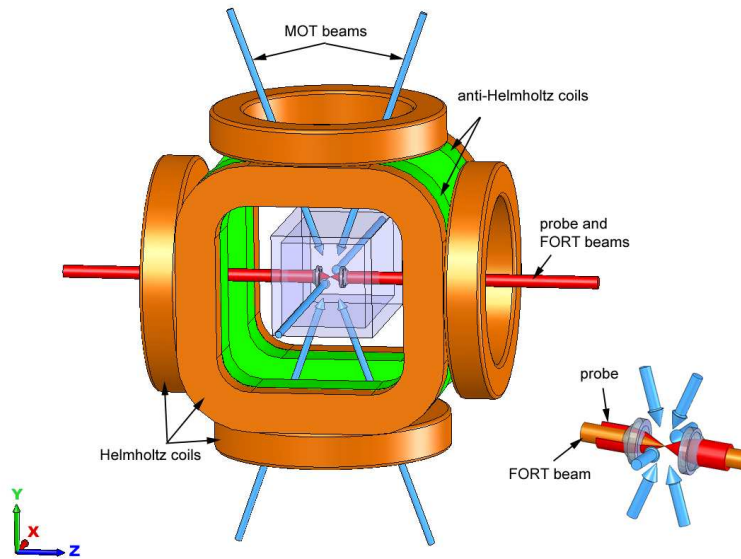


**Figure 2.3:** Illustration of the core of the single atom setup, including the magnetic field coils and laser beams for the MOT, the cuvette (attached to a vacuum chamber) containing the aspheric lenses, and the FORT and probe beam paths. The inset is a zoom-in near the center of the lens system. For clarity, the lens holder is not shown. Figure credit: [1]

it. During the operation of the dispenser, the chamber pressure typically does not exceed  $10^{-8}$  mbar.

### Gaussian beams

All light beams are sent to the trapped atom via single-mode optical fibers. This serves as a convenient way to guide the light from various parts of the setup to the atom, and also “cleans up” the spatial mode of the beams, which are then defined by the fundamental Gaussian mode supported by the fiber.

### 2.1.2 Magneto-Optical Trap

The core of the setup is shown in Fig. 2.3. The MOT is formed at the intersection of 3 pairs of counter-propagating beams and a magnetic quadrupole field with a field minimum at the intersection point. A full description of how a MOT cools and traps a cloud of atoms is beyond the scope of this thesis; comprehensive explanations can be found in [39, 40].

## MOT Beams

The MOT beams set up an optical molasses that cool and slow the atoms down (but do not create a trapping potential on their own). They consist of 780 nm cooling light and 795 nm repump light, both circularly polarized. The cooling light is  $\approx 4\Gamma_0$  red-detuned from the  $5S_{1/2}, F=2 \rightarrow 5P_{3/2}, F'=3$  transition on the D2 line (where  $\Gamma_0$  is natural decay rate), and performs Doppler cooling on the atoms [41–44]. The repump light is resonant to the  $5S_{1/2}, F=1 \rightarrow 5P_{1/2}, F'=2$  transition on the D1 line, and depopulates the  $5S_{1/2}, F=1$  ground state so that the atoms can be continuously cooled in the cycling transition<sup>3</sup>. The energy level diagrams depicting the relevant transitions can be found in Appendix A.

The cooling light is generated from a 780 nm laser diode (Sanyo DL-7140-201S, 80 mW) locked to the  $5S_{1/2}, F=2 \rightarrow 5P_{3/2}, F'=1$  transition. For the repump, we either operate a 780 nm diode at  $\approx 70^\circ\text{C}$ , or use a 795 nm diode (QPhotonics QLP-795-150S, 150 mW). The laser is locked to the  $5S_{1/2}, F=1 \rightarrow 5P_{1/2}, F=1$ -to-2 cross-over transition<sup>4</sup>. Both lasers are then shifted to their desired frequencies using acousto-optic modulator (AOM) double-pass setups.

The cooling and repump light are combined at a polarizing beam-splitter and collected into a single-mode fiber, then split into three MOT beams. The horizontal beam travels along the length of the cuvette, while the two vertical beams are at a  $20^\circ$  angle from the vertical axis. Each beam is then retro-reflected and coupled back into the single-mode fiber to create a pair of counter-propagating MOT beams. The MOT beams have a waist of  $\approx 0.6$  mm at the trap center. The intensity of the cooling light in each beam is  $\sim 25$  mWcm<sup>-2</sup>, while the total repump intensity is  $\sim 50$  mWcm<sup>-2</sup> (the repump power is not equally distributed across the MOT beams, but this is unimportant).

## Quadrupole Magnetic Field

The gradients of a quadrupole magnetic field cause differential Zeeman shifts, which create a position-dependent restoring component in the radiative force from the cooling beams (as opposed to the velocity-dependent Doppler cooling effect).

<sup>3</sup> Many <sup>87</sup>Rb MOT setups use the 780 nm D2 transitions from the  $5S_{1/2}, F=1$  ground state for repumping. However, in some of our experiments, e.g. the transmission of a weak coherent beam (§4.5.4), we send probe and repump light (also derived from the MOT repump laser) to the atom along the same optical path, but have to filter out the repump light afterwards. Thus it was desirable to have the repump transition at a different wavelength; the interference filters we use in the collection optics (Semrock MaxLine LL01-780-12.5) have a transmission of  $\sim 6 \cdot 10^{-5}$  at 795 nm.

<sup>4</sup> The cross-over transition is not a real atomic transition, but an artefact of the saturated absorption spectroscopy technique using counter-propagating beams [39].

The quadrupole field is generated by a pair of anti-Helmholtz coils, and has a gradient of approximately 20 Gauss/cm along the X-axis and 10 Gauss/cm along the Y- and Z-axes (see Fig. 2.3). Three other pairs of Helmholtz coils compensate for any stray magnetic fields to within 10 mGauss and ensure that the magnetic field minimum, where the atomic cloud is trapped, coincides with the center of the quadrupole field.

In our setup, we obtain a  $^{87}\text{Rb}$  atomic cloud with a diameter of  $\approx 0.4$  mm. Further details on setting up the MOT can be found in Appendix B.

### 2.1.3 Far-Off-Resonant Optical Dipole Trap (FORT)

To generate an optical dipole trap, we tightly focus a far-red-detuned laser beam using the aspheric lens, creating a large intensity gradient near the focus. The interaction of the light field with the atom causes AC Stark shifts in the atomic energy levels, creating a potential well that attracts the atoms to the laser intensity maximum at the focal spot [45].

The depth of the potential is approximately proportional to  $I/\delta$ , while the scattering rate of the trap light by the atom scales with  $I/\delta^2$  [1, 46]. Here,  $I$  is intensity of the trap light at the focus and  $\delta$  is the detuning from the relevant atomic transition, which in our case is the D1 line of  $^{87}\text{Rb}$  at 795 nm. A large detuning is generally favoured so as to reduce the scattering rate of the trap light by the atom, and hence minimize the influence of the dipole trap on any prepared atomic states; however, a large optical power is then required to achieve a reasonable trap depth. We choose to use 980 nm as the dipole trap wavelength due to its large detuning ( $\sim 200$  nm), and the availability of relatively cheap and robust high-power laser diodes at 980 nm.

The 980 nm laser diode (Thorlabs L980P200J) is temperature-stabilized and free-running without an external cavity (a narrow linewidth is not necessary). The polarization of the dipole trap is set to circular<sup>5</sup>. It is important that the trap power is stabilized, as any drifts translate to changes in the AC Stark shifts and the resonance frequencies of the atomic transitions. Therefore, we measure the power of the dipole trap beam with a photodiode (Hamamatsu S5107) after it passes through the vacuum chamber and is separated from the

---

<sup>5</sup> We had previously observed that the extinction of probe light by the atom drops by a factor of two when using linear instead of circular polarization for the trap [1]. More recently, we tried to repeat the same experiment with a linearly polarized trap, but could not observe any extinction at all, while still obtaining similar results for a circularly polarized trap. It is not completely understood why the atom-light coupling seems to depend so strongly on the trap polarization; one hypothesis is that the symmetry of the circularly polarized light is better preserved in the strong focusing regime.

probe beam (see Fig. 2.1), and stabilize it to a set value using a PID loop that applies feedback to the laser diode current.

### Trap Characteristics

The dipole trap beam has a typical power of  $\simeq 45$  mW and a focal waist of  $w_D \simeq 1.8 \mu\text{m}$ , as estimated using paraxial approximation. This gives rise to an off-resonant scattering rate of  $\sim 20 \text{s}^{-1}$  [47]. We can describe the spatial distribution of the trap potential using cylindrical coordinates with

$$U(\rho, z) = -\frac{U_0}{1 + (z/z_R)^2} \exp\left[-\frac{2\rho^2}{w_D^2(1 + (z/z_R)^2)}\right], \quad (2.1)$$

where  $U_0$  is the trap depth at the focus ( $\rho = z = 0$ ), and

$$z_R = \pi w_D^2 / \lambda \quad (2.2)$$

is the Rayleigh range at the wavelength  $\lambda$ . For a sufficiently cold atom oscillating near the bottom of the potential, we can approximate the trap as a harmonic potential:

$$U(\rho, z) \approx -U_0 \left[ 1 - 2 \left( \frac{\rho}{w_D} \right)^2 - \left( \frac{z}{z_R} \right)^2 \right]. \quad (2.3)$$

The oscillation frequencies of a trapped atom in the radial and longitudinal directions are, respectively,

$$\omega_\rho = \sqrt{\frac{4U_0}{mw_D^2}}, \quad \omega_z = \sqrt{\frac{2U_0}{mz_R^2}}, \quad (2.4)$$

where  $m$  is the mass of a  $^{87}\text{Rb}$  atom. Rearranging, we obtain

$$U_0 = \frac{m\lambda}{8\pi^2} \frac{\omega_\rho^4}{\omega_z^2}. \quad (2.5)$$

In our setup, we measure trap frequencies of approximately  $\omega_\rho = 2\pi \cdot 100 \text{kHz}$ <sup>6</sup> and  $\omega_z = 2\pi \cdot 16 \text{kHz}$  using either parametric heating via modulation of the dipole trap power, or resolved sideband Raman spectroscopy (implementation details are similar to Refs. [48, 49]). Thus the trap depth given by Eq. (2.5) is  $U_0 \simeq k_B \cdot 2 \text{mK}$ . We obtain a similar value by

<sup>6</sup> In this thesis, all frequency values quoted with an accompanying factor of  $2\pi$  are angular frequencies; those without are linear frequencies.

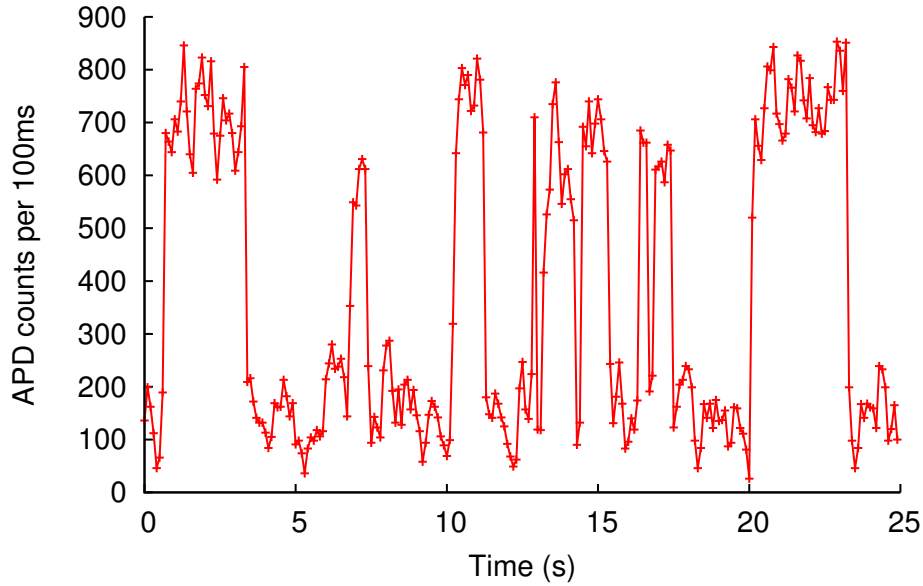


**Figure 2.4:** Typical fluorescence signal measured by an APD in the forward or backward direction, with the MOT always turned on. The signal jumps between two discrete levels: a lower background level, and a higher level corresponding to having one atom in the trap.

measuring the resonance frequency of the  $5S_{1/2}, F=2, m_F = -2 \rightarrow 5P_{3/2}, F'=3, m'_F = -3$  cycling transition, deducing the AC Stark shifts, and calculating  $U_0$  using time-dependent perturbation theory (see Appendix A).

For our trap frequencies, the characteristic oscillator lengths  $\sqrt{\hbar/m\omega}$  are  $x_\rho = 34$  nm and  $x_z = 85$  nm, which are quite small compared to the estimated focal waist of  $\simeq 0.9\mu\text{m}$  and the Rayleigh range of  $\simeq 3\mu\text{m}$  for the probe beam, respectively. Thus if an atom is sufficiently close to the vibrational ground state of the trap potential, the movement of the atom should not significantly alter the intensity of the probe field it experiences<sup>7</sup>.

### Trapping a Single Atom

The tightly focused dipole trap can only accommodate a single trapped atom due to the collisional blockade mechanism [50, 51]: when two atoms are loaded into the trap, they undergo light-assisted inelastic collisions that immediately eject both atoms from the trap [52, 53]. This leads to strongly sub-Poissonian loading statistics with only either zero or one atom in the trap.

<sup>7</sup> Ref [1] estimates the reduction of the scattering probability of probe light due to atomic motion, assuming the atom has a kinetic energy of  $k_B \cdot 100\mu\text{K}$ , to be  $< 20\%$ .

The atomic fluorescence detected in the forward and backward directions show a discrete behaviour (see Fig. 2.4), jumping between a lower background level and a higher level corresponding to having one atom in the trap [38, 50]. However, the observation of a binary on/off fluorescence signal does not exclude the possibility of multiple atoms always entering or leaving the trap together at the same time. A more definitive proof of the single-atom occupancy of the trap is to measure the normalized second-order correlation function of the light scattered by the trapped atom(s), defined classically in terms of the fluorescence intensity  $I(t)$  as [54, 55]

$$g^{(2)}(\tau) = \frac{\langle I(t)I(t+\tau) \rangle}{\langle I(t) \rangle^2} \quad (2.6)$$

where the angle brackets denote averaging over time  $t$ . For long time delays  $\tau \rightarrow \infty$ , all correlations vanish and  $g^{(2)}(\tau) \rightarrow 1$ . At shorter time scales,  $g^{(2)}(\tau)$  depends on the properties of the fluorescence source. For any classical light field,  $g^{(2)}(\tau)$  obeys the inequalities [56]

$$g^{(2)}(0) \geq 1 \quad , \quad g^{(2)}(\tau) \leq g^{(2)}(0) . \quad (2.7)$$

However, the fluorescence from a single atom is not classical: after the emission of the first photon, the atom is in the ground state and cannot immediately emit a second photon, i.e.  $g^{(2)}(0) = 0$ , which violates Eq. 2.7.

For multiple atoms, the fluorescence does not show this complete anti-bunching behaviour as the emission of the first photon from one atom does not prevent the emission of a second photon from another atom. We can generalize the correlation function to  $N$  atoms [54, 57]:

$$g_N^{(2)}(\tau) = \frac{1}{N} \left[ g_1^{(2)}(\tau) + (N-1) \left( 1 + |g^{(1)}(\tau)|^2 \right) \right] , \quad (2.8)$$

where  $g^{(1)}(\tau)$  is the correlation function describing the interference between light fields from different atoms, and  $g^{(2)}(\tau)$ , in terms of photon counting, now describes the conditional probability of detecting a second photon at time  $\tau$  after a first one was detected at  $t = 0$  [58, 59]. For the collection of fluorescence from a large solid angle, the interference effects cancel out and we have  $g_{N>1}^{(2)}(0) = \frac{N-1}{N} \geq 0.5$ .

We extract  $g^{(2)}(\tau)$  from the fluorescence signal in both collection arms (see Fig. 2.5), where we observe a Rabi frequency of 63 MHz and a damping time of  $\approx 26$  ns, compatible with the lifetime of the 5P state in  $^{87}\text{Rb}$ . Without correcting for background counts, we obtain an anti-bunching dip of  $g^{(2)}(0) = 0.26 < 0.5$ , providing further evidence that we only have a single atom in the trap [38, 57, 60].

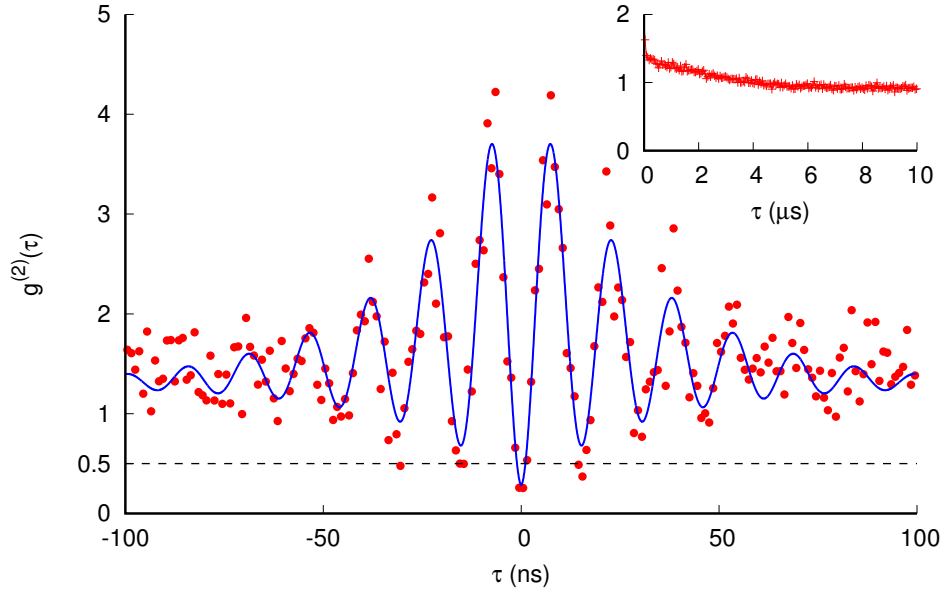


**Figure 2.5:** Normalized second-order correlation function  $g^{(2)}(\tau)$  as a function of the time delay  $\tau$  between detection events in the forward and backward directions. We identify the time delay of the minimum  $g^{(2)}$  value as  $\tau = 0$ , and use it to offset the horizontal axis for experimental delays caused by optical and electrical lines. The data is not corrected for background counts. The anti-bunching dip at  $g^{(2)}(0) = 0.26 < 0.5$  (marked by dashed line) suggests the presence of only a single atom. The smooth line is a fit<sup>8</sup> using a sinusoidal term with an exponentially decaying envelope. (Inset) At large  $\tau$ ,  $g^{(2)}(\tau) \rightarrow 1$ .

### Is There an Atom in the Trap?

With the MOT beams turned on, the clear separation of the fluorescence levels with and without the atom allows us to set a threshold count rate that indicates the presence of an atom into the trap; the detection of a count rate above this threshold can be used to trigger the start of an experimental sequence. In our experiments, the pattern generator device monitors the photon count rate and executes the experimental sequence directly (see §2.3.3). Given the single-atom fluorescence rate and the collection/detection efficiencies, it takes few 10s of ms to obtain sufficient photon counts to reliably determine the presence of the atom.

<sup>8</sup>Throughout the thesis, there are numerous instances where experimental data is fitted to a theoretical model or equation. We use the Levenberg-Marquardt (LM) Nonlinear Least-Squares Algorithm [61, 62] in various implementations, including gnuplot [63] and the python packages `scipy.optimize` [64] and `lmfit` [65]. For the LM algorithm, `lmfit` uses `scipy.optimize`, which uses the Fortran MINPACK package [66].

### Atom Lifetime and its Impact on the Experimental Sequence

The  $1/e$  lifetime of the trapped atom is on the order of a few seconds, limited by collisions with the background vapour within the vacuum chamber<sup>9</sup>. We measure the ‘survival’ rate of the atom by turning off the MOT (cooling beams and quadrupole field) upon the loading of an atom, waiting for a variable amount of time, and checking if the atom is still present (by turning on the MOT beams and monitoring the fluorescence). The survival probability decays exponentially with an increase in the waiting time. Turning off the MOT is necessary for a proper measurement as the beams and additional collisions within the cold atom cloud will influence the lifetime.

The flow of the actual experimental sequences is similar: atom loads  $\rightarrow$  sequence starts  $\rightarrow$  sequence ends  $\rightarrow$  check for atom. If the atom has survived, the data recorded during the measurement window of the sequence is valid; if not, the data is discarded as we do not know the exactly when the atom was lost from the trap, and hence cannot determine which portion of the data is valid.

Thus, a longer measurement window per sequence allows us to obtain more data within one experimental cycle, but we risk discarding more data due to a lower survival rate; a shorter sequence with more frequent checks will result in a higher proportion of valid data, but at the expense of spending more time to perform the checks. We note that the time spent performing the checks is not insignificant compared to the atom lifetime, as well as the duration of other preparation steps within the sequence. As such, the length of the sequence has to be chosen such that we have an optimal balance between the duty cycle and the collection rate of valid data.

#### 2.1.4 Preparing the Trapped Atom

By using a cycling transition to probe the atom, we effectively reduce the multi-level  $^{87}\text{Rb}$  atom to a two-level system, which greatly simplifies its study and analysis. We choose the  $\sigma^- |g\rangle = 5S_{1/2}, F=2, m_F=-2 \rightarrow |e\rangle = 5P_{3/2}, F'=3, m'_F=-3$  probe transition over its  $\sigma^+$  counterpart ( $m_F=+2$  to  $m'_F=+3$ ), as previous experiments on the same  $\sigma^+$  and  $\sigma^-$  transitions in  $^{87}\text{Rb}$  have shown a stronger extinction using a  $\sigma^-$  probe [1, 28].

The following steps, carried out upon the loading of an atom into the dipole trap, prepares the atom in the ground state of the effective two-level system. After these steps, we are ready to commence the experiment.

<sup>9</sup> The lifetime has also degraded in time: back in 2011, we measured a  $1/e$  lifetime of  $\sim 9$  s.

### Molasses Cooling

Although the MOT beams themselves constitute an optical molasses for the Rb atoms, the temperature of the MOT is higher than the cooling limit of the optical molasses technique. This is due to the breakdown of the sub-Doppler cooling mechanisms when the Zeeman shift exceeds the light shift, as well as the absorption of the MOT beams as they pass through the atom cloud [39].

Thus, upon the detection of the loading signal, we turn off the MOT quadrupole field and allow the atom cloud to dissipate, but leave the MOT beams on (without changing the frequencies or powers) for another 10 ms to perform further molasses cooling on the trapped atom<sup>10</sup>.

Using the release-and-recapture technique [67], the temperature of the trapped atom had been estimated to be  $\simeq 34 \mu\text{K}$  on a comparable setup with similar experimental conditions [48]<sup>11</sup>.

### Setting the Quantization Axis

In the absence of external fields, the atom has no preferred direction: the  $m_F$  levels are degenerate and the population is equally distributed among them. The dipole trap beam breaks this symmetry along its propagation axis and sets the quantization axis; by sending a circularly polarized probe beam of the appropriate handedness along the same axis, we can address either  $\sigma^+$  or  $\sigma^-$  transitions.

For a 2 mK trap, we estimate that the AC Stark shifts cause a splitting of  $\approx 600$  kHz between successive  $m_F$  levels of the  $5S_{1/2}, F=2$  manifold (see Appendix A). However, stray magnetic fields can still cause decoherence of the prepared state by inducing Larmor precession, which leads to a gradual mixing of the population among the  $m_F$  states. To minimize this effect, we apply a bias magnetic field of several Gauss along the quantization axis to further break the degeneracy among the  $m_F$  sublevels ( $700 \text{ kHz/Gauss} / m_F$ ).

<sup>10</sup> In the experimental sequence, the check for the presence of the atom (by turning on the MOT beams and monitoring the fluorescence) is also effectively a molasses cooling step, albeit of variable length due to the exact way we determine if the atom is present. Thus, atoms that survive a sequence and enter the next one are, in some way, already ‘pre-molasses-cooled’. For further details, refer to the full experimental sequences in §3.5.2 and §4.6.1.

<sup>11</sup> We note we could further optimize the detunings and intensities of the MOT beams during the molasses cooling step for maximum cooling, as was done in Refs. [67, 68]. However, we do not believe that the effect would be significant for our experiments. See also footnote 7 (pg. 13).

## Dark State Optical Pumping

After molasses cooling, the atomic population is distributed across  $F$  and  $m_F$  levels in the  $5S_{1/2}$  ground state. We perform dark state optical pumping to prepare the atom efficiently in the desired state  $|g\rangle = 5S_{1/2}, F=2, m_F = -2$  with minimal scattering events so as to avoid unnecessary heating of the atom. We send  $\sigma^-$  optical pumping light tuned on resonance with the  $5S_{1/2}, F=2 \rightarrow 5P_{3/2}, F'=2$  transition along the probe beam path, together with repump light tuned on resonance with the  $5S_{1/2}, F=1 \rightarrow 5P_{1/2}, F'=2$  transition. The atom continuously scatters light until it ends up in  $|g\rangle$ , where it is then decoupled from both beams as no other resonant excitations are possible; the closest allowed off-resonant transition is to the  $F' = 3$  excited state, which is  $\sim 270$  MHz detuned from the optical pumping light, and where the only possible decay path is back to  $|g\rangle$  anyway.

We typically perform optical pumping for 5–10 ms. The optical pumping light and repump light are derived from the same lasers as the MOT cooling and repump lasers, respectively, and are shifted to the desired frequencies via separate AOMs. The power of the optical pumping and repump beams entering the cuvette is on the order of 10 pW each.

## 2.2 Four-Wave Mixing

The purpose of the four-wave mixing (FWM) setup is to produce heralded single photons which are compatible with the single atom in terms of their spectral and temporal properties.

We perform FWM in a dense, cold ensemble of  $^{87}\text{Rb}$  atoms in a MOT and generate photon pairs. The detection of one photon of the pair heralds the presence of the other, which is used to interact with the single atom system. By choosing to work with the same atomic species, we can conveniently generate photons with similar wavelengths and bandwidths compared to the spontaneously emitted photons from the single  $^{87}\text{Rb}$  atom,

The capabilities of the FWM setup are reported in Refs. [33–36], and further theoretical discussions and technical details can be found in Refs. [2, 69]. Here we just provide a brief description of FWM process and an overview of the setup, before discussing the relevant properties of the generated photons.

### 2.2.1 Working Principle

FWM is a third-order nonlinear parametric process involving the interaction of four optical fields in a nonlinear medium, e.g. nonlinear fibers [70, 71], hot vapour cells [72, 73], and cold atomic ensembles [74–76].

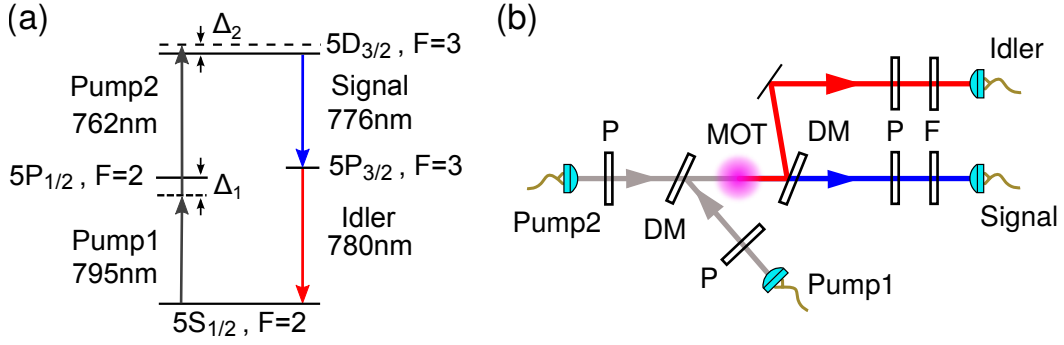


**Figure 2.6:** (a) Energy level scheme of the FWM process. We fix the detuning  $\Delta_1 = 30$  MHz, while  $\Delta_2 \sim 4$  MHz is an optimizable parameter. (b) Basic schematic of the FWM setup. Two pump beams (795 nm, 762 nm) are overlapped inside a cold cloud of  $^{87}\text{Rb}$  atoms in a MOT, generating signal (776 nm) and idler (780 nm) photon pairs. The detection of a signal photon heralds the presence of a single photon in the idler mode. DM: Dichroic mirrors, F: interference filters, P: polarizers.

The response of the medium is characterised by the third-order nonlinear susceptibility  $\chi^{(3)}$ . Being a parametric process, the initial and final quantum states of the medium are identical [77]. This implies the conservation energy and momentum between the four participant fields.

The level scheme of the FWM process is shown in Fig. 2.6a. Energy conservation is given by the frequencies of the pump, signal and idler modes:

$$\omega_1 + \omega_2 = \omega_S + \omega_I . \quad (2.9)$$

In a spatially extended medium, as in the case of our atomic ensemble, momentum conservation is given by the translational symmetry of the medium, giving rise to the phase matching condition:

$$\vec{k}_1 + \vec{k}_2 = \vec{k}_S + \vec{k}_I , \quad (2.10)$$

where the terms represent the wave-vectors of pump1, pump2, signal and idler modes, respectively. In the FWM setup, the phase matching condition is met by overlapping the pump beams in a co-propagating geometry (see Fig. 2.6b), which also simplifies the collection of the signal and idler modes.

The signal and idler photons are generated as a correlated pair via the cascade decay; as such, the detection of a photon in the signal mode heralds the presence of a single photon in the idler mode (and vice versa).

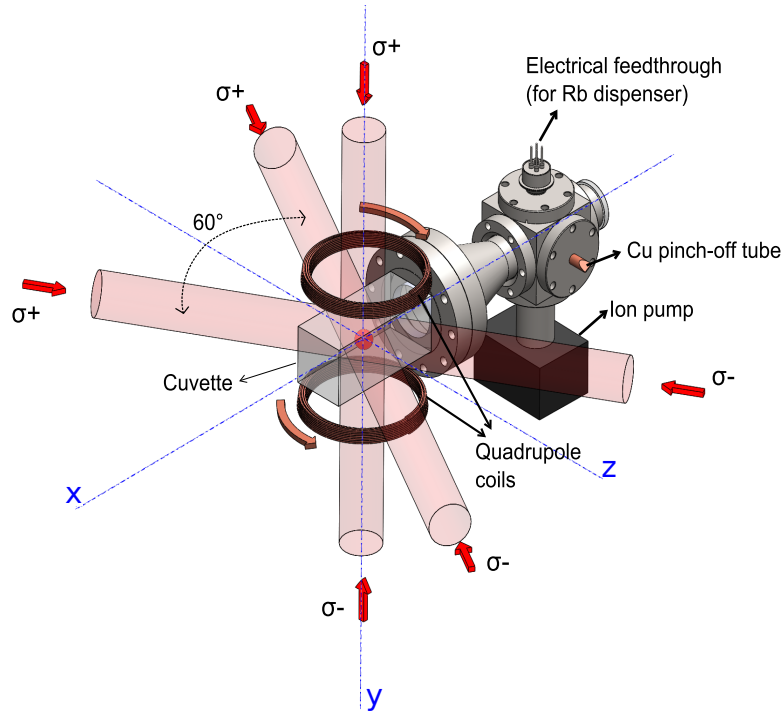


**Figure 2.7:** The MOT apparatus of the FWM setup, showing the vacuum chamber, MOT beams, and quadrupole field coils. The two horizontal pairs of beams (in the x-z plane) are  $60^\circ$  apart; the vertical pair passes through the coils (along the y axis). Figure credit: [2]

## 2.2.2 Setup

### Magneto-Optical Trap

The centerpiece of the FWM setup is a six-beam MOT which cools and traps a cloud of cold  $^{87}\text{Rb}$  atoms in a glass cuvette, which is attached to a vacuum chamber. The MOT beam configuration is slightly different compared to that in the single atom setup, with six individual beams (instead of three retro-reflected beams) at different angles (see Fig. 2.7). The MOT beams are also larger (diameter  $\approx 15$  mm) and brighter (cooling, repump light intensities at  $40\text{--}50\text{ mWcm}^{-2}$ ,  $5\text{--}8\text{ mWcm}^{-2}$  per beam). The optical density (OD) of the atom cloud increases with a higher quadrupole field gradient, which can be varied up to  $25\text{ Gauss/cm}$  (radial) and  $50\text{ Gauss/cm}$  (axial), corresponding to a coil current of  $12\text{ A}$ . The resultant atomic cloud is roughly  $1\text{ mm}$  in diameter.

The MOT transitions are at  $780\text{ nm}$ , along the D2 line. The cooling light is  $4\Gamma_0$  red-detuned from the  $5S_{1/2}, F=2 \rightarrow 5P_{3/2}, F'=3$  transition, while the repump light is resonant with the  $5S_{1/2}, F=1 \rightarrow 5P_{3/2}, F'=2$  transition. They are generated using separate diode

lasers, with the cooling light being further amplified by a tapered amplifier (2W, Eagleyard EYP-TPA-0780-02000-4006-CMT03-0000) to obtain the required optical power.

### Four-Wave Mixing

Fig. 2.6a shows the FWM level scheme. The 795 nm and 762 nm pumps excite the atoms from  $5S_{1/2}, F=2 \rightarrow 5P_{1/2}, F'=2 \rightarrow 5D_{3/2}, F''=3$ . The detunings  $\Delta_1 = 30$  MHz (fixed) and  $\Delta_2 \sim 4$  MHz (optimized as necessary during the experiment) are chosen to minimize incoherent scattering without compromising too much on the photon pair rate and the heralding efficiency (defined as the probability of detecting the corresponding single photon after a heralding event).

Besides the cascade decay via the  $5P_{3/2}, F=3$  intermediate state (as shown in Fig. 2.6a), there exists an alternative decay path via the  $5P_{3/2}, F=2$  level; we denote them as X and Y, respectively. The interference of the two paths would result in quantum beats at the difference frequency of 266 MHz between the two intermediate states [36]. To avoid this interference effect and ensure that the collected single photons are not of two different frequencies, we suppress the Y decay by choosing the following polarization settings: we set the 795 nm and 762 nm pumps at horizontal  $|H\rangle$  and vertical  $|V\rangle$  polarizations, respectively, and project the signal mode onto  $|H\rangle$  and the idler mode onto  $|V\rangle$ . By doing so, the generation amplitude of the Y decay becomes a factor of 35 smaller than that of X [36], and is effectively suppressed.

During the photon pair generation, the atoms can decay to the  $5S_{1/2}, F=1$  ground state and be decoupled from the FWM process. Thus, we use an additional 795 nm repump beam tuned to the D1  $5S_{1/2}, F=1 \rightarrow 5P_{1/2}, F'=2$  transition to depopulate the  $F=1$  ground state.

The above-mentioned beams are also generated via similar diode laser setups<sup>12</sup>.

### Pump & Collection Modes

The pump, signal and idler modes co-propagate through the atom. We use narrowband interference filters as dichroic mirrors to overlap the pump beams and to separate the signal and idler fields (see Fig. 2.6b). Additional interference filters in the collection arms filter out the pump light. The pump and collection modes are slightly focused onto the MOT cloud with a beam diameter of  $\sim 0.8$  mm, approximately equal to the size of the atomic ensemble.

The 795 nm repump beam is orthogonal to the pump beams.

<sup>12</sup> We specially mention that the 762 nm pump light is generated with an Eagleyard EYP-RWE-0790-04000-0750-SOT01-0000 gain chip, and frequency-locked with a slightly modified excited-state spectroscopy setup.

## Experimental Sequence

If light from the MOT beams were present during the FWM process, a lot of incoherently scattered light will be collected in the signal and idler modes. To avoid this, the setup continuously alternates between a MOT cooling phase to cool and replenish the atom cloud, and a photon pair generation phase.

During the cooling phase, the MOT beams are turned on, and the pump beams are turned off; during the pair generation phase, the MOT beams are off and the pump beams are turned on. The quadrupole magnetic field and the 795 nm repump beam are always kept on. This cycling sequence is not synchronized with the single atom setup.

### 2.2.3 Single Photon Properties

The generated photons are a very good approximation of a single photon state, with a strong anti-bunching signal of  $g^{(2)}(0) < 0.05$ , and are narrowband with a Fourier-transform-limited spectrum (i.e. the photons have the minimum temporal width for the given spectral bandwidth) [33, 35]<sup>13</sup>.

In our experiments, we detect the 776 nm signal photon as a herald, and use the 780 nm idler photon to interact with the single atom system. As the idler photons are resonant with the ground state transition (after compensating for the AC Stark shift and Zeeman shift that the single atom experiences), they can be used to excite the single atom efficiently.

When heralding on the detection of a signal photon, the idler photons have an exponentially decaying profile, with a decay time  $\tau_f$  shorter than the natural lifetime of the transition due to collective effects in the atomic ensemble [78, 79]. A typical measurement is shown in Fig. 2.8. We can vary  $\tau_f$  from 4.5 ns to 13.5 ns by changing the optical density (OD) of the atom cloud via the quadrupole field gradient.

In general, raising the field gradient increases the OD, shortens  $\tau_f$ , and increases the pair rate. Beyond an OD of  $\sim 32$  (coil current 12 A),  $\tau_f$  does not decrease further below 4.5 ns, most likely due to the limit in creating a denser atomic cloud simply by increasing the field gradient. On the other hand, if we lower the OD,  $\tau_f$  approaches the natural transition lifetime of 26.2 ns, which makes the photon more compatible with the atom, but for  $\tau_f < 13.5$  ns the pair rate is too low to be experimentally useful.

<sup>13</sup> These two properties were explicitly shown only for the reversed FWM scheme: sending pump beams at 780 nm and 776 nm, generating signal and idler photons at 762 nm and 795 nm. However, since the setup is otherwise identical, we assume that these properties still apply.

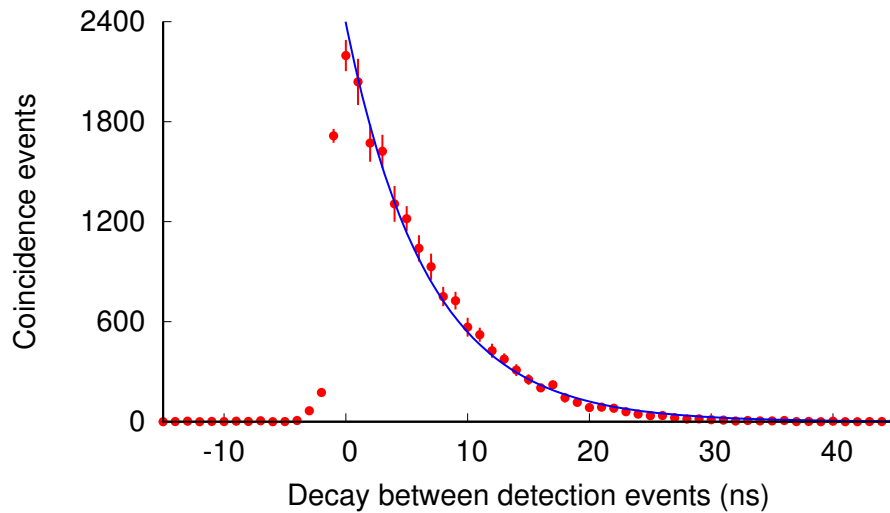


**Figure 2.8:** Histogram of coincidence events as a function of the time delay between the detection of signal and idler photons, with the signal photons serving as the herald. An exponential fit (solid line) indicates an idler photon decay time of  $\tau_f = 6.7$  ns. The error bars represent Poissonian statistics.

## 2.3 Common instruments

Here we describe some of the instruments that are common to both the single atom and FWM setups. Unless stated otherwise, these instruments are developed and built in-house within our research group.

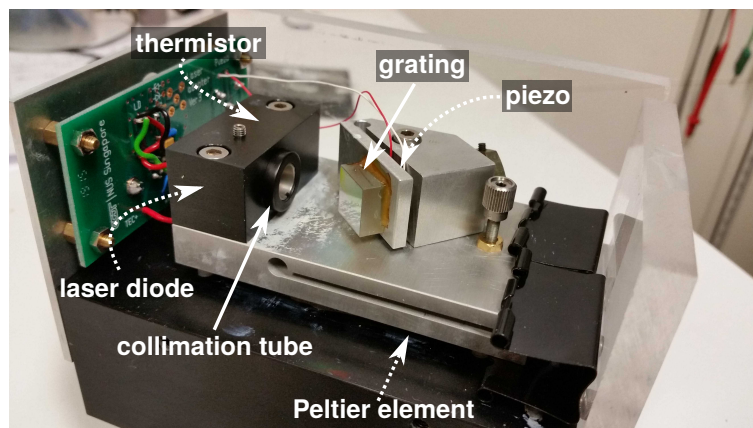


**Figure 2.9:** Partially uncovered ECDL box.

### 2.3.1 Coherent Light Sources

#### Diode Lasers

Diode lasers are a convenient source of narrow-band coherent light used to address and manipulate the internal electronic states of the atoms. Laser diodes for typical wavelengths used in our experiments have wider applications in industry and have been extensively engineered, thus they are reliable and relatively cheap. For example, 780 nm (D2 transition in  $^{87}\text{Rb}$ ) diodes are used in CD players, while 980 nm (for the dipole trap) lasers have medical applications and are used as pumps for pump solid state lasers. Specifics of the different laser diodes used are mentioned in the detailed setup descriptions (see §2.1, §2.2).

The laser diodes are mounted in home-built External Cavity Diode Laser (ECDL) systems in a Littrow configuration<sup>14</sup> [80, 81] (see Fig. 2.9). The external cavity narrows the emission linewidth by providing feedback to the laser diode and selecting only a single frequency mode. The cavity length is  $\approx 3$  cm and is formed by the partial reflection off a diffraction grating (usually Thorlabs GR13-1850, 1800 lines / mm, 500 nm blaze). Rough wavelength tuning is achieved by changing the temperature with a Peltier element and stabilizing it with a PID loop, while fine tuning is achieved by adjusting the external cavity length with a piezoelectric actuator (Thorlabs AE0505D08F, tuning sensitivity  $\sim 0.4 - 0.6$  MHz / mV).

The ECDL is housed in an enclosed box to reduce the effects of external temperature fluctuations and airflows. The elliptical beam from the ECDL, which has already been collimated (collimation tube, Thorlabs LT230-B), is reshaped into a circular Gaussian mode with a pair of anamorphic prisms. Optical isolators ( $\geq 30$  dB) further improve laser stability by suppressing unwanted optical feedback to the laser diode.

On the single atom setup, we use Thorlabs LDC200C series laser diode drivers, with the temperature stabilization provided by a separate analog PID loop. For the FWM setup, we use home-made laser driver boards which integrate both the current driver and a digital PID loop for temperature stabilization.

#### Laser Locking and Tuning

The lasers are frequency-locked using Doppler-free saturated-absorption frequency-modulation (FM) spectroscopy [82, 83] to transitions in  $^{87}\text{Rb}$  in an atomic vapour cell. The spectroscopy setup generates a feedback signal to the piezoelectric element controlling the grating (and hence the external cavity length) on the laser.

<sup>14</sup>The exception is the 980 nm laser used for the dipole trap, which does not require a narrow linewidth and thus is free-running without an external cavity.

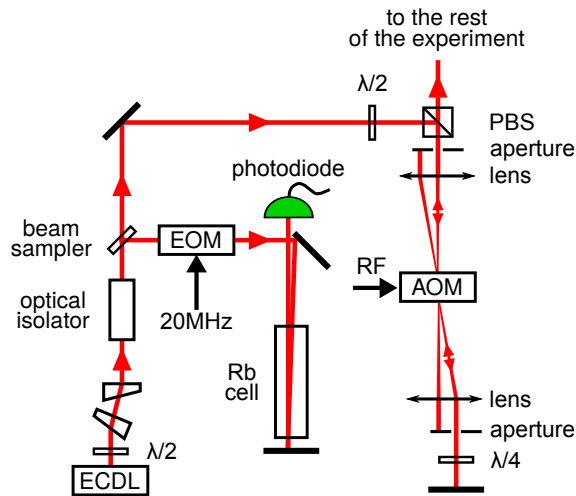


**Figure 2.10:** A typical laser setup. The HWP just after the ECDL minimizes losses through the anamorphic prism pair. A portion of the laser output is diverted to the FM spectroscopy setup, either with a beam sampler (as shown) or with a HWP and PBS. The retro-reflecting beams passing through the Rb cell are separated via a slight angular displacement (as shown) or with a QWP and PBS. We typically use a 150 mm lens pair to focus the beam onto the AOM, and apertures to transmit only the correct first order diffracted beam. More details can be found in the main text. AOM, EOM: acousto- and electro-optic modulators,  $\lambda/2$ ,  $\lambda/4$ : half- and quarter-wave plates (HWP and QWP, respectively), PBS: polarizing beam-splitter.

The resulting laser linewidth is  $< 1$  MHz, which we verify using beat note measurements. A beat note can be measured by combining two independent laser beams of the same wavelength (with a slight frequency offset between them, typically 200 MHz applied using an AOM) at a beam-splitter, and measuring the output with a fast photodetector connected to a spectrum analyzer. There will be a peak in the beat note spectrum at the frequency difference between the beams, which is given by the convolution of the linewidths of both lasers. By using three independently locked lasers and performing three pairs of beat note linewidth measurements between them, we can deduce the linewidth of each laser<sup>15</sup>.

Fig. 2.10 shows a typical laser setup. A portion of the laser output (typically a few  $100 \mu\text{W}$ ) is phase-modulated with a local oscillator (LO) at 20 MHz using an electro-optic modulator (EOM), which consists of a  $\text{LiNbO}_3$  crystal in a resonant tank circuit. The beam passes through the atomic vapour cell and is retro-reflected before detection by a

<sup>15</sup> Alternatively, we can split a single laser beam using a beam-splitter, and apply a large optical path length difference between the two outputs by sending one of the outputs through a long fiber that exceeds the coherence length of the laser (typically a few 100 m). We then apply the frequency shift at the output of the long fiber, recombine the beam with the second output of the first beam-splitter, and perform the measurement as stated above. In this case, the recombined beams are uncorrelated but have the same linewidth, and thus the laser linewidth can be obtained with a single beat note measurement.

photodiode; this counter-propagating geometry gives us a Doppler-free signal. A phase-sensitive measurement of the photodiode signal with respect to the 20 MHz LO produces an error signal, which is then fed to an analog PID loop to generate the feedback signal.

Further tuning of the laser frequency is achieved with AOMs in a single- or double-pass setup [84] (the latter is shown in Fig. 2.10). The AOMs also act as switches for turning on/off the beams with an extinction of  $\sim 40$  dB (double-pass). Depending on the required modulation frequency, we use either 80 MHz, 200 MHz (Crystal Technology [now Gooch & Housego] 3200-124 and 3080-122, respectively), or 130 MHz (IntraAction ATM-1331A2) AOMs.

### 2.3.2 Avalanche Photodetectors (APDs)

The avalanche photodetectors (APDs) are single photon counters and are used to measure the optical outputs of our experimental setups. Our main considerations for choosing an APD are: dark count rate, efficiency, and jitter time. Three types of APDs are used for the work presented in this thesis:

- Home-made APD units based on passively-quenched Perkin Elmer C30902SH diodes with fiber pigtailed<sup>16</sup> (see Fig. 2.11). The attached circuit board also controls a Peltier element and maintains the temperature at  $-30^\circ\text{C}$ . The units used in the experiments have a dark count rate of  $\approx 150\text{ s}^{-1}$ , an efficiency of  $\approx 50\%$  at 780 nm, and a timing jitter of 0.6 to 1 ns. Most measurements are performed with these APDs.
- Perkin Elmer SPCM-AQR-15 modules based on actively-quenched Si APD diodes. We focus the light collected from single-mode fibers onto the diode via a pair of lenses. They have a dark count rate of  $\approx 50\text{ s}^{-1}$ , an efficiency of  $\approx 60\%$  at 780 nm, and a timing jitter of 0.4 ns. These APDs are used to obtain the main results of the scattering experiment in §4.7.
- Micro Photon Devices PDM PD-050-CTC-FC modules based on actively-quenched Si APD diodes with a pre-aligned fiber receptacle. The dark count rate is  $< 100\text{ s}^{-1}$ . Despite its low efficiency of  $\approx 15\%$  at 780 nm, we specifically use this APD to characterize the short excitation pulse (see §3.3.2) due to its low jitter time of 40 ps.

<sup>16</sup> The fibers have a FC/PC connector, which causes some light to be back-reflected. This can be an issue for very weak signals, e.g. the scattering experiment (Chapter 4), where we collect a similar number of probe photons scattered by the atom (signal) and by the fiber (noise) when using these APDs. Thus, we use other APDs to perform the scattering experiment.

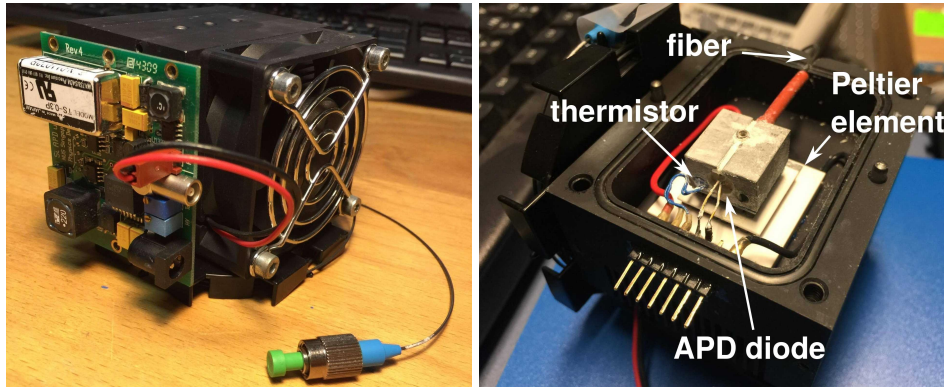


**Figure 2.11:** Exterior (**left**) and interior (**right**) of a home-made APD unit. Photo credit: [3]

We note that the timing uncertainty of the measurements are nonetheless limited by the resolution of the timestamp unit (nominally 125 ps).

Whenever it was necessary to include the APD efficiency directly in our data analysis, we perform a calibration measurement on the detector (see Appendix D).

### 2.3.3 Electronics

#### Rubidium Clock

A rubidium clock (SRS FS725, nominal accuracy  $\pm 5 \cdot 10^{-11}$ ) serves as the frequency reference for all the electronic devices that require an accurate clock signal input. The clock unit outputs a 10MHz reference signal, which we then separately duplicate and split among the recipient devices as needed. Examples of such devices are the pattern generator, direct digital synthesizer (DDS) board, and the timestamp unit. These devices typically use this reference clock to generate an internal clock signal of a different frequency.

#### Pattern Generator

The home-made USB-programmable pattern generator unit implements the experimental sequences by controlling various devices via electrical logic signals, according to a pre-programmed pattern. The tasks performed by these signals include switching beams on/off by controlling the acousto-optic modulators (AOM)s, changing the currents in a magnetic field coil, being recorded directly on the timestamp unit as a timing signal, etc. The FWM and single atom setups each employ a pattern generator which is not synchronized to the other. On the FWM setup, the device continuously alternates between the MOT cooling and photon pair generation steps *ad infinitum*. For the single atom setup, it uses APD clicks from

the detection of atomic fluorescence to determine the presence of an atom in the trap, and triggers the main sequence when the count rate rises above a set threshold.

The device is based on a lookup table implemented using fast RAM (32 Mbit, 8 x Cypress CY7C1049DV33 chips, 10 ns access time). The different steps of the pattern control which of the 48 output bits are turned on. The duration of each step, which must be an integer multiple of two internal clock cycles, also determines the amount of memory it occupies on the RAM chips. As such, due to the finite RAM capacity, the time-step resolution is limited by the maximum allowable length of the pattern: the device on the FWM setup uses a 100 MHz clock frequency, which gives a time-step resolution of 20 ns, but the full sequence is typically limited to  $<100$  ms. To accommodate longer experimental sequences, the pattern generator on the single atom setup uses a 1 MHz clock with a minimum time-step of  $2 \mu\text{s}$  for the main HOM and scattering experiments.

### **Direct Digital Synthesizer Board (DDS)**

The home-made USB-programmable Direct Digital Synthesizer (DDS) boards are based on the Analog Devices AD9958 chip. They serve as switchable and tunable frequency sources, and are primarily used to generate RF fields of up to 250 MHz at -2 dBm (into  $50 \Omega$ ), which are subsequently amplified and used to drive the AOMs.

### **Timestamp Unit**

The home-made timestamp unit has 4 input channels and records the arrival time of input signals (specifically, the falling edge of a NIM pulse) with a nominal timing resolution of 125 ps. The recorded data is continuously flushed to a computer via a USB interface. It is capable of registering simultaneous signals in different channels, but after each signal is recorded (on one or multiple channels), the device has a dead time of  $\approx 200$  ns during which no further signals can be recorded. Therefore, in order to perform coincidence measurements, the signals (usually APD clicks) have to reach the timestamp unit sufficiently separated in time. This can be achieved with a delay cable on one of the input channels.

The nominal 125 ps resolution is achieved by multiplying a 10 MHz input reference from the rubidium clock to a 500 MHz clock signal (2 ns period), which is further subdivided into 16 “bins” via a phase interpolation stage, i.e. these bins provide the high-resolution timing information within each 2 ns clock cycle. However, the subdivision is not strictly uniform, and this results in a small oscillation of period 2 ns on top of the expected signal in our coincidence measurements.

---

For the scattering experiment, this directly interferes with the time-resolved dynamics of the atom-light interaction which we want to study, and could constitute a significant error. As such, for the scattering experiment data only, we correct for this during post-processing (see Appendix C for details) at the expense of an increase in the timing uncertainty of each timestamp. Nevertheless, for those coincidence measurements, we expect the total timing uncertainty to be dominated by the combined timing jitter of both APDs ( $\approx 800$  ps).



# Chapter 3

## Hong-Ou-Mandel Interference Experiment

This chapter presents the Hong-Ou-Mandel (HOM) interference between heralded single photons produced via FWM and triggered single photons generated via spontaneous decay of the single atom. We first present a theoretical formulation of the interference effect and describe how we utilize the single atom as a single-photon source. Next, we introduce the full experimental setup and sequence. Finally, we show the experimental results, including the well-known ‘HOM dip’.

### 3.1 Introduction

We consider two photons to be indistinguishable when they have identical polarizations, frequencies, and spatio-temporal modes. When two such photons are simultaneously incident on a 50:50 beam-splitter, the HOM interference effect [85] causes them to always emerge from the same (but random) output port. Although it was initially developed as a sensitive tool for timing measurements, this effect also provides a fundamental primitive for the coherent interfacing of separate quantum systems via their emitted photons [86], as opposed to their direct interaction [87, 88]. It is the basis of quantum teleportation [89–91] and entanglement swapping [92, 93].

HOM interference has been demonstrated using single photons generated from separate copies of the same quantum system: nonlinear crystals [94–96], neutral atoms [97, 98], with a particularly high visibility between two  $^{87}\text{Rb}$  atoms [99], quantum dots [100, 101], NV centers in diamond [102], single molecules [103, 104], atomic ensembles [105], trapped ions [106], and superconducting qubits [107]. The use of identical sources ensures the

generation of compatible photons with matching temporal shapes and bandwidths, allowing for a very high visibility when the sources are accurately synchronized.

However, such compatible photons are harder to generate using disparate sources. Prior to this work, there have been few experimental demonstrations of HOM interference with single photons originating from different physical processes: a single quantum dot and parametric down-conversion in a nonlinear crystal [108], and different parametric effects in nonlinear optical materials [109]. These two demonstrations rely on spectral filtering in order to match the temporal shape and the bandwidth of the generated photons, at the expense of drastically reducing the photon rate.

Here, we perform a HOM interference experiment without spectral filtering of the photons (except correcting for background noise). Aside from demonstrating the intrinsic compatibility of the single atom and FWM systems, the results allow us to understand the connection between the two separate setups, as well as the limitations caused by the mismatch between the single photons from both systems.

### 3.1.1 Idea of the Experiment

The key concept of the experiment is illustrated in Fig. 3.1a. Apart from obtaining heralded single photons from the FWM setup, we also use the single atom as a single-photon source via scattering from a triggered excitation pulse. We combine the generated single photons on a 50:50 beam-splitter and measure the outputs with APDs. If the two photons are compatible, the HOM will decrease the rate of coincident detection events at the outputs, as compared to having two completely distinguishable photons.

We can already expect to observe significant two-photon interference by considering a few basic properties of both systems:

1. The photons have compatible frequencies as they are generated from the same 780 nm  $5S_{1/2}, F=2 \rightarrow 5P_{3/2}, F'=3$  transition (see Fig. 3.1b,c).
2. Both photons have a decaying exponential temporal envelope.
3. Both temporal envelopes have similar time constants:  $\tau_s = 26.2$  ns for the single atom source, and  $4.5$  ns  $\lesssim \tau_f \lesssim 13.5$  ns for the FWM source. With  $\tau_f \approx 13.5$  ns, we predict an interference visibility of 90% (see Eq. 3.19).

To synchronize the experiment and ensure the temporal overlap of the photons at the HOM beam-splitter, the detection of the heralding photon at the FWM source also serves as the trigger for generating the excitation pulse at the single atom source.

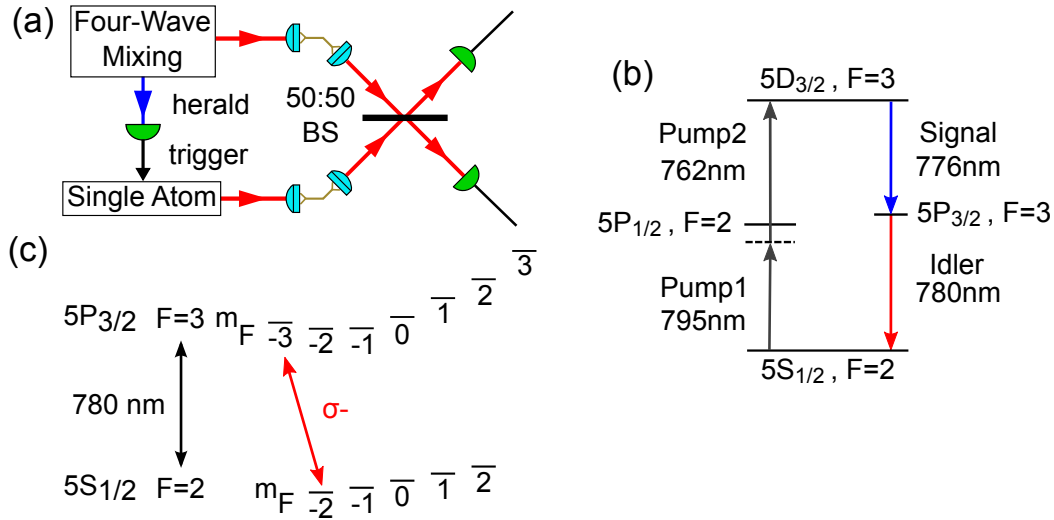


**Figure 3.1:** (a) Schematic representation of the Hong-Ou-Mandel interference experiment. Single photons are obtained by heralding on one photon of a time-correlated photon pair generated via FWM. The heralding event triggers the generation of a single photon by a single atom. The single photons from each setup interfere at a 50:50 beam-splitter, and are detected by APDs at the outputs. (b) Simplified level scheme of the FWM process. The signal photon serves as the herald, and the idler photon is used for the interference experiment. (c) Level scheme for the single atom in the dipole trap and electronic transition used for exciting the single atom.

## 3.2 Theory

### 3.2.1 A Little Intuition

To understand the HOM interference effect, consider two photons entering a 50:50 beam-splitter simultaneously. Depending on whether each photon is transmitted or reflected, there are four possible outcomes (see Fig. 3.2): 1) Photon 1 is reflected and photon 2 is transmitted; 2) Both photons are transmitted; 3) Both photons are reflected; 4) Photon 1 is transmitted and photon 2 is reflected.

The conservation of energy requires that there be a relative phase shift of  $\pi$  between the transmitted and reflected paths of a 50:50 beam-splitter [110]. For identical photons, outcomes 2 and 3 become indistinguishable, and the relative phase difference ensures that

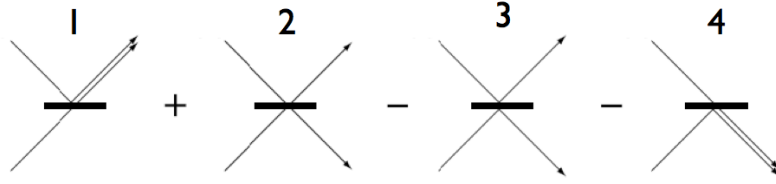


**Figure 3.2:** Four possible outcomes of two photons entering a 50:50 beam-splitter simultaneously. If both photons are indistinguishable, the probability amplitudes of outcomes 2 and 3 cancel out, and both photons will exit the beam-splitter from the same (but random) side; this is the HOM effect. Image: [4]

their probability amplitudes destructively interfere<sup>1</sup> and cancel out, thus both photons will exit the beam-splitter from the same random output port.

For a more mathematical description, we start with a simple Fock-state picture. Energy conservation implies that the action of a lossless beam-splitter can be expressed via a unitary matrix  $U$  [54, 112, 113]:

$$U = \begin{bmatrix} t & -r^* \\ r & t^* \end{bmatrix}, \quad (3.1)$$

where  $r$  and  $t$  are the reflection and transmission coefficients, and

$$|r|^2 + |t|^2 = 1 \quad (3.2)$$

expresses the lossless property of the beam-splitter. In terms of field operators, we then have

$$\begin{bmatrix} b_1 \\ b_2 \end{bmatrix} = U \begin{bmatrix} a_1 \\ a_2 \end{bmatrix} = \begin{bmatrix} t & -r^* \\ r & t^* \end{bmatrix} \begin{bmatrix} a_1 \\ a_2 \end{bmatrix}, \quad (3.3)$$

where  $a_{1,2}$  and  $b_{1,2}$  are the annihilation operators for the input and output modes, respectively. Via the usual commutation relations  $[a, a^\dagger] = 1$ , we obtain

$$\hat{a}_1^\dagger = t\hat{b}_1^\dagger + r\hat{b}_2^\dagger \quad (3.4)$$

$$\hat{a}_2^\dagger = -r^*\hat{b}_1^\dagger + t^*\hat{b}_2^\dagger. \quad (3.5)$$

<sup>1</sup> Another explanation for the destructive interference is derived from the Fresnel equations [111], according to which reflection causes a phase shift only when light passing through a material of low refractive index is reflected at a material of high refractive index. This argument works well for plate beam-splitters with a dielectric coating, but becomes tricky when extended to conductive coatings or stratified media, while the energy conservation argument is more general and would still hold.

For an input state having one photon in each input port, i.e.  $|1, 1\rangle = \hat{a}_1^\dagger \hat{a}_2^\dagger |0, 0\rangle$ , the resulting state is

$$\hat{a}_1^\dagger \hat{a}_2^\dagger |0, 0\rangle = \left( t \hat{b}_1^\dagger + r \hat{b}_2^\dagger \right) \left( -r^* \hat{b}_1^\dagger + t^* \hat{b}_2^\dagger \right) |0, 0\rangle \quad (3.6)$$

$$= -r^* t |2, 0\rangle + (|t|^2 - |r|^2) |1, 1\rangle + r t^* |0, 2\rangle . \quad (3.7)$$

For a 50:50 beam-splitter,  $|r| = |t|$  and the  $|1, 1\rangle$  term cancels out, thus both photons always emerge together from either output port with equal probabilities.

The above approach is valid for a particular mode of the electromagnetic field, but is not well-suited for describing the full time-resolved interference involving photons which are localised in space and time. To account for this, our mathematical treatment will adopt a multi-mode approach in the following sections.

### 3.2.2 Coincident Photon Detection at the Beam-Splitter Outputs

To describe single-photon wavepackets in the space-time domain, we use a mode function written as a product of a real amplitude term and a complex phase:

$$\psi_j(t) = \xi_j(t) \exp[-i\Phi_j(t)], \quad (3.8)$$

with the amplitude envelope normalised to  $\int |\xi_j(t)|^2 dt = 1$ .

Experimentally, we study the HOM effect using photons with parallel ( $\parallel$ , interfering) or orthogonal ( $\perp$ , non-interfering) polarizations. To quantify the interference, we measure the probability of coincidences between the detection events at the two 50:50 beam-splitter output ports, which can be written for the interfering case as [114, 115]

$$G_{\parallel}(\Delta t_{12}) = \frac{1}{4} \int_{-\infty}^{\infty} |\psi_1(t) \psi_2(t + \Delta t_{12}) - \psi_1(t + \Delta t_{12}) \psi_2(t)|^2 dt , \quad (3.9)$$

where  $\Delta t_{12}$  is the delay between detection events. The minus sign has its roots in the relative phase difference between transmission and reflection in the beam-splitter<sup>2</sup>. We can rewrite Eq. (3.9) as

$$G_{\parallel}(\Delta t_{12}) = G_{\perp}(\Delta t_{12}) - F(\Delta t_{12}) , \quad (3.10)$$

<sup>2</sup> To see this explicitly via the continuous-mode operator formalism for the beam-splitter, refer to Ref [116].

consisting of a non-interfering term  $G_{\perp}(\Delta t_{12})$  and an interfering term  $F(\Delta t_{12})$ . The first term

$$G_{\perp}(\Delta t_{12}) = \frac{1}{4} \int_{-\infty}^{\infty} |\xi_1(t)\xi_2(t+\Delta t_{12})|^2 + |\xi_1(t+\Delta t_{12})\xi_2(t)|^2 dt \quad (3.11)$$

is the convolution of the photon amplitudes, and is independent of the phase; it corresponds to our observations for non-interfering, orthogonally polarized photons. The second term describes the interference between the photons:

$$F(\Delta t_{12}) = \frac{1}{2} \int_{-\infty}^{\infty} \xi_1(t)\xi_2(t+\Delta t_{12})\xi_1(t+\Delta t_{12})\xi_2(t) \cdot \phi(t, \Delta t_{12}) dt \quad , \quad (3.12)$$

where

$$\phi(t, \Delta t_{12}) = \cos[\Phi_1(t) - \Phi_1(t + \Delta t_{12}) + \Phi_2(t + \Delta t_{12}) - \Phi_2(t)] \quad . \quad (3.13)$$

The phase term  $\phi(t, \Delta t_{12})$  is always equal to 1 unless  $\Phi_1$  and  $\Phi_2$  display a different time evolution, e.g. when the photons have different central frequencies.

We can now define a HOM interference visibility  $V$  as

$$V = 1 - P_{||}/P_{\perp} \quad (3.14)$$

where the total probability  $P$  is obtained via  $P = \int_{-\infty}^{\infty} G(\Delta t_{12})d(\Delta t_{12})$ . From the normalisation conditions we obtain

$$P_{\perp} = \int_{-\infty}^{\infty} G_{\perp}(\Delta t_{12})d(\Delta t_{12}) = \frac{1}{2} \quad , \quad (3.15)$$

and the visibility reduces to the overlap integral between the two photon amplitudes [54]:

$$V = \left| \int_{-\infty}^{\infty} \xi_1(t)\xi_2(t)dt \right|^2 \quad , \quad (3.16)$$

assuming  $\phi(t, \Delta t_{12}) = 1$  in Eq. (3.12). For identical photons  $\xi_1(t) = \xi_2(t)$ , we obtain a full visibility  $V = 1$ .

### 3.2.3 Exponentially Decaying Photons

Here we consider the experimentally relevant case of two exponentially decaying photons which are identical except for their coherence times:

$$\xi_i(t) = \sqrt{\frac{1}{\tau_i}} e^{-\frac{t-t_i}{2\tau_i}} \Theta(t-t_i) \quad \text{with } i = f, s \quad , \quad (3.17)$$

where  $\tau_{f,s}$  are the coherence times of the photons from the FWM and single atom sources, respectively,  $t_{f,s}$  correspond to the peaks of their respective exponential envelopes, and  $\Theta(t)$  is the Heaviside step function. The visibility is

$$V = \frac{4\tau_f\tau_s}{(\tau_s + \tau_f)^2} \cdot \begin{cases} e^{-\Delta T/\tau_s} & \text{for } \Delta T \geq 0 \\ e^{\Delta T/\tau_f} & \text{for } \Delta T < 0 \end{cases}, \quad (3.18)$$

where  $\Delta T = t_f - t_s$ . The maximum visibility occurs at  $\Delta T = 0$ , i.e. when the peaks of the temporal envelopes coincide, giving

$$V = \frac{4\tau_f\tau_s}{(\tau_f + \tau_s)^2}. \quad (3.19)$$

For  $\Delta T = 0$ , Eq. (3.10) and (3.11) become

$$G_{\perp}(\Delta t_{12}) = \frac{1}{4(\tau_s + \tau_f)} \left( e^{-|\Delta t_{12}|/\tau_s} + e^{-|\Delta t_{12}|/\tau_f} \right) \quad (3.20)$$

$$G_{\parallel}(\Delta t_{12}) = \frac{1}{4(\tau_s + \tau_f)} \left( e^{-|\Delta t_{12}|/2\tau_s} - e^{-|\Delta t_{12}|/2\tau_f} \right)^2. \quad (3.21)$$

We see that when  $\tau_f \neq \tau_s$ ,  $G_{\parallel}(\Delta t_{12})$  does not vanish even for  $\Delta T = 0$ .

### 3.2.4 Quantum Beats

The interference of two photons with slightly different frequencies will result in quantum beats. We write our mode functions as

$$\psi_f(t) = \xi_f(t) \exp[-i\omega t] \quad (3.22)$$

$$\psi_s(t) = \xi_s(t) \exp[-i(\omega + \delta)t], \quad (3.23)$$

where  $\omega$ ,  $\omega + \delta$  are the two photon angular frequencies separated by the detuning  $\delta$ . Eq. (3.10) becomes

$$G_{\parallel}(\Delta t_{12}) = \frac{1}{4} \int_{-\infty}^{\infty} \left| \xi_f(t) \xi_s(t + \Delta t_{12}) \right|^2 + \left| \xi_f(t + \Delta t_{12}) \xi_s(t) \right|^2 dt \\ - \frac{\cos(\delta \cdot \Delta t_{12})}{2} \int_{-\infty}^{\infty} \left| \xi_f(t) \xi_s(t + \Delta t_{12}) \xi_f(t + \Delta t_{12}) \xi_s(t) \right| dt, \quad (3.24)$$

and the interfering term in the coincidence probability now oscillates at the frequency difference  $\delta$  [116, 117].

### 3.3 Single Photons from the Single Atom

#### 3.3.1 Idea

For the HOM experiment, we use the single atom as a triggered single-photon source, i.e. we want to generate single photons, triggered on the detection of the heralding signal photon from the FWM source, to interfere with the FWM idler photon at the HOM interferometer.

To do so, we send a short optical  $\pi$  pulse to the atom, which excites it with near unit probability along the cycling transition  $|g\rangle = 5S_{1/2}, F=2, m_F = -2 \rightarrow |e\rangle = 5P_{3/2}, F'=3, m'_F = -3$ ; the spontaneously emitted photon is collected with the aspheric lens and sent the HOM interferometer. The excitation pulse should be much shorter than the transition lifetime of  $\tau_s = 26.2$  ns for two main reasons:

1. Due to decoherence from spontaneous decay process, only very short pulses can approach an excitation efficiency of 1.
2. If the pulse is long, the atom will start to decay and emit photons during the excitation pulse itself. This is problematic, as the coherently scattered photons (during the excitation pulse) have different temporal properties from those emitted via spontaneous decay (when the atom is no longer under the influence of probe light), and thus influence the observed HOM interference.

We only collect the emitted photons in the backward direction (opposite to the propagation direction of the probe beam) so as to separate the atomic emission from the probe pulse.

#### 3.3.2 Generating the Short Excitation Pulse

The schematic of the pulse generation setup is shown in Fig. 3.3, and a typical generated optical pulse is shown in Fig. 3.4.

##### Optical Pulse

The short optical pulse is generated from a continuous laser beam using two fiber-coupled amplitude EOMs connected in series (EOSpace, AZ-0K5-10-PFA-SFA-780-UL-S and AZ-0K5-10-PFA-PFA-780-UL). Any resonant probe light leaking through the EOMs would excite the atom and cause heating, thus dramatically reducing the lifetime of the atom in the trap, as well as contributing to additional optical noise in both collection arms. Thus it is necessary to use two amplitude EOMs in series to obtain a sufficiently large extinction ratio

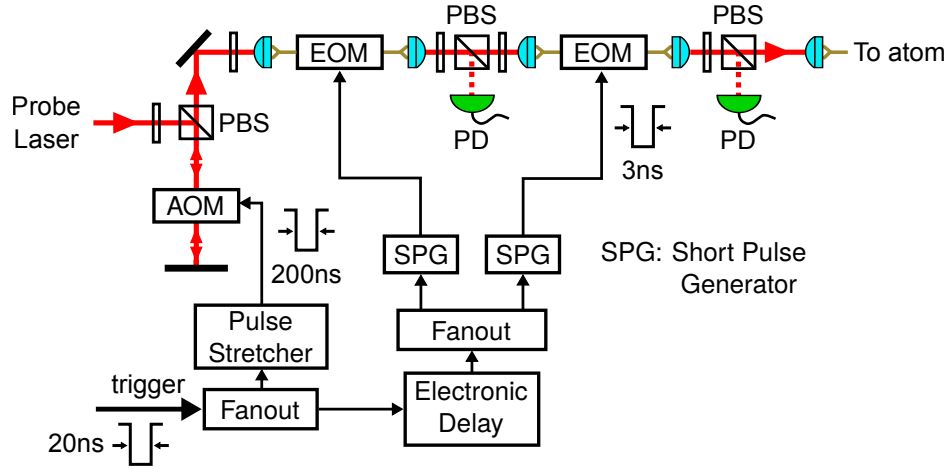


**Figure 3.3:** Schematic of the generation of the short excitation pulse. The open rectangles in the beam path are half-wave plates used to control the power splitting ratio at the PBS, and also optimize the alignment of the beam polarization to the polarization-maintaining input fibers of the EOMs. The depiction of the AOM double-pass setup has been simplified. More details are found in the main text. PBS: Polarizing beam-splitter, PD: photodiode, AOM: acousto-optic modulator, EOM: electro-optic modulator.

( $\lesssim 20$  dB per EOM), in addition to using an AOM double-pass setup as an optical switch ( $\sim 40$  dB extinction) that is only turned on briefly when the excitation pulse is generated.

Similar to the MOT cooling laser, the probe light is generated from a 780 nm laser diode (Sanyo DL-7140-201S, 80 mW) locked to the  $5S_{1/2}, F=2 \rightarrow 5P_{3/2}, F'=1$  transition, then shifted onto resonance with the cycling transition via the AOM double-pass setup.

### Electrical Signals

The generation of the excitation pulse begins with the arrival of a 20 ns NIM-logic trigger signal. A fanout unit duplicates the pulse, one copy of which turns on the AOM for 200 ns. However, there is a minimum delay of  $\approx 600$  ns between the arrival of the trigger and the beam being fully turned on, due to the propagation delay of the acoustic wave through the AOM crystal ( $\approx 500$  ns) and the rise time ( $\approx 100$  ns) of the optical response. Therefore the other copy of the trigger is delayed before it is duplicated again and sent to the short pulse generators which create the appropriate pulses for driving the EOMs. This electronic delay also allows us to fine-tune the temporal overlap between the input photons at the HOM interferometer (see §3.4.2).

For each input pulse, the short pulse generator creates a short pulse of nominal width 3 ns (see Fig. 3.5), then amplifies it to  $V_{\pi} \approx 1.7$  V (into 50  $\Omega$ ) to achieve the maximum modulation depth of the excitation pulse intensity via the EOMs.

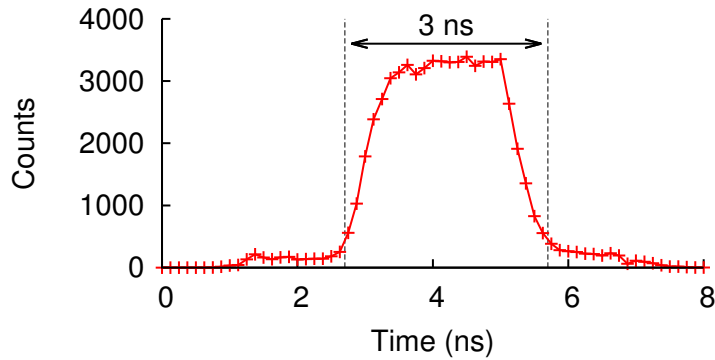


**Figure 3.4:** The 3 ns optical pulse, as measured by an APD with low jitter time (Micro Photon Devices PDM PD-050-CTC-FC). The data is recorded over many pulses, attenuated such that the number of detected photons per pulse  $\ll 1$ . The timing resolution is 125 ps, limited by the timestamp unit.

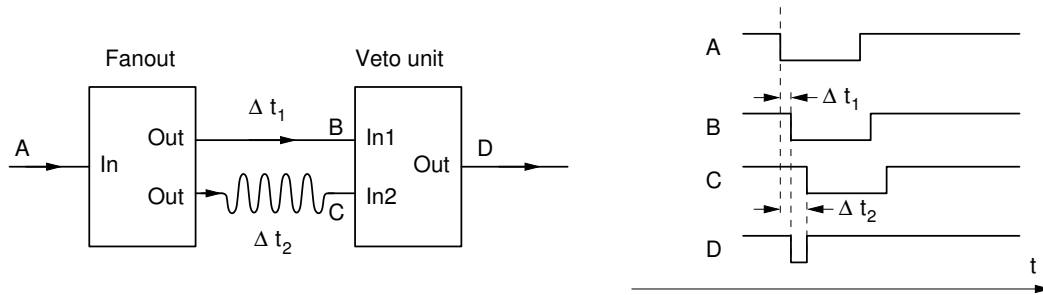


**Figure 3.5:** Working principle of the short pulse generator. Two slightly delayed copies of the input pulse is generated, and the width of the output pulse is defined by the relative delay of the leading edge of the two copies.

### Stabilizing the EOMs

The amplitude EOMs used are essentially phase modulators incorporated within a Mach-Zehnder interferometer. As with all interferometers, it is essential that the phase between the interferometer arms is kept stable. We do so by mounting each EOM within a temperature-stabilized enclosure, as shown in Fig. 3.6.

The interferometer phase can be adjusted by applying a DC bias voltage, and is set such that the transmission through the EOM is minimized when the input pulse is not applied; an input pulse of amplitude  $V_\pi$  would then set the EOM transmission to maximum. We can optimize the bias voltage by diverting some of the EOM output to a monitoring photodiode (see Fig. 3.3), scanning the bias voltage (without any input pulses), and selecting the value where the EOM transmission is minimized. Despite the temperature stabilization, we find that it is necessary to perform this optimization every hour or so.

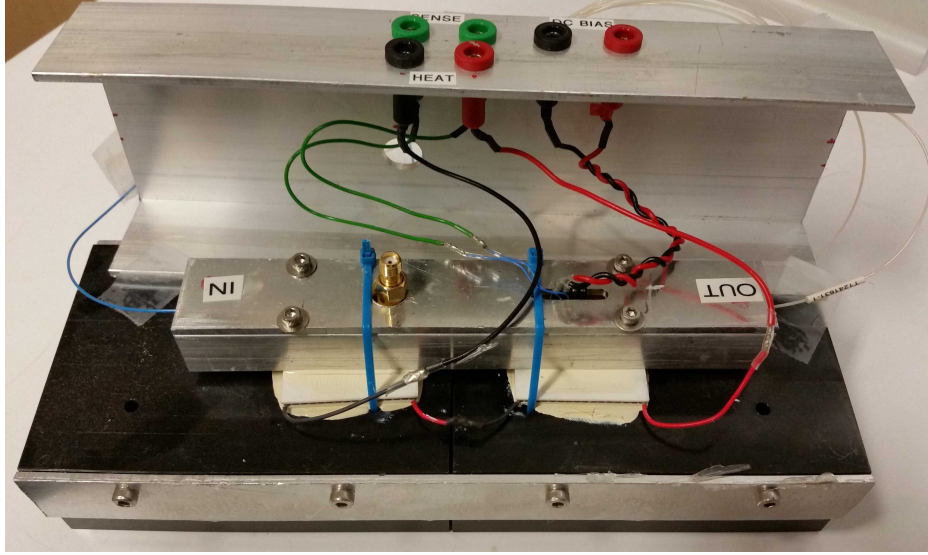


**Figure 3.6:** Photograph of the temperature-stabilized enclosure for the EOM, with the outer cover flipped open. The EOM sits within a trench in the inner aluminium block. The temperature is monitored by a thermistor, and stabilized using Peltier elements via an external PID loop.

### 3.3.3 The Single Photon from the Single Atom

The setup schematic for measuring the generated single photons is very similar to that shown in Fig. 2.1. The excitation pulses are sent to the atom via the probe beam path, and the single photons collected in the backward direction are sent directly to an APD. In the forward direction, we measure the transmitted excitation pulse and hence determine its average photon number  $\langle N \rangle$ ; a neutral density filter (optical density (OD) 3.7) is placed in the forward collection path so that we detect  $\ll 1$  photons per pulse<sup>3</sup>. We then obtain  $\langle N \rangle$  by accounting for the collection and detection efficiencies.

The experimental sequence for the pulsed excitation of the single atom is shown in Fig. 3.7. The steps are as follows:

1. Turn on the MOT, and wait for an atom to be loaded into the dipole trap.
2. Turn off the MOT quadrupole field, and perform molasses cooling for 10 ms.
3. Turn off the MOT beams, and perform 10 ms of optical pumping to the  $|g\rangle = 5S_{1/2}, F=2, m_F = -2$  dark state. Both the pumping and repump light are sent to the atom via the probe beam path. A bias magnetic field of  $\approx 2$  Gauss is turned on.

<sup>3</sup> This is to avoid saturating the APD: due to its dead time, if there were multiple photons in one pulse, the APD would only be able to detect one.

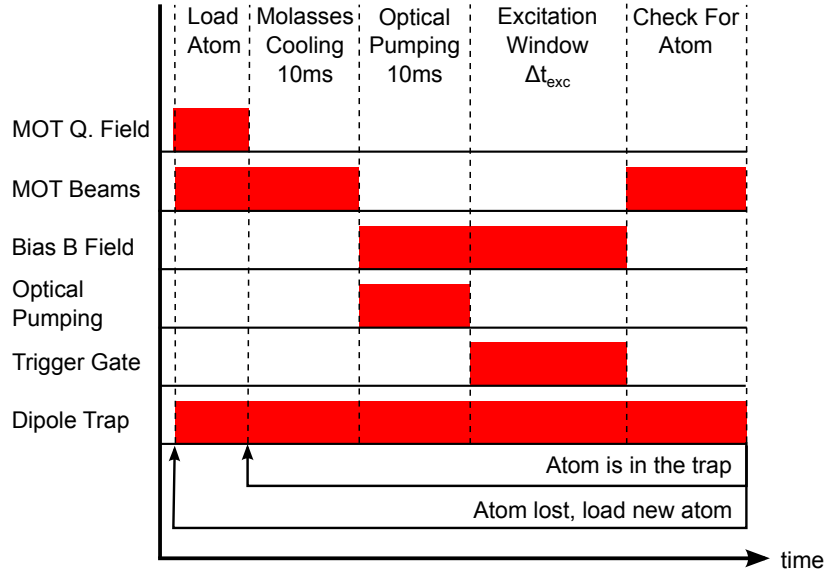


**Figure 3.7:** Experimental sequence for the pulsed excitation of the single atom. When the trigger gate is opened during the excitation window (of width  $\Delta t_{\text{exc}}$ ), an incoming trigger signal generates an excitation pulse.

4. Excitation window of duration  $\Delta t_{\text{exc}}$ , which ranges from 0.25 s to 1.5 s in our measurements. The trigger gate is opened, and an incoming trigger signal generates an excitation pulse.
5. Check for the presence of the atom. The bias magnetic field is turned off, and the MOT beams (but not the quadrupole field) is turned on.
  - If the atom is present, the data collected in this sequence is considered valid. Repeat sequence from step 2.
  - If the atom is lost, the data collected in this sequence is discarded. Return to step 1 and load a new atom.

We check for the presence of the atom by measuring fluorescence in the backward direction; we do not detect sufficient fluorescence in the forward direction due to the attenuation by the neutral density filter.

For this measurement, we send 100 triggers at intervals of  $8 \mu\text{s}$  to the setup during each excitation window. Typical results are shown in Fig. 3.8.

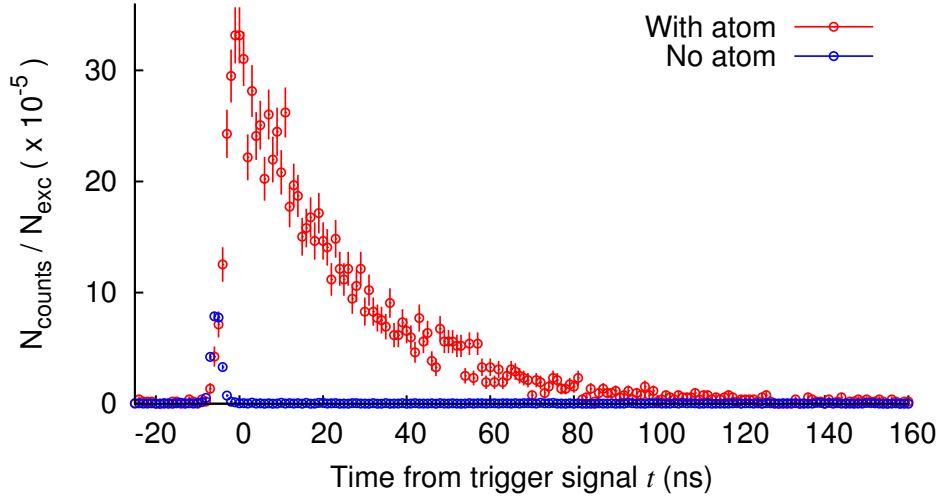


**Figure 3.8:** Spontaneous emission from the single atom, measured in the backward direction, for  $\langle N \rangle = 700$  photons. The recorded APD counts are normalised to the total number of excitation pulses sent to the atom. Without the atom in the trap, we observe that a portion of the excitation pulse is back-reflected into the collection mode by various components in the optical path, but this should not affect the experiment significantly. The time-bin size is 1 ns, and the error bars reflect Poissonian statistics. The detection times are offset to account for delays introduced by optical and electrical delay lines.

### Indeed a Single Photon?

We had previously mentioned that the heralded idler photon from the FWM source is a very good approximation of a single photon state (see §2.2.3). To verify that this is also the case for the single atom source, we again excite the single atom at regular intervals, but send the photons collected in the backward direction to a 50:50 beam-splitter, before measuring the coincidences between the APD detection events at the outputs. If we are indeed generating single photons, both detectors will not detect a photon simultaneously, and there will be no coincidences at zero time delay between the detection events.

The coincidence measurement is shown in Fig. 3.9, with the diminished peak at zero detection delay bearing the signature of single photons.

### 3.3.4 Optimizing the Pulse Parameters

For a two-level system, the evolution of its excited state population  $P_e$  under resonant excitation can be described by Rabi oscillations with a characteristic Rabi frequency  $\Omega$ . For a very short excitation pulse of width  $\Delta t_{\text{pulse}} \ll \tau_s$ , where  $\Delta t_{\text{pulse}} = 3$  ns and  $\tau_s$  is the excited state lifetime, we can ignore the effects of spontaneous decay during the excitation. We

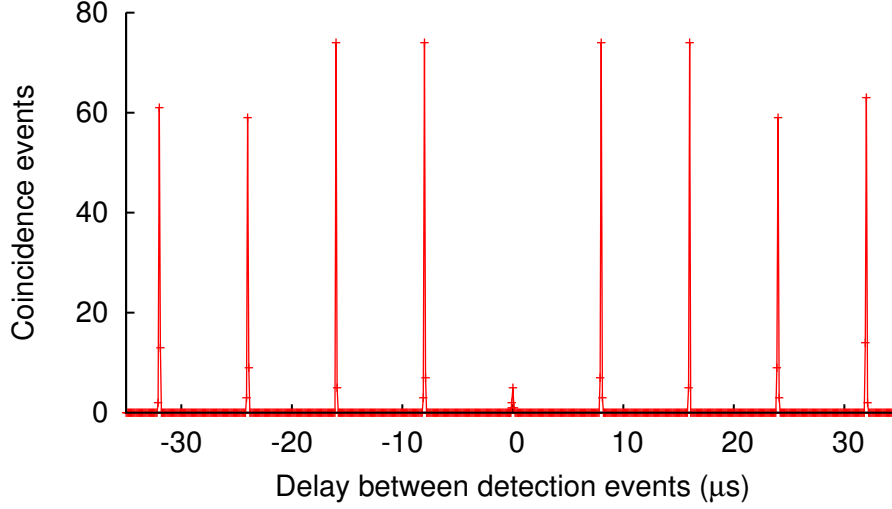


**Figure 3.9:** Coincidence measurement between two APDs at the outputs of a 50:50 beam-splitter, with the single photons generated by the single atom via triggered excitation as the input. We observe regular peaks  $8 \mu\text{s}$  apart, corresponding to the interval between excitation pulses sent to the atom. The lack of coincidence events at zero time delay is the signature of single photons; the residual of coincidence events there ( $\sim 10\%$  of the average of the other peaks) is consistent with the expected number of accidental coincidences contributed by background noise in the measurement.

are interested in the excitation probability, i.e. the excited state population right after the excitation pulse ends, given by [39]

$$P_e = \sin^2\left(\frac{\Omega \cdot \Delta t_{\text{pulse}}}{2}\right). \quad (3.25)$$

We can achieve the maximum excitation, i.e.  $P_e = 1$ , with a so-called  $\pi$  pulse which satisfies  $\Omega \cdot \Delta t_{\text{pulse}} = \pi$ . The Rabi frequency is proportional to the electric field strength, thus for a given  $\Delta t_{\text{pulse}}$ ,  $\Omega \propto \sqrt{\langle N \rangle}$ , where  $\langle N \rangle$  is the average photon number per pulse.

From the measurement of the atomic emission (see Fig. 3.8), we can obtain  $P_e$  via

$$P_e = \frac{1}{\eta N_t} \sum_{i=0}^j N_{\text{counts}}(t_i), \quad (3.26)$$

where  $N_{\text{counts}}(t_i)$  is the number of APD counts in time-bin  $t_i$ ,  $N_t$  is the total number of triggered excitation pulses, and  $\eta \approx 0.013$  is the overall collection and detection efficiency for this particular configuration. The summation is performed from  $t_0$  to  $t_j = t_0 + 155 \text{ ns}$ , where  $t_0$  corresponds to the peak of the detected photon distribution, and marks the start of

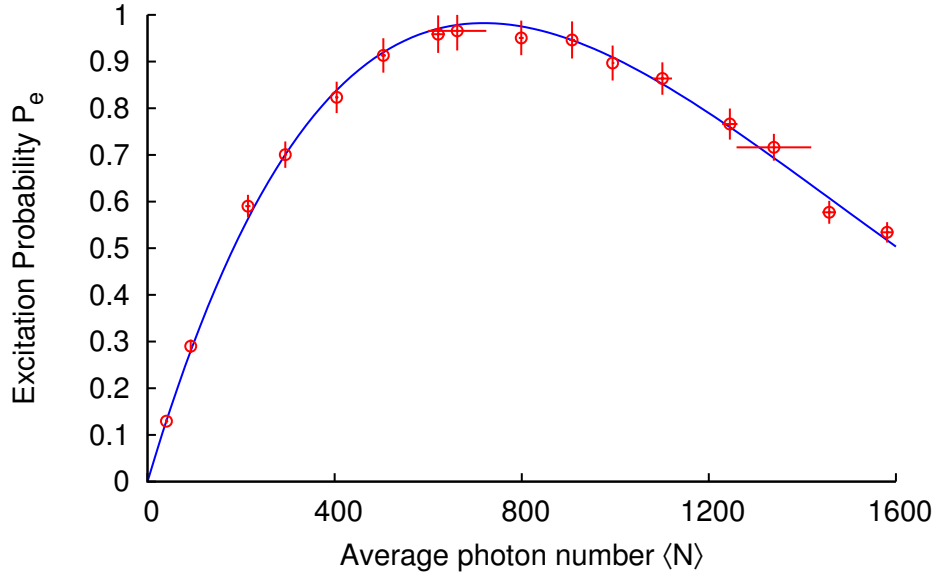


**Figure 3.10:** Rabi oscillations in the excitation probability  $P_e$  as we vary the average pulse photon number  $\langle N \rangle$ . The solid line shows a fit to the form  $P_e = A \sin^2(B\sqrt{\langle N \rangle})$ , where  $A$  and  $B$  are free parameters. Vertical error bars represent Poissonian statistics, while horizontal bars represent the drifts in  $\langle N \rangle$  during the measurement.

the spontaneous decay regime (we also see that is the point where the excitation pulse ends). We limit  $t_j$  as the noise is more dominant than the signal for  $t_i > t_j$ . With this summation window, we include  $\frac{1}{\tau_s} \int_{t_0}^{t_j} e^{-t/\tau_s} dt = 0.997$  of the photon.

We observe Rabi oscillations as we vary  $\langle N \rangle$ , as shown in Fig. 3.10. The results fit well to our predictions, and we obtain a  $\pi$  pulse for  $\langle N \rangle = 700$  photons and a maximum  $P_e = 96.5 \pm 1.5\%$ .

### Even Shorter Pulses?

As mentioned earlier, we want  $\Delta t_{\text{pulse}}$  to be as short as possible, and we can indeed generate even shorter pulses with our short pulse generator, and still achieve a  $\pi$  pulse with a larger  $\langle N \rangle$ . However, there are practical limitations concerning the probe laser power.

Despite only requiring  $\langle N \rangle \sim 10^3$ , there are major losses in the probe optical path, e.g. the 99:1 beam-splitter (99% loss) used to separate the probe beam and collection mode, the 6:1 beam-splitter (83%) used to combine multiple beams into the probe beam path, EOMs (>50% each), AOM double-pass ( $\sim 50\%$ ) etc. In Fig. 3.10,  $\langle N \rangle \approx 1600$  already corresponds to the maximum obtainable pulse intensity from the low-power laser diode. Therefore, we keep the

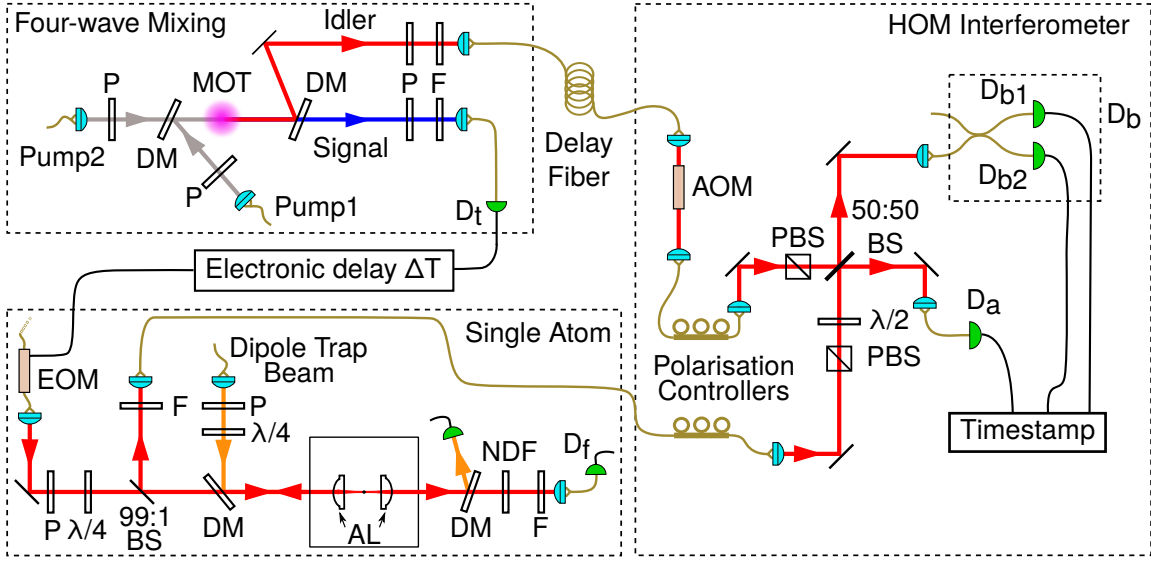


**Figure 3.11:** Schematic of the full HOM experimental setup, consisting of the FWM setup (top left), single atom setup (bottom left), and the HOM interferometer (right). One output port of the HOM 50:50 beam-splitter is connected to another 50:50 fiber beam-splitter, with detectors  $D_{b1}$  and  $D_{b2}$  at the outputs; these two detectors are collectively referred to as  $D_b$ . AOM, EOM: acousto- and electro-optic modulators, DM: dichroic mirrors, P: polarizers, F: interference filters, NDF: neutral density filter,  $\lambda/2$ ,  $\lambda/4$ : half- and quarter-wave plates, (P)BS: (polarizing) beam splitters,  $D_a$ ,  $D_{b1}$ ,  $D_{b2}$ ,  $D_f$ ,  $D_t$ : avalanche photodetectors.

pulse width at  $\Delta t_{\text{pulse}} = 3$  ns as a practical choice, which leaves us with a comfortable buffer to maintain  $\langle N \rangle$  even if certain elements of the setup deteriorate.

## 3.4 HOM Experimental Setup

Fig. 3.11 shows the joint experimental setup for the HOM interference experiment.

### 3.4.1 Single Atom and FWM Setups

The details of the single atom and FWM setups have already been covered in Chapter 2. The detection of a signal photon heralds the presence of a photon in the idler mode, and is also used to trigger the generation of the excitation pulse at the single atom setup. The electronic delay  $\Delta T$  (implemented via 2 x ORTEC DB463 Delay Box units) sets the delay between the detection of the heralding photon and the generation of the excitation pulse; controlling  $\Delta T$  allows us to synchronize both setups and adjust the temporal overlap between the photons.

To allow for sufficient time to generate the excitation pulse, the idler photon travels through a 230 m long single-mode fiber to delay its arrival at the HOM interferometer.

At the single atom setup, the forward collection arm is connected to APD  $D_f$ , which is used to measure atomic fluorescence and check for the presence of the trapped atom. The backward collection arm is connected directly to the HOM interferometer via a single-mode fiber.

### **Back-reflection Problem**

Unlike the previous pulsed excitation configuration (§3.3.3), where we relied on the backward collection arm to check for the presence of the atom, here we can only use the forward APD  $D_f$  for that purpose. As such, we planned to calibrate the pulse parameters beforehand, then remove the neutral density filter (NDF) of optical density (OD) 3.7 in the forward collection path when performing the experiment, such that we can still detect and trigger on the atomic fluorescence using  $D_f$ .

However, once the NDF is removed, the back-reflection of the excitation pulse into the backward collection mode becomes more severe (see Fig. 3.12a, blue curve). Besides a significant noise floor, there is a large peak caused by the back-reflection of the excitation pulse by the far end of the single-mode collection fiber in the forward direction (the fiber end facing the APD). Despite the collection fiber having APC connectors on both ends, the small amount of back-reflection from the far end of the fiber is large compared to the single-photon signal we hope to collect from the single atom.

We cannot ignore this issue as the large back-reflection peak occurs where the single photon emission is still significant; even if we exclude the time window corresponding to the peak during our data processing, we will lose a significant fraction of the recorded data and also effectively alter the temporal shape of the photon.

To mitigate the problem, we insert a NDF of OD 0.16 in the forward collection path: the attenuation is strong enough to suppress the noise floor, but still allows us to detect a sufficiently high level of fluorescence at  $D_f$  to determine the presence of the atom. We also changed the length of the collection fiber in the forward direction from 5 m to 9 m, delaying the back-reflection peaks to  $t > 87$  ns after the peak of the photon profile (see Fig. 3.12b). We can now exclude the time windows corresponding to the back-reflection peaks without losing too much of the single photon signal.

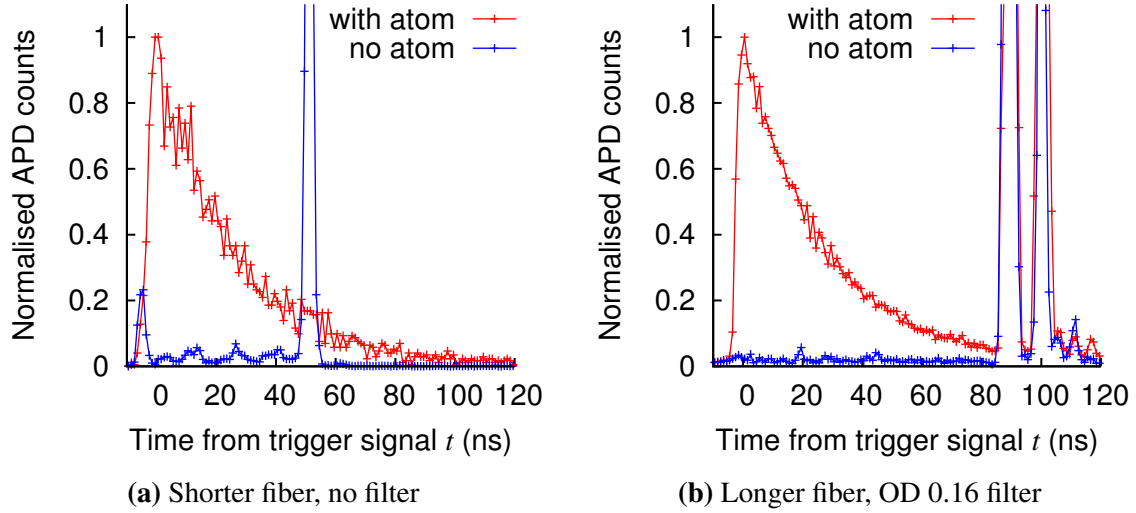


**Figure 3.12:** APD measurements at the backward collection arm for the pulsed excitation of the single atom. **(a):** As a reference, we include the red curve, taken from Fig. 3.8, which is measured with the atom and with a OD 3.7 filter in the forward collection arm. The blue curve is measured without the filter. There is a 5 m fiber between the collection lens and APD  $D_f$ . **(b):** Both curves are measured with a OD 0.16 filter in the forward collection arm, and a longer 9 m fiber. Compared to (a), the noise floor is suppressed, and the strong back-reflection peaks<sup>4</sup> are delayed to  $t > 87$  ns. The small initial peak (blue curve in (a)) is also eliminated by slightly tilting the optical components that reflected a significant amount of light. In both figures, the time-bin width is 1 ns, and the APD counts are normalised to the peak of the curve taken with the trapped atom. The detection times are offset to account for delays introduced by optical and electrical delay lines.

### 3.4.2 HOM Interferometer

The HOM interferometer is located on the same optical table as the single atom setup (while the FWM setup is  $\sim 15$  m away, in an adjacent room). The centerpiece of the HOM interferometer is a 50:50 cube beam-splitter (Melles Griot NCBS-780-050) where the single photons from both the FWM source and the single atom interfere. One of the beam-splitter outputs is sent directly to APD  $D_a$ , while the other output is connected to a 50:50 fiber beam-splitter (Thorlabs FC780-50B-APC). The outputs of the fiber beam-splitter are connected to APDs  $D_{b1}$  and  $D_{b2}$ ; these two APDs are collectively referred to as  $D_b$ . The purpose of this arrangement is to detect the outcomes where two photons exit together from one of the outputs of the central beam-splitter, which will become relevant in §3.6.4.

<sup>4</sup>We now obtain an extra back-reflection peak. The time delay after the first one suggests that it is due to a back-reflection from the APD diode of the home-made APD unit, with a 10 ns round trip time along the 1 m pigtailed fiber. It is not clear why this extra peak did not show up before.

For maximum interference effect, we have to minimize the distinguishability of the two interfering photons in terms of frequency, polarization, spatial mode, and temporal overlap.

### **Polarization**

For each input arm, a PBS sets the polarization of the input photons to be horizontal, while fiber polarization controllers maximize the transmission through the PBS. An additional HWP allows us to set the relative polarization of the input photons to be either parallel (interfering) or orthogonal (non-interfering).

We note the passive polarization stability of the 230 m delay fiber; the transmission of the idler photons through the PBS does not drift by more than a few percent over several days.

### **Frequency**

The central frequency of the idler photon generated via FWM is that of the unperturbed  $5S_{1/2}, F=2 \rightarrow 5P_{3/2}, F'=3$  transition, but the corresponding energy levels of the trapped single atom are shifted due to AC Stark shifts from the dipole trap and Zeeman shifts from the bias magnetic field (see Appendix A). By observing the extinction of a coherent probe beam by the single atom as a function of the probe frequency (the methods are similar to those presented in §4.5.4), we measure a blue-shift of  $\delta/2\pi = 76 \pm 1$  MHz in the transition resonance frequency. To compensate for this, we use an AOM to shift the central frequency of the idler photon onto resonance with the single atom cycling transition.

### **Spatial Mode**

Spatial mode-matching is achieved by careful alignment of the interferometer. To verify this, we replace the inputs with a frequency-locked laser split by a fiber beam-splitter, with one arm going through a short free-space coupling link (see Fig. 3.13a). We ensure that the optical power in each arm of the HOM interferometer is equal. The passive instability of the free-space link causes a sufficiently large drift in the relative phase of the HOM interferometer input arms, and we are able to observe interference fringes (see Fig. 3.13b). The measured visibility is  $>98\%$ , indicating good spatial mode-matching.

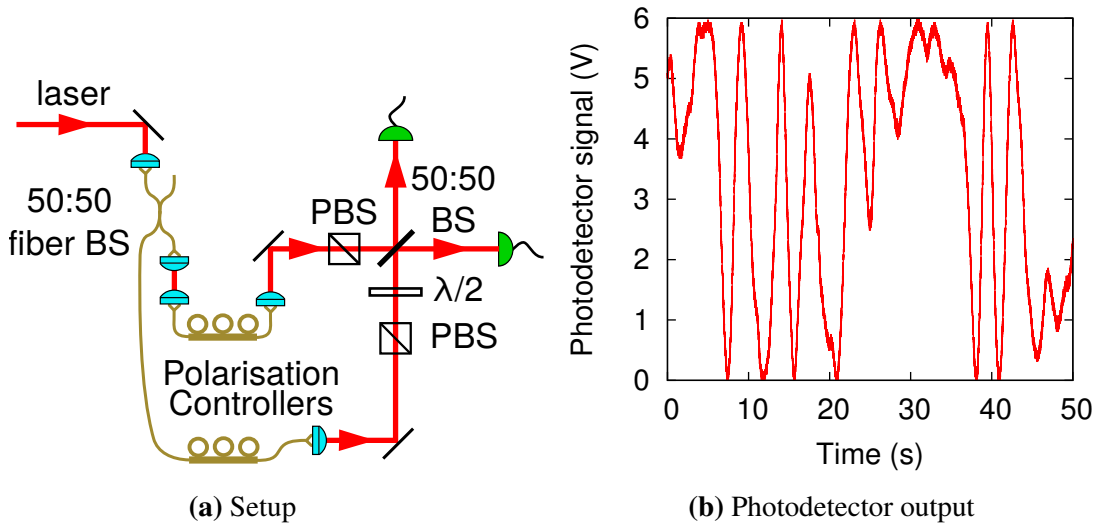


**Figure 3.13:** Verifying the spatial mode-matching of the HOM interferometer. **(a)** The interferometer inputs are replaced with a frequency-locked laser split by a fiber beam-splitter, with one arm going through a short free-space coupling link. **(b)** Photodetector signal at one of the HOM interferometer outputs showing interference fringes under the passive instability of the free-space link.

### Temporal Overlap

For interference to take place, we have to ensure that the photons from both the FWM and single atom setups arrive<sup>5</sup> at the beam-splitter in the HOM interferometer simultaneously. To determine the temporal overlap, we record the APD counts at  $D_a$  while blocking each of the inputs in turn, such that we independently measure the temporal profiles of the two photons.

The relative delay between the trigger signal arriving at the single atom setup and idler photon arriving at the interferometer is 850 ns, which is fixed over the course the experiment. Again using  $t_s$  and  $t_f$  to refer to the peak of the temporal profiles for the single photons from the single atom and FWM sources, from Eq. (3.18) we see that the maximum overlap occurs when the peaks of their temporal profiles coincide, i.e.  $t_f = t_s$ . We define  $\Delta T = 0$  as the electronic delay applied to achieve this synchronization, as shown in Fig. 3.14.

<sup>5</sup> For convenience, we use the term ‘arrival time of the photon’ loosely to refer to the time corresponding to the peak of its temporal profile. Of course, the photon detection times are not constant (with respect to the heralding signal), but has a distribution given by the temporal profile of the photon.

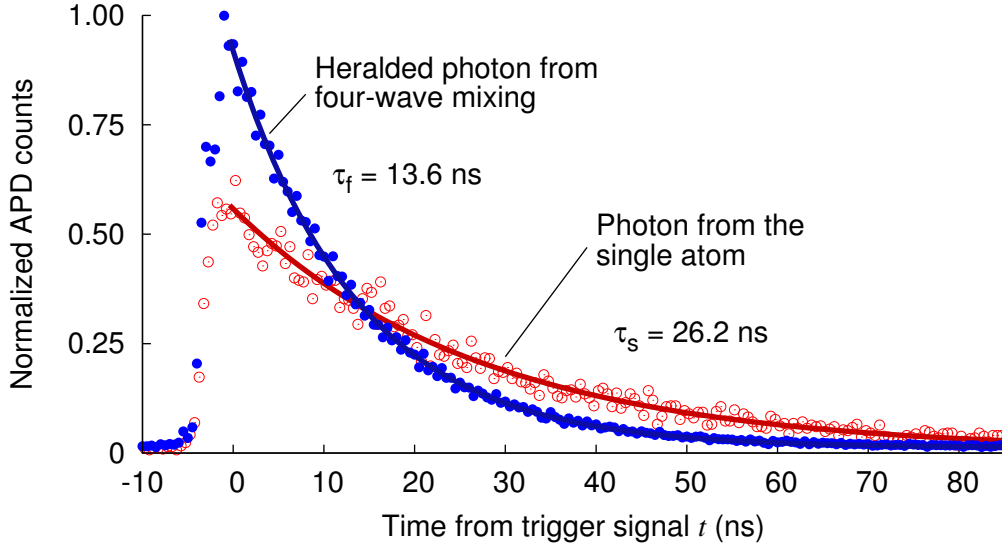


**Figure 3.14:** Temporal profile of the single photons generated by the single atom (open circles) and FWM (filled circles) sources. The coherence times are obtained from exponential fits (solid lines). The APD counts are sorted into 500 ps wide time-bins, and normalized such that the area under both curves are equal. The detection times are offset to account for delays introduced by optical and electrical delay lines.

### 3.4.3 Rates and Efficiencies

For the single atom photon source, we define the overall generation, collection and detection efficiency as  $\eta_{sa} = N_{det}/N_t$ , where  $N_{det}$  is the number of detected photons at the HOM interferometer outputs ( $D_a$ ,  $D_{b1}$ , and  $D_{b2}$  combined), and  $N_t$  is the detected number of heralding photons, corresponding to the number of triggered excitation pulses sent to the single atom. This is measured while blocking the interferometer input for the FWM photon.

We measure  $\eta_{sa} \approx 0.5\%$ . The approximate breakdown is as follows: excitation efficiency (95%), collection efficiency at the single atom setup (1.5%), fiber coupling of the HOM interferometer output (75%), and the APD efficiency (50%).

For the FWM source, the efficiency and rates depend on the operating parameters and the desired idler photon decay time  $\tau_f$ . For much of the experiment, we focus on  $\tau_f \approx 13.5$  ns, for which we achieve an overall heralding rate<sup>6</sup> of  $500 - 700 \text{ s}^{-1}$  and a pair rate of  $1.5 - 2 \text{ s}^{-1}$ . To obtain shorter decay times, we increase the optical density of the atomic ensemble, which would also raise the photon rates. While a larger photon rate is generally desirable, here we additionally tune the pump powers to keep the detection rate of heralding photons constant,

<sup>6</sup> The FWM setup alternates between  $80 \mu\text{s}$  of MOT cooling and  $10 \mu\text{s}$  of photon pair generation, thus the ‘instantaneous’ rate during the pair generation window itself is a factor of 9 higher.

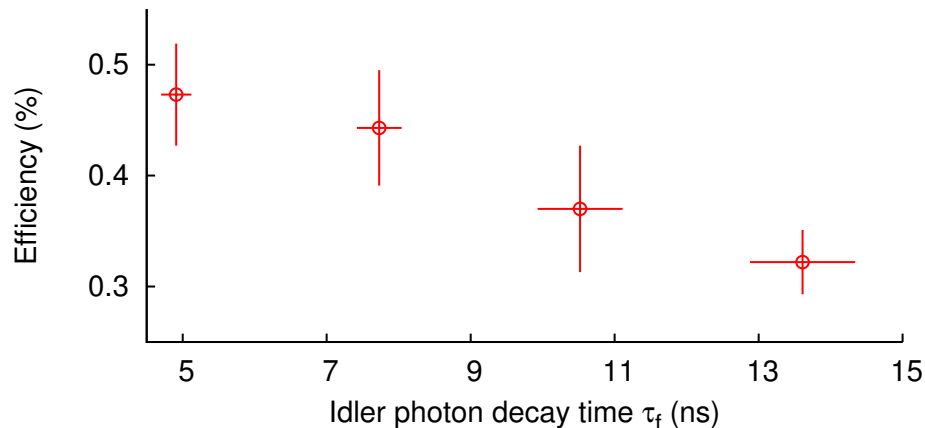


**Figure 3.15:** Heralding efficiency of the FWM source  $\eta_{\text{fwm}}$  at different idler decay times  $\tau_f$  during the HOM experiment. Error bars reflect the standard deviation in the distribution of the measured values.

as changing the number of triggered excitation pulses per experimental sequence would also influence the atom lifetime in the trap (see §3.5.1).

We similarly define the heralding efficiency  $\eta_{\text{fwm}} = N_{\text{pairs}}/N_t$ , where  $N_{\text{pairs}}$  is the number of coincident detections of the signal (herald) and idler photons, i.e. the detected number of photon pairs. This is measured during the experiment when the atom is lost from the trap (see §3.5.3), and the results after correcting for accidentals are shown in Fig. 3.15.

The major sources of losses for the idler photon are (approximately): the 230 m delay fiber (40%)<sup>7</sup>, single-pass AOM and re-coupling into the fiber (40%), fiber coupling at the HOM interferometer output (25%), and APD efficiency (50%).

## 3.5 Running the Experiment

### 3.5.1 Choosing the Length of the Excitation Window

As mentioned in §2.1.3, we want to choose the length of the experimental sequence such that we have an optimal balance between the duty cycle and the collection rate of valid data. We run the pulsed excitation sequence (see §3.3.3) while varying the length of the excitation window  $\Delta t_{\text{exc}}$ . To simulate actual experimental conditions, we keep the FWM source running

<sup>7</sup> To obtain a 230 m fiber, we spliced together one 30 m and two 100 m fibers, and the limited quality of the splices limits the overall transmission to 60%. For comparison, the transmission of a single 230 m length of single-mode fiber (Thorlabs 780HP) would be 83%, according to the datasheet.

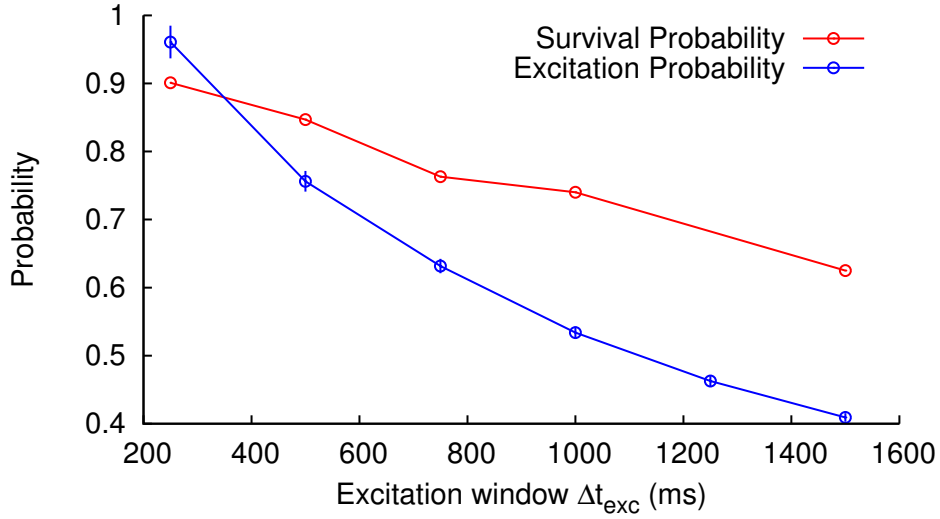


**Figure 3.16:** The measured survival and excitation probabilities as a function of the excitation window  $\Delta t_{\text{exc}}$ .

and use the detection of heralding photons as the trigger signals, even though we do not use the FWM idler photons here.

In particular, we are interested in the survival probability of the atom in the trap after each experimental sequence, as well as its excitation probability. The survival probability is the fraction of the number of experimental sequences that end up with an atom still present in the trap, while the excitation probability is obtained in the same way as in §3.3.4.

The results are shown in Fig. 3.16. For longer  $\Delta t_{\text{exc}}$ , the survival probability decreases due to a combination of the natural collisional loss mechanism and the atom being heated up by more excitation pulses. The overall excitation probability also drops as each excitation pulse has a finite probability of transferring the atom out of the cycling transition and into the  $F = 1$  ground state, most likely due to the excitation pulse not having a completely pure  $\sigma^-$  polarization. Besides, the prepared state would also have a finite coherence time even in the absence of excitation pulses (e.g. due to residual magnetic fields inducing Larmor precession, etc.).

Given these results, we choose to have five measurement cycles of 100 ms each, with 10 ms of optical pumping before each cycle to ensure that the atom stays in the ground state of the cycling transition.

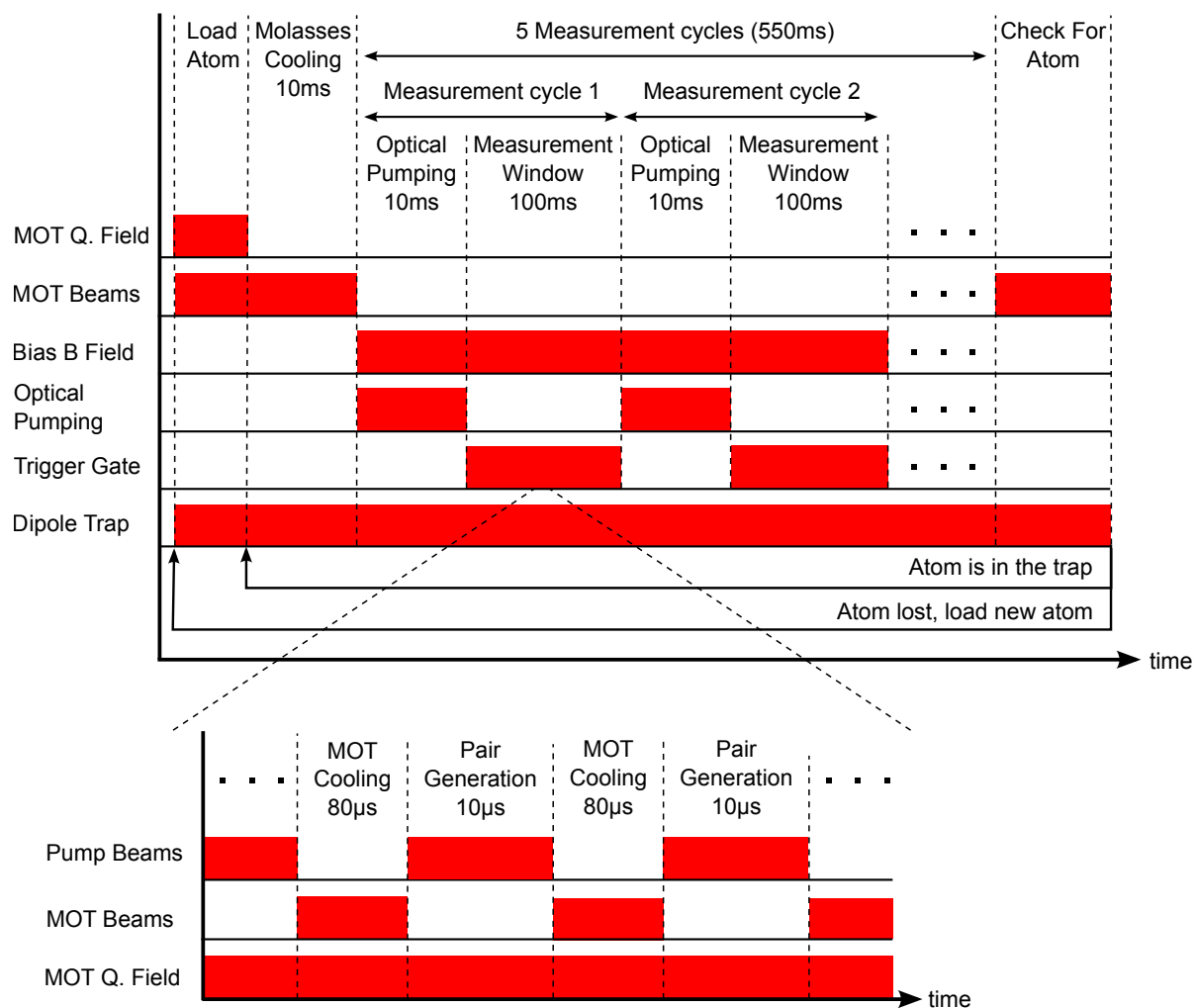


**Figure 3.17:** Experimental sequence of the HOM interference experiment for the single atom setup (top) and the FWM setup (bottom). The two sequences run asynchronously. When the trigger gate is opened during the 100 ms measurement window, an incoming trigger signal generates an excitation pulse.

### 3.5.2 Experimental Sequence

The full experimental sequence is shown in Fig. 3.17.

#### Single Atom Setup

For the single atom setup, the steps are:

1. Turn on the MOT, and wait for an atom to be loaded into the dipole trap.
2. Turn off the MOT quadrupole field, and perform molasses cooling for 10 ms.
3. Execute five measurement cycles, each consisting of:
  - (a) 10 ms of optical pumping to the  $|g\rangle = 5S_{1/2}, F=2, m_F = -2$  dark state. Both the pumping and repump light are sent to the atom via the probe beam path. The periodic optical pumping ensures that the atom stays in the ground state of the cycling transition throughout the whole sequence. At the start of the first cycle, a bias magnetic field of  $\approx 2$  Gauss is turned on.
  - (b) 100 ms measurement window. The trigger gate is opened, and an incoming trigger signal generates an excitation pulse.
4. Check for the presence of the atom by monitoring atomic fluorescence at APD  $D_f$ . The bias magnetic field is turned off, and the MOT beams (but not the quadrupole field) is turned on.
  - If the atom is present, the data collected in this sequence is considered valid. Repeat sequence from step 2.
  - If the atom is lost, the data collected in this sequence is discarded. Return to step 1 and load a new atom.

On the single atom setup, incoming trigger signals are recorded only during the measurement windows. APD clicks are recorded only if they occur within a  $2\ \mu\text{s}$  window starting from the arrival of a trigger signal. This avoids the recorded data files from being unnecessarily large due to APD clicks from MOT fluorescence, background light etc.

#### FWM Setup

The FWM setup alternates between  $80\ \mu\text{s}$  of MOT cooling and  $10\ \mu\text{s}$  of photon pair generation. During photon pair generation, the detection of a heralding photon generates a trigger

signal which is sent to the single atom setup. The FWM sequence runs continuously and is not synchronized with the single atom setup.

### 3.5.3 Monitoring the Photon Decay Times

The decay time of the spontaneously emitted photon from the single atom  $\tau_s$  is fixed by the natural lifetime of the transition. However, the decay time of the heralded idler photon  $\tau_f$  depends on various parameters which can drift over time. Thus we need to monitor  $\tau_f$ , and maintain it at the desired value by making slight adjustments to the optical density (OD) of the atom cloud.

When the atom is lost from the trap and before the next atom is loaded (step 1 of the single atom sequence), the only light reaching the interferometer from the single atom setup is that of MOT fluorescence, which is uncorrelated with the FWM photons. Thus, with the triggers from  $D_t$  serving as the heralding signal, the coincidence histogram between  $D_t$  and  $D_a$  will yield the exponentially decaying profile of the idler photon (as in Fig. 2.8), and we can extract the decay time  $\tau_f$  from a fit. We perform the fit on the data accumulated over every 30 mins while running the experimental sequence, and adjust the quadrupole coil current (and hence the OD of the cloud) at the FWM setup to keep  $\tau_f$  constant.

From the detected number of triggers and coincidence events, we can also monitor the rates and efficiencies of the FWM source directly.

## 3.6 Results

In this section we present the results of the HOM interference experiment [117, 118].

First, we present the results that show the maximum interference by using synchronized photons ( $\Delta T = 0$ ). We then study the HOM effect further by introducing controlled degrees of distinguishability between the photons. Varying  $\Delta T$  produces the familiar HOM dip, detuning the central frequency of the idler photon leads to quantum beats, while controlling the idler decay time  $\tau_f$  can also vary the temporal overlap between the photons.

### Preamble on Data Analysis

To observe the HOM interference, we consider the coincidences between the detectors at the outputs of the HOM interferometer. The arrival time of the FWM idler photon is always fixed with respect to the trigger signal; by varying  $\Delta T$ , we can control the arrival time of the photon from the single atom with respect to the idler photon.

The detection times of all detectors are offset to account for the delays introduced by optical and electrical delay lines. We refer to the earlier of the two arrival times  $t_s$  and  $t_f$  as the start of the qualifying window  $t_q$ <sup>8</sup>. If either  $D_a$  or  $D_b$  clicks within 85 ns starting from  $t_q$ , that click is considered ‘qualified’; with that qualified click as a reference, we then look for coincident clicks in the other detector. The coincidence events are sorted into time bins according to the time delay between the detection events  $\Delta t_{ab}$ .

In searching for coincidence events, we exclude the time windows corresponding to the back-reflection peaks caused by the collection fiber in the single atom setup (see §3.4.1). These peaks, starting from  $t_s + 87$  ns, also set a natural limit of 85 ns for the width of the qualifying window.

### 3.6.1 Synchronized Photons: $\Delta T = 0$

First, we present the measurements performed with synchronized photons, i.e.  $\Delta T = 0$ , for photons with the measured decay times  $\tau_f = 13.61 \pm 0.73$  ns (the uncertainty represents the standard deviation of the measured values, see Fig. 3.15) and  $\tau_s = 26.18 \pm 0.11$  ns (obtained from an exponential fit to the measured temporal profile shown in Fig. 3.14).

We consider the normalized coincidence probability

$$G(\Delta t_{ab}) = \frac{N_{ab|t}(\Delta t_{ab})}{N_t}, \quad (3.27)$$

where  $N_{ab|t}(\Delta t_{ab})$  is the number of coincidence events between  $D_a$  and  $D_b$ , and  $N_t$  is the number of triggers.

The measured  $G_{\perp}$  and  $G_{\parallel}$  are shown in Fig. 3.18. For  $|\Delta t_{ab}| \lesssim 50$  ns, the coincidence probability for non-interfering photons  $G_{\perp}$  increases significantly above the background at large  $|\Delta t_{ab}|$ , while it remains at an almost constant level for the interfering case  $G_{\parallel}$ . The lack of coincidences in  $G_{\parallel}$  compared to  $G_{\perp}$  demonstrates the HOM interference. The constant offset in the coincidence measurements are due to accidental coincidences, which result from the limited efficiencies of the single photon sources.

<sup>8</sup> In practice, we shift  $t_q$  back by a few ns so as to include the rising edge of the detected temporal profile, which is not infinitely sharp. For the FWM photon, we expect that the rising edge is due to the timing jitter of the APDs (both  $D_t$  and the APD at the interferometer output), i.e. the rising edge is still ‘part of the photon’. For the single atom, however, we ideally only want to consider the spontaneous emission regime, and exclude any photons collected during the excitation pulse; yet for  $t_s > t_f$  it is impossible to exclude the rising part as it already overlaps with temporal profile of the FWM photon. Therefore, for overall consistency, we always include the rising edge of the earlier photon, regardless of which photon arrives earlier.

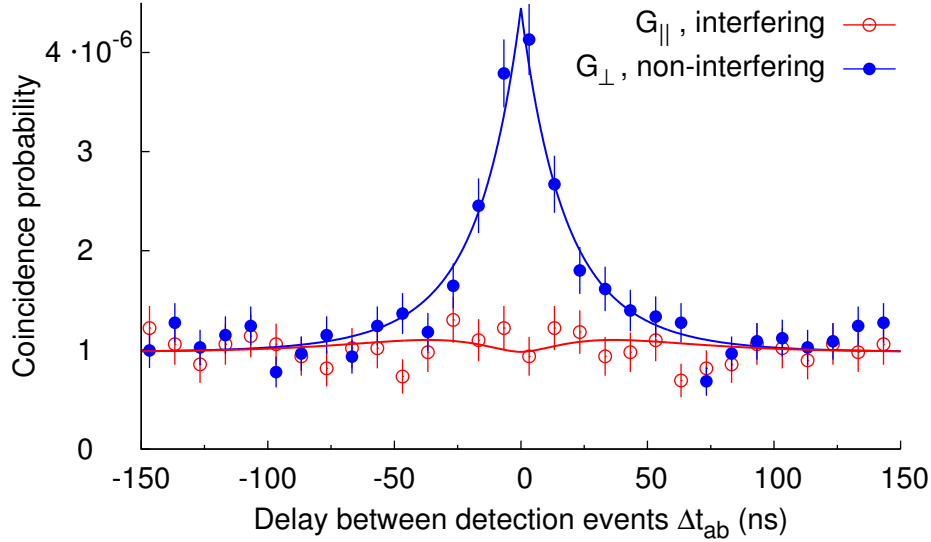


**Figure 3.18:** Coincidence probability between  $D_a$  and  $D_b$  measured at  $\Delta T = 0$ . The filled and open circles represent the cases where the photons have orthogonal (non-interfering) and parallel (interfering) polarizations, respectively. The data is sorted into 10 ns wide time-bins and normalized to the total number of trigger events  $N_f$ . The solid lines represent  $G_{\text{acc}} + A \cdot G(\Delta t_{ab})$  [see Eq. (3.20), (3.21)], where  $G_{\text{acc}}$  is a constant offset describing the accidental coincidences, and  $A$  is a scaling factor. Error bars represent Poissonian statistics.

The interference visibility  $V$  is then a measure of the contrast between  $G_{\perp}$  and  $G_{\parallel}$ . From Eq. (3.19), we expect  $V = \frac{4\tau_f\tau_s}{(\tau_f+\tau_s)^2} = 90.0 \pm 1.5\%$ . We obtain  $V$  from our data via

$$\begin{aligned} V &= 1 - P_{\parallel}/P_{\perp} \\ &= 1 - \frac{\sum_{T_c} G_{\parallel}(\Delta t_{ab})}{\sum_{T_c} G_{\perp}(\Delta t_{ab})} \end{aligned} \quad (3.28)$$

where the summation is performed over the coincidence window  $T_c$ .

The accidental coincidences degrade the observed visibility. To reduce the influence of the accidentals, we can limit ourselves to a narrow coincidence window where  $G_{\perp}(\Delta t_{ab})$  is significantly larger than  $G_{\parallel}(\Delta t_{ab})$ . Similar to what has been used in the past [106], we choose  $T_c = -25 \leq \Delta t_{ab} \leq 25$  ns, a window (approximately) wide enough to include the longer of the two photon coherence times, and obtain  $V = 62 \pm 4\%$ .

This visibility value is not corrected for accidentals, and can be interpreted as the experimentally useful amount of interference that can be extracted if this experiment were to be implemented directly as a part of a quantum information protocol. Though much smaller

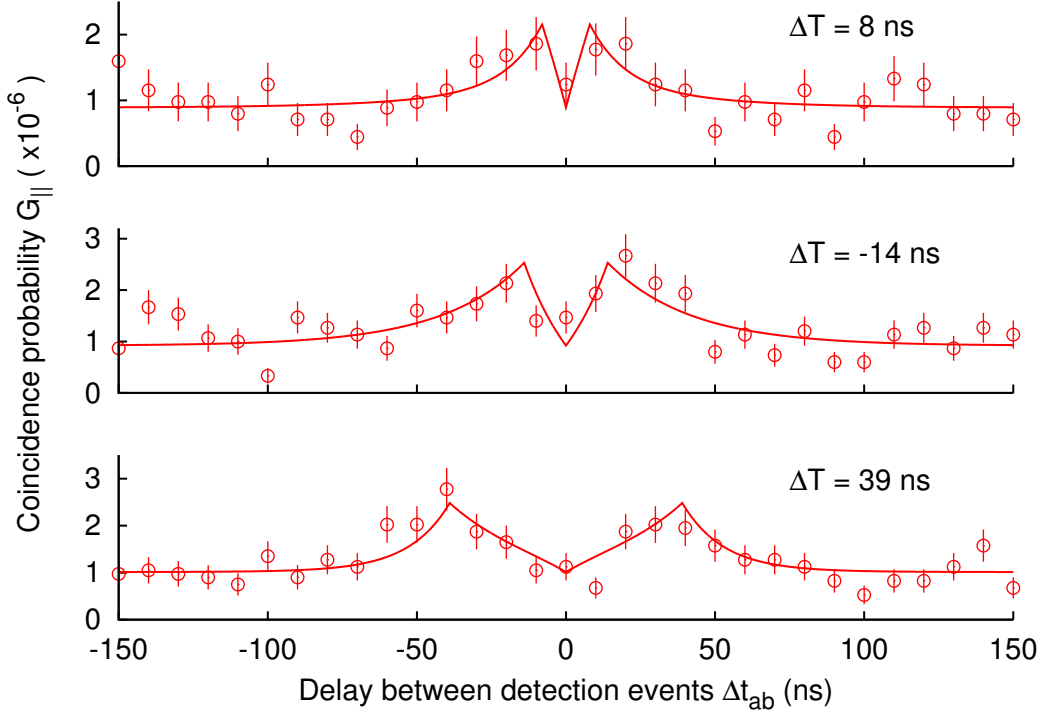


**Figure 3.19:** Coincidence probability for interfering photons  $G_{||}$  between  $D_a$  and  $D_b$ , measured for several values of  $\Delta T$ . The data is sorted into 10 ns wide time-bins and normalized to the total number of trigger events  $N_t$ . As  $|\Delta T|$  increases, the coincidence events are concentrated around two separate peaks at  $\Delta t_{ab} = \pm|\Delta T|$ . The solid lines represent  $G_{\text{acc}} + A \cdot G_{||}(\Delta t_{ab})$ , where  $G_{||}(\Delta t_{ab})$  is given by the solution of Eq. (3.10),  $G_{\text{acc}}$  is a constant offset describing the accidental coincidences, and  $A$  is a scaling factor. Error bars represent Poissonian statistics.

than the expected value, the uncorrected visibility is still larger than the standard quantum limit of 50%<sup>9</sup>.

Nevertheless, choosing a narrow  $T_c$  has its shortcomings: we exclude a portion of the detected coincidence events, and the remaining accidentals, though reduced, still degrade the visibility significantly. As such, the uncorrected visibility of  $V = 62 \pm 4\%$  reflects the technical limitations of our experiment in terms of detector noise and the heralding efficiency of the FWM source etc., rather than an underlying incompatibility of the photons themselves.

Therefore, we also adopt an alternative approach: we choose a large coincidence window  $T_c = -75 \leq \Delta t_{ab} \leq 75$  ns such that we include all relevant coincidence events, and correct for

<sup>9</sup> Though it is often quoted that a HOM visibility of  $>50\%$  cannot be explained in terms of classical particles (as opposed to photons) [54, 119], such visibilities have been demonstrated in specially engineered classical analogues of the HOM experiment [120, 121].

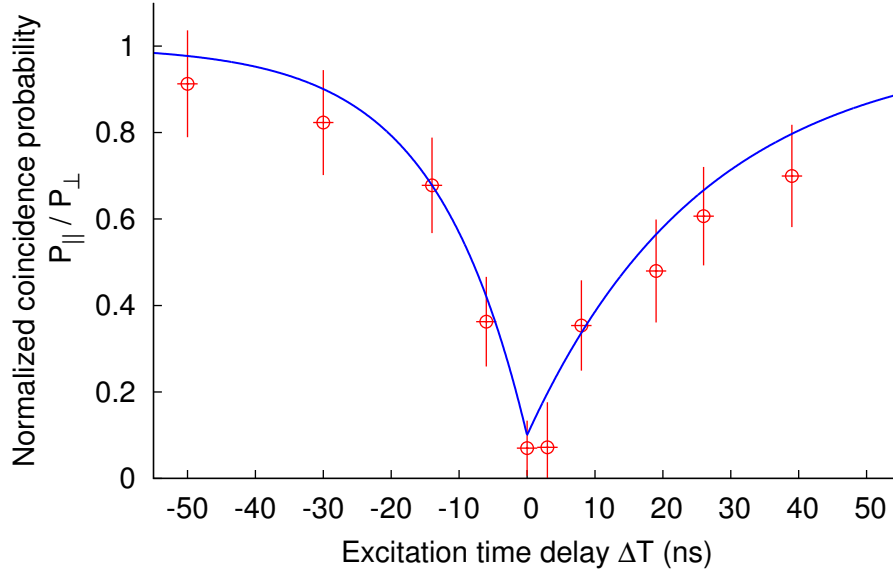


**Figure 3.20:** Normalized coincidence probability  $P_{\parallel}/P_{\perp} = 1 - V$ , corrected for accidental coincidences, showing the HOM dip. The solid line shows expected values obtained from Eq. (3.18). Vertical error bars represent Poissonian statistics, while horizontal bars reflect the uncertainty in the calibration of  $\Delta T$  due the APD timing jitter.

the accidental coincidences  $G_{\text{acc}}$  by fitting the data to the expected forms shown in Eq. (3.20) and (3.21). Doing so, we obtain a corrected visibility of  $V = 93 \pm 6\%$ , which is compatible with the expected value of  $90.0 \pm 1.5\%$ . The high visibility demonstrates the compatibility of the two single-photon sources.

### 3.6.2 HOM Dip

We now consider the results of varying the temporal overlap of the two photons by adjusting the delay time  $\Delta T$ , while maintaining  $\tau_f = 13.6$  ns. The delay is defined such that  $\Delta T > 0$  corresponds to the idler photon arriving after the photon from the single atom. The measured  $G_{\parallel}$  for several values of  $\Delta T$  are shown in Fig. 3.19. The measurement time for each setting of  $\Delta T$  is approximately 48 h.

As  $|\Delta T|$  increases, the coincidence events are concentrated around two separate peaks at  $\Delta t_{ab} = \pm|\Delta T|$ . Thus, to obtain the visibility  $V$  in a consistent manner across the whole range of  $\Delta T$  values, but without excluding significant portions of the detected coincidence events,  $T_c$  has to be much larger than the maximum value of  $|\Delta T|$  used in the experiment.

As before, we choose a large coincidence window  $T_c = -75 \leq \Delta t_{ab} \leq 75$  ns, correct for the accidental coincidences, and obtain  $P_{\parallel} = \sum_{T_c} G_{\parallel}(\Delta t_{ab})$ . We do not measure  $G_{\perp}$  again at

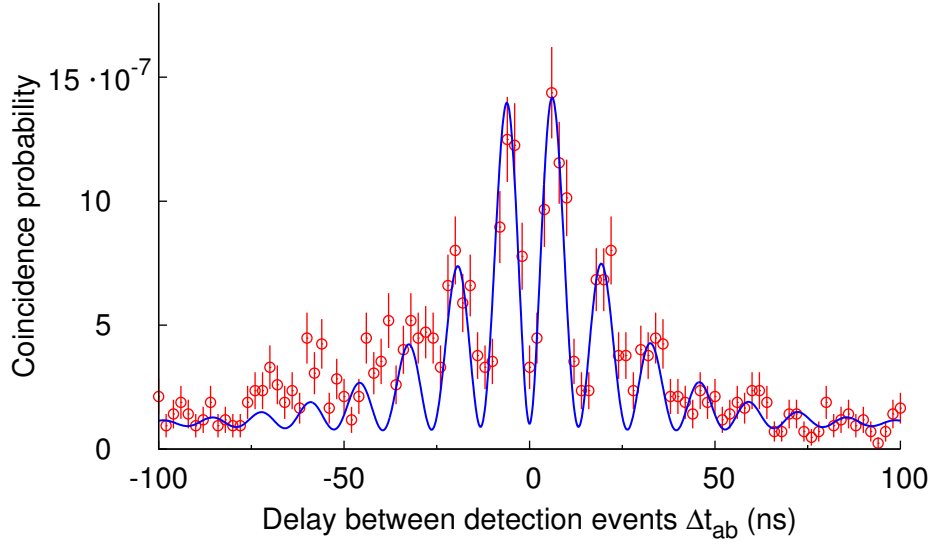


**Figure 3.21:** Quantum beats in the coincidence probability  $G_{\parallel}$  between  $D_a$  and  $D_b$ . The data is sorted into 2 ns wide time-bins and normalized to the total number of trigger events  $N_T$ . The finer time resolution allows us to resolve the temporal structure of the beat. The solid line is a fit to the form described by Eq. (3.24), with the free parameters being a scaling factor, an accidentals offset, and the detuning  $\delta$ . The obtained beat frequency of  $\delta/2\pi = 75.7 \pm 0.7$  MHz is consistent with the frequency difference between the two photons. Error bars represent Poissonian statistics.

different  $\Delta T$  values as  $P_{\perp}$  is not expected to depend on  $\Delta T$  [see Eq. (3.15)]; instead we use the  $P_{\perp}$  value measured at  $\Delta T = 0$  to obtain the visibilities.

In Fig. 3.20 we plot  $P_{\parallel}/P_{\perp} = 1 - V$ , and observe the familiar HOM dip [85]. The shape is slightly asymmetric, and can be described by two separate exponential curves with characteristic time constants corresponding to  $\tau_f$  and  $\tau_s$  [see Eq. (3.18)]. Most of the measured points lie within one standard deviation from the line, in good agreement with the theoretical predictions.

### 3.6.3 Quantum Beats

Here we vary the distinguishability of the photons by detuning the central frequencies of the photons with respect to each other. We set  $\Delta T = 0$  and  $\tau_f = 13.6$  ns, but we bypass the AOM in the idler photon path; the central frequency of the idler photon is therefore red-detuned by  $\delta/2\pi = 76$  MHz from the photon produced by the single atom.

The HOM interference of the two photons with different frequencies gives rise to quantum beats [97], as shown in Fig. 3.21. From Eq. (3.24) we expect the coincidence probability to

oscillate at the frequency difference of the photons. We obtain the beat frequency of  $\delta/2\pi = 75.7 \pm 0.7$  MHz from a fit to our data, consistent with the value measured independently.

### 3.6.4 Different decay times

In this measurement, we vary the temporal overlap of the photons by controlling the idler decay time  $\tau_f$ .

Previously, we quantified the HOM effect in the conventional way via the interference visibility, i.e. by comparing the measurements with interfering and non-interfering photons. To obtain the HOM dip, it sufficed to calculate the visibilities by comparing individual results for  $G_{\parallel}$  (at different  $\Delta T$ ) against a common  $G_{\perp}$  measurement. However, as we vary  $\tau_f$ , the heralding efficiency does not remain constant (see Fig. 3.15), and we can no longer rely on the  $G_{\perp}$  data taken at a fixed  $\tau_f$  value<sup>10</sup>.

Here we adopt an alternative way to quantify the HOM interference via the ratio  $P_{1,1}/P_{2,0}$ , where  $P_{1,1} = P_{\parallel}$  is the probability that the two photons exit the beam-splitter from different output ports,  $P_{2,0}$  is the probability that the two photons exit the beam-splitter on the same side, and  $P_{2,0} + P_{1,1} = 1$ . This ratio is related to the interference visibility  $V$  via [54]

$$\frac{P_{1,1}}{P_{2,0}} = \frac{1 - V}{1 + V} . \quad (3.29)$$

Experimentally, we measure the coincidence probability  $G$  between the detectors as before, and obtain

$$\frac{P_{1,1}}{P_{2,0}} = \alpha \cdot \frac{P_{a,b1} + P_{a,b2}}{P_{b1,b2}} , \quad (3.30)$$

where  $\alpha$  is a constant,  $P = \sum_{T_c} G$ , and the subscripts refer to the pairs of detectors involved. Again we use a large coincidence window  $T_c = -75 \leq \Delta t_{ab} \leq 75$  ns; accidental corrections for  $G$  are made by averaging over the background regions at large  $|\Delta t_{ab}|$ , and subtracting the value across all data points. In an ideal setup  $\alpha = \frac{1}{4}$ , but the actual value depends on the exact beam-splitter ratios and the relative efficiencies of the APDs. We measure  $\alpha$  independently by comparing the relative count rates at the different detectors with a fixed light input on one of the interferometer arms (while blocking the other input arm).

The results are shown in Fig. 3.22. The measured  $P_{1,1}/P_{2,0}$  ratios increase with a smaller  $\tau_f$ , signifying a weaker interference effect as the temporal mismatch between the photons grows. The increasing deviation from the expected values at smaller  $\tau_f$  is most likely due to

<sup>10</sup> In principle, we can circumvent this by also measuring  $G_{\perp}$  at each  $\tau_f$  value, but doing so would be much more time-consuming.

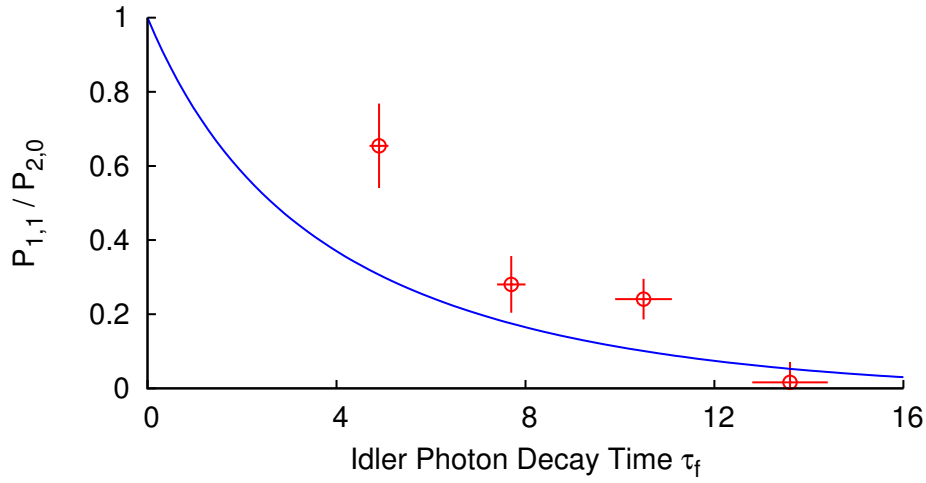


**Figure 3.22:** Measured ratios  $P_{1,1}/P_{2,0}$  at different idler photon decay times  $\tau_f$ . The solid line represents the expected values of  $1 - V/(1 + V)$ , where  $V$  is the HOM interference visibility. Vertical error bars represent Poissonian statistics, while horizontal bars represent the standard deviation in the distribution of measured  $\tau_f$  values.

the photon temporal profiles not being strictly exponential; the effect of the rising edge (for both photons) would become more significant when  $\tau_f$  is short.

### 3.7 Conclusion

We have presented the HOM interference between heralded photons from the FWM source, and the triggered photons generated via spontaneous emission from the single atom. Though based on the same atomic species, these two sources generate single photons through different physical processes. We observe a HOM visibility of  $V = 62 \pm 4\%$  (without accidental corrections) and  $V = 93 \pm 6\%$  (with accidental corrections), consistent with the expected value of  $90.0 \pm 1.5\%$ . We also study the changes in the two-photon interference as we introduce varying degrees of distinguishability between the photons, and our results agree well with theoretical predictions.

The observation of a high interference visibility without any spectral filtering demonstrates the compatibility of the two different physical systems. This gives us confidence that the single photons produced via FWM have the required spectral and timing characteristics to interact directly with the single atom efficiently.



# Chapter 4

## Scattering Dynamics with Single Photons

This chapter presents the time-resolved scattering of single photons by a single atom, using photons with exponentially rising and decaying profiles. First, we present the theory of the scattering process. Next, we introduce our method for generating exponentially rising probe photons, describe the experimental setup and its characterization, and present the experimental sequence. Finally, we discuss the experimental results and compare our observations for different photon shapes and bandwidths.

### 4.1 Introduction

Scattering of light by matter has been studied extensively in the past. Among the numerous scattering phenomena, the most fundamental process is the scattering of a single photon by a single atom. Yet, few experiments have explored this fundamental scattering process, due to challenges in simultaneously implementing the two critical ingredients: an efficient atom-light interface in free space, and a compatible source of single photons. So far, efforts include the single-photon spectroscopy by a single atom [122] or molecule [123].

However, to fully understand the interaction between a single photon and a single atom, we need to carry out time-resolved measurements and investigate the dynamics of the scattering process. Only very recently has there been a first report on the time-resolved absorption of single photons via a double heralding technique [124].

It is only in the time-resolved domain that we can address a prominent prediction of quantum optics: the deterministic absorption of a propagating photon by a single atom, provided the photon waveform matches the time-reversed version of the spontaneously emitted photon spatially and temporally [125–129].

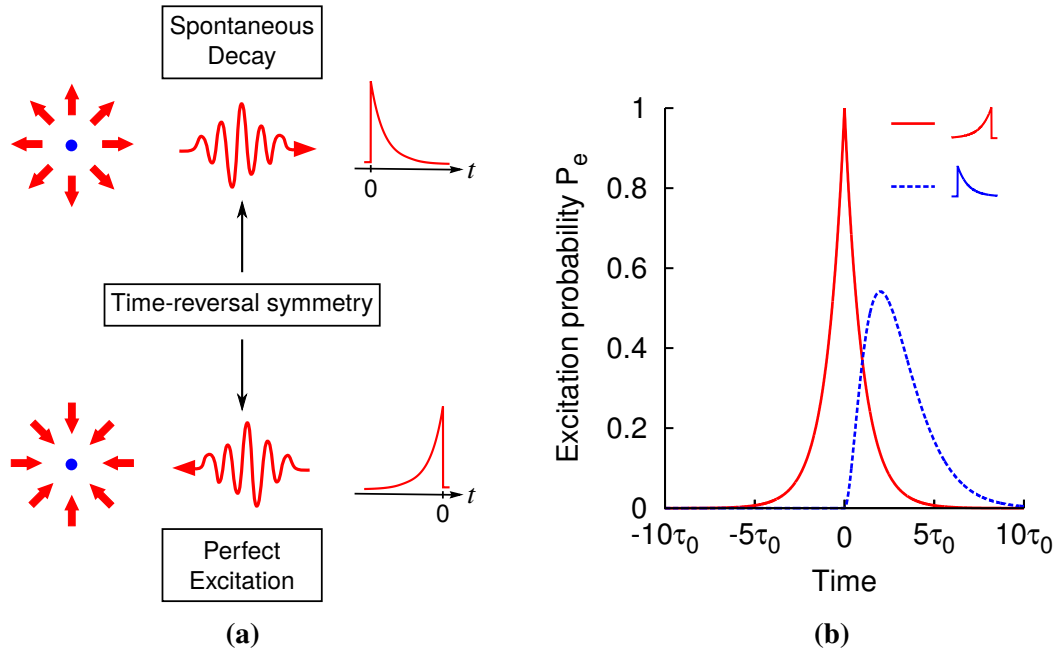


**Figure 4.1:** (a) Illustration of the time-reversal symmetry between spontaneous decay and perfect single-photon excitation. The spontaneous decay process emits an exponentially decaying photon in a spatial mode corresponding to the atomic dipole transition. Perfect single-photon excitation requires an exponentially rising photon propagating towards the atom with the same spatial mode. (b) Calculated excitation probability  $P_e(t)$  for both exponentially rising (red solid curve) and decaying (blue dashed curve) photon shapes, assuming perfectly matched bandwidths and spatial modes (see §4.2.2). The rising photon leads to perfect excitation, with a maximum  $P_e(t)$  value of 1; for the decaying photon, the maximum value is 0.56.

Fig. 4.1a illustrates the time-reversal principle. Consider a two-level atom in free space, initially in the excited state: the excited state population  $P_e(t)$  decays exponentially with a time constant given by the radiative lifetime  $\tau_0$ , emitting a photon with the same temporal decay profile in a spatial mode corresponding to the atomic dipole transition [130]. The time-reversal symmetry of the Schrödinger and Maxwell equations suggests that the perfect absorption of the photon requires the reverse of the spontaneous emission process: an incident photon having an exponentially rising temporal envelope with a matching time constant  $\tau_0$ , propagating towards the atom in the same spatial mode.

Fig. 4.1b shows the evolution of the excited state population when exciting the atom with such an exponentially rising photon, with a maximum of  $P_e(t) = 1$  (see §4.2.2 for analytical expressions). In contrast, an exponentially decaying photon in the same spatial mode can only achieve a maximum of  $P_e(t) = 0.56$ . Although both photon shapes give rise to different

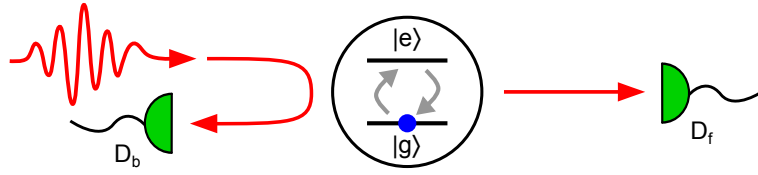


**Figure 4.2:** Concept of the scattering experiment. An incident single photon excites a two-level atom in free space. The time evolution of the atomic excited state population  $P_e(t)$  can be inferred by measuring the photons at the forward and backward detectors  $D_f$  and  $D_b$ .

transient atomic excitation, we note that the overall probability of the photon being scattered by the atom remains the same for both shapes due to their identical Lorentzian power spectra.

In our experiment, we investigate the influence of the photon temporal profile on the scattering dynamics. So far, demonstrations of more efficient photon absorption via temporal shaping have used either attenuated laser fields as the light source [32] or an optical cavity as an analogue of the single atom [34, 131]. Here, we perform an experimental test using single photons and a single atom, and measure the  $P_e(t)$  for photons with exponentially rising and decaying shapes.

#### 4.1.1 Idea of the Experiment

The HOM experiment (Chapter 3) demonstrated that the heralded single photons from the FWM source are compatible with the spontaneously emitted photons from the single atom; from this we infer that these photons can efficiently excite the single atom. Thus, we use the heralded idler photons as the probe photons for the scattering experiment.

Fig. 4.2 describes the central concept of the experiment. We focus the probe photons onto the single atom, excite the  $|g\rangle = 5S_{1/2}, F=2, m_F = -2 \rightarrow |e\rangle = 5P_{3/2}, F'=3, m'_F = -3$  transition of the effective two-level system (see Fig. 3.1b,c), and simultaneously measure the photons arriving at the forward and backward detectors  $D_f$  and  $D_b$ .

Inferring the atomic excited state population  $P_e(t)$  from the measurements at  $D_b$  is relatively straightforward, as we directly measure the atomic fluorescence. Alternatively, we can reconstruct  $P_e(t)$  from the measurements at  $D_f$  by considering the difference in the photon rates measured with and without the trapped atom. We obtain  $P_e(t)$  via both methods and compare the results.

## 4.2 Theory

### 4.2.1 A Two-Level Atom and a Single-Photon Fock State

We consider the interaction of a two-level atom, initially in the ground state, with an excitation pulse described by a single-photon Fock state, and study the probability  $P_e(t)$  of finding the atom in the excited state at any time  $t$ . The evolution of  $P_e(t)$  depends on

1. The natural transition linewidth  $\Gamma_0 = 1/\tau_0$ ,
2. The photon probability amplitude  $\xi(t)$  at the position of the atom,
3. The overlap between the photon and the dipole pattern of the atomic spontaneous emission  $\Lambda \in [0, 1]$ , where  $\Lambda = 1$  corresponds to a complete spatial mode overlap.

Our starting point is the analysis presented in Ref. [127]: with the help of the Weisskopf-Wigner approximation [130], the atom-photon coupling strength  $g(t)$  is defined as

$$g(t) = \sqrt{\Lambda\Gamma_0}\xi(t) , \quad (4.1)$$

and the atomic dynamics can be modeled with following set of coupled differential equations:

$$\dot{\mathbf{s}}(t) = M\mathbf{s}(t) + \mathbf{b} , \quad (4.2)$$

with

$$M = \begin{pmatrix} -\Gamma_0 & -2g(t) & -2g^*(t) \\ 0 & -\Gamma_0/2 & 0 \\ 0 & 0 & -\Gamma_0/2 \end{pmatrix}, \quad \mathbf{b} = \begin{pmatrix} -\Gamma_0 \\ -g^*(t) \\ -g(t) \end{pmatrix},$$

$$\mathbf{s}(t) = \begin{pmatrix} \langle g, 1_p, 0_e | \hat{\sigma}_z(t) | g, 1_p, 0_e \rangle \\ \langle g, 0_p, 0_e | \hat{\sigma}_+(t) | g, 1_p, 0_e \rangle \\ \langle g, 1_p, 0_e | \hat{\sigma}_-(t) | g, 0_p, 0_e \rangle \end{pmatrix}, \quad (4.3)$$

where  $\langle g, 1_p, 0_e |$  describes the two-level atom in the ground state, the excitation pulse mode as a single-photon Fock state, and the environment in the vacuum state. The atomic operators are  $\hat{\sigma}_+ = |e\rangle\langle g|$ ,  $\hat{\sigma}_- = |g\rangle\langle e|$ ,  $\hat{\sigma}_z = |e\rangle\langle e| - |g\rangle\langle g|$ .

The initial state of the system is  $|g, 1_p, 0_e\rangle$ , i.e.

$$\mathbf{s}^T(t_0) = (-1, 0, 0). \quad (4.4)$$

The excited state population is given by the first component of the vector  $\mathbf{s}$ :

$$P_e(t) = \frac{1}{2} [s_1(t) + 1]. \quad (4.5)$$

Further assuming that  $g(t)$  is real, we can simplify the differential equations in Eq. (4.3) to:

$$\dot{P}_e(t) = -\Gamma_0 P_e(t) - 2g(t)s_2(t) \quad (4.6)$$

$$\dot{s}_2(t) = -\frac{\Gamma_0}{2}s_2(t) - g(t), \quad (4.7)$$

where  $s_2(t)$  is the second component of the vector  $\mathbf{s}$ .

We now consider the evolution of  $P_e(t)$  using Eq. (4.6) and the initial condition  $P_e(t_0) = 0$ . The excited state population can only either increase (via excitation, by absorbing the incoming photon) or decrease (via decay, by emission of a photon). The term  $-\Gamma_0 P_e(t)$  is the scattering rate given by the standard treatment of a two-level atom [40], and represents the decay of the excited state; we thus identify  $-2g(t)s_2(t) \geq 0$  as the instantaneous atomic absorption<sup>1</sup>.

### 4.2.2 Exponential Temporal Envelopes

We now apply the above model to the single photons we use in the experiment, which have exponential temporal envelopes with a Lorentzian bandwidth  $\Gamma_p = 1/\tau_p$ . The decaying and rising shapes are described by, respectively,

$$\begin{aligned} \xi_{\downarrow}(t) &= \frac{1}{\sqrt{\tau_p}} e^{-\frac{t}{2\tau_p}} \Theta(t) \\ \xi_{\uparrow}(t) &= \frac{1}{\sqrt{\tau_p}} e^{\frac{t}{2\tau_p}} \Theta(-t), \end{aligned} \quad (4.8)$$

---

<sup>1</sup>From the solutions of  $s_2(t)$  in Eq. (4.10) and (4.12), we see that  $s_2(t) \leq 0$ , and thus  $-2g(t)s_2(t) \geq 0$ .

where  $\Theta(t)$  is the Heaviside step function, and find the corresponding solutions

$$P_{e,\downarrow}(t) = \begin{cases} \frac{4\Lambda\tau_0\tau_p}{(\tau_0 - \tau_p)^2} \left[ e^{-\frac{1}{2\tau_0}t} - e^{-\frac{1}{2\tau_p}t} \right]^2 \Theta(t) & \text{for } \tau_p \neq \tau_0 \\ \frac{\Lambda t^2}{\tau_0^2} e^{-t/\tau_0} \Theta(t) & \text{for } \tau_p = \tau_0 \end{cases} \quad (4.9)$$

$$s_{2,\downarrow}(t) = \begin{cases} -\frac{2\sqrt{\Lambda\tau_0\tau_p}}{\tau_0 - \tau_p} \left[ e^{-\frac{1}{2\tau_0}t} - e^{-\frac{1}{2\tau_p}t} \right] \Theta(t) & \text{for } \tau_p \neq \tau_0 \\ -\frac{\sqrt{\Lambda}t}{\tau_0} e^{-\frac{\Gamma_0}{2}t} \Theta(t) & \text{for } \tau_p = \tau_0 \end{cases} \quad (4.10)$$

$$= -\sqrt{P_{e,\downarrow}(t)}$$

$$P_{e,\uparrow}(t) = \frac{4\Lambda\tau_0\tau_p}{(\tau_0 + \tau_p)^2} \left[ e^{\frac{1}{\tau_p}t} \Theta(-t) + e^{-\frac{1}{\tau_0}t} \Theta(t) \right] \quad (4.11)$$

$$s_{2,\uparrow}(t) = -\frac{2\sqrt{\Lambda\tau_0\tau_p}}{\tau_0 + \tau_p} \left[ e^{\frac{1}{2\tau_p}t} \Theta(-t) + e^{-\frac{1}{2\tau_0}t} \Theta(t) \right] = -\sqrt{P_{e,\uparrow}(t)} \quad (4.12)$$

The maximum excitation probabilities are

$$P_{e,\max,\downarrow} = 4\Lambda \left( \frac{\tau_0}{\tau_p} \right)^{\frac{\tau_p + \tau_0}{\tau_p - \tau_0}} \quad \text{at } t = \frac{2\tau_0\tau_p}{\tau_0 - \tau_p} \ln \left( \frac{\tau_0}{\tau_p} \right) , \quad (4.13)$$

$$P_{e,\max,\uparrow} = \frac{4\Lambda\tau_0\tau_p}{(\tau_0 + \tau_p)^2} \quad \text{at } t = 0 . \quad (4.14)$$

Complementary to the time-resolved atomic dynamics, we can also consider the time-integrated extinction  $\varepsilon$ , which is the overall reduction in the number of transmitted photons due to the atom-light interaction. This is equivalent to the fraction of incident photons that are scattered into a different spatial mode from the excitation pulse mode. Thus, with the scattering rate  $\Gamma_0 P_e(t)$ , we can obtain the extinction via

$$\varepsilon = (1 - \Lambda) \int_{-\infty}^{+\infty} \Gamma_0 P_e(t) dt = \Lambda(1 - \Lambda) \frac{4\tau_p}{\tau_0 + \tau_p} , \quad (4.15)$$

where the factor  $(1 - \Lambda)$  describes all other free-space modes that do not overlap with the excitation pulse. In contrast to the transient interaction, the time-integrated extinction  $\varepsilon$  is equal for both photon shapes.

### 4.2.3 Forward and Back-Scattered Photons

We can now link these results to our experimental observables: measuring the scattering of the photons in the forward and backward directions. For now, we assume detectors with perfect efficiency. The excited state population  $P_e(t)$  can be directly measured using the atomic fluorescence in the backward direction:

$$R_b(t) = \eta_b \Gamma_0 P_e(t) , \quad (4.16)$$

where  $R_b(t)$  is the detection probability per unit time, and  $\eta_b$  is the collection efficiency.

In the forward direction, where we measure the excitation pulse mode, the corresponding detection probability is  $R_{f,0}(t) = |\xi(t)|^2$  without an atom in the trap. When an atom is present, the transmission of the single-photon pulse is altered via two processes: absorption and re-emission into the pulse mode. As such, the detection probability becomes

$$\begin{aligned} R_f(t) &= R_{f,0}(t) - \underbrace{[-2g(t)s_2(t)]}_{\text{absorption}} + \underbrace{\Lambda \Gamma_0 P_e(t)}_{\text{re-emission}} \\ &= \left| \xi(t) - \sqrt{\Lambda \Gamma_0 P_e(t)} \right|^2 , \end{aligned} \quad (4.17)$$

where we have used Eq. (4.1) and (4.9)-(4.12).

From the final expression, we can interpret the extinction as the destructive interference between the incident excitation field and the portion of the scattered field that overlaps with the pulse mode<sup>2</sup>. The time-resolved difference in forward detection probabilities with and without the atom is

$$\begin{aligned} \delta_f(t) &= R_{f,0}(t) - R_f(t) = -2g(s)s_2(t) - \Lambda \Gamma_0 P_e(t) \\ &= \dot{P}_e(t) + (1 - \Lambda) \Gamma_0 P_e(t) , \end{aligned} \quad (4.18)$$

where the final expression is obtained by substituting Eq. (4.6), and we can now obtain  $P_e(t)$  by integrating Eq. (4.18).

As the atom eventually decays back to the initial ground state, i.e.  $\int_{-\infty}^{+\infty} \dot{P}_e(t) dt = 0$ , extending the integration limit to  $t \rightarrow \infty$  yields the same time-integrated extinction  $\varepsilon$  as in Eq. (4.15):

$$\int_{-\infty}^{+\infty} \delta_f(t) dt = (1 - \Lambda) \int_{-\infty}^{+\infty} \Gamma_0 P_e(t) dt = \varepsilon . \quad (4.19)$$

<sup>2</sup> The destructive interference (as indicated by the minus sign in Eq. 4.17) is due to a  $\pi$  phase shift between the incident and scattered fields, for which an explanation can be found in Ref [132].

### 4.3 Preparing Exponentially Rising Probe Photons

We have already introduced the production of exponentially decaying single idler photons from the FWM setup by heralding on the signal photon. However, the production of exponentially rising single photons is generally more difficult. We could herald on the idler photon instead to generate a rising signal photon [35], but it would be of a different frequency which is not resonant to the a ground state transition in  $^{87}\text{Rb}$ . Alternatively, we could directly modulate the heralded idler photon [131, 133, 134], but the losses would be inevitably huge due to the small overlap between an exponentially rising and decaying profile.

Instead, we generate exponentially rising probe photons by inverting the temporal profile of the exponentially decaying idler photons, using an asymmetric Fabry-Pérot cavity [128] and the well-known temporal correlation properties of photon pairs [135]. We note that this is a technique designed to convert between exponentially decaying and rising profiles, and does not work as a general ‘photon shape inverter’ for arbitrary temporal profiles.

This technique has been demonstrated in [34, 131]; here we will briefly explain how it works, and describe our implementation.

#### 4.3.1 Working Principle

##### Perfect Loading of Cavity: Exponential Rise $\rightarrow$ Exponential Decay

We start by describing how an exponentially rising photon shape can be inverted to an exponential decay, as illustrated in Fig. 4.3a. For an asymmetric cavity with a partially reflective mirror  $M_1$  and a highly reflective mirror  $M_2$ , a photon incident on  $M_1$  will either be directly reflected or be coupled to the cavity mode.

Now consider a photon incident on  $M_1$  that is resonant to the cavity, and has a rising exponential temporal envelope with a time constant that matches the cavity ring-down time, i.e. the photon and cavity have matching bandwidths. The waveforms of the direct reflection and the leakage of the cavity mode through  $M_1$  will destructively interfere and completely cancel out, thus no light is reflected and the photon is completely loaded into the cavity. The photon subsequently exits the cavity through  $M_1$  with an exponentially decaying temporal profile, thus inverting the photon shape.

As no light is lost from the cavity through  $M_2$ , all incident light is eventually reflected regardless of its coupling into the cavity.

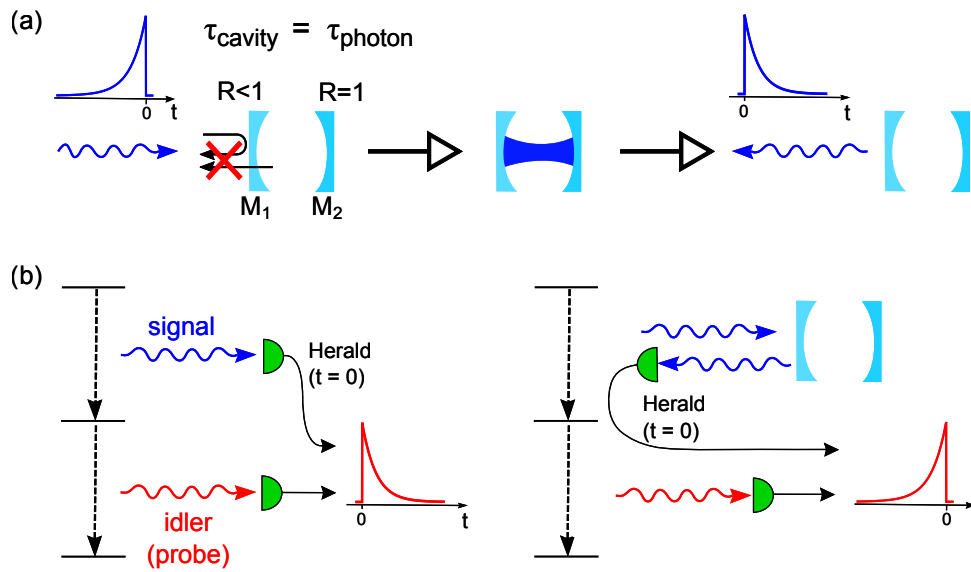


**Figure 4.3:** (a): Inverting an exponentially rising photon. If such a photon is sent to an asymmetric resonant bandwidth-matched cavity, the waveforms of the direct reflection and the leakage of the cavity mode through mirror  $M_1$  destructively interfere and completely cancel out, thus no light is reflected and the photon is completely loaded into the cavity. The photon subsequently exits the cavity with an exponentially decaying temporal profile. (b): If the signal photon from FWM is sent to such a cavity prior to its detection, the shape of the heralded idler (probe) photon is transformed from an exponential decay to an exponential rise.  $R$ : reflectivity of cavity mirror.

### Inverting the Idler Photon: Exponential Decay $\rightarrow$ Exponential Rise

The above-mentioned shape inversion does not work directly for the heralded idler photon, as it has an exponentially decaying shape. Instead, we send the signal photon, which has an exponentially rising field when heralding on the idler photon [35], to the asymmetric cavity prior to its detection as a herald (see Fig. 4.3b). The cavity imparts a frequency-dependent phase shift to the signal field, which is also ‘imprinted’ onto the heralded idler photon due to the correlation properties of the photon pair. The result is the inversion of the idler photon shape from an exponential decay to an exponential rise.

### Physical Interpretation

Nonetheless, it might seem counter-intuitive that by only manipulating the signal field (and not the idler), we can control the temporal shape of the idler photon and even influence its interaction with an atom. Here we consider a physical interpretation of the heralding process in the context of the scattering experiment.

The FWM source generates photon pairs probabilistically. Without heralding, we can treat the idler photons as a (very) weak continuous beam, but the photon rate is too low to detect a meaningful signal in this manner. To pinpoint the time window in which we can find the atom in the excited state, we rely on the heralding process to provide a timing reference; it is with respect to the heralding signal that the idler photon has an exponentially decaying temporal profile.

By sending the signal photon to the cavity prior to its detection, we modify the heralding process to produce an exponentially rising idler profile, effectively improving the timing reference by providing a higher probability for finding the atom in the excited state *at a particular instant in time*. The transformation of temporal profiles does not alter the power spectrum of the photon, and thus would not affect the overall extinction.

### Mathematical Description

For completeness (and perhaps adding some clarity to the discussion), we reproduce the summarized mathematical description of the process found in [2, 34]. Due to the cascade decay in the FWM process, the signal photon is generated before the idler, and thus both photons emerge with a well-defined time order. The resulting two-photon amplitude wavefunction is

$$\psi(t_s, t_i) = A e^{-(t_i - t_s)/2\tau} \Theta(t_i - t_s) , \quad (4.20)$$

where  $t_s, t_i$  are the detection times of the signal and idler photons, and  $\Theta(t)$  is the Heaviside step function. Heralding on the signal photon yields an idler photon with an exponentially decaying temporal envelope starting at  $t_i = t_s$ .

The effect of the cavity on the signal mode can be described as a frequency-dependent phase factor [136, 137]:

$$C(\delta') = \frac{\sqrt{R_1} - \sqrt{R_2} e^{i\delta'/\Delta\nu_f}}{1 - \sqrt{R_1 R_2} e^{i\delta'/\Delta\nu_f}} , \quad (4.21)$$

where  $R_{1,2}$  are the reflectivities of  $M_{1,2}$ ,  $\Delta\nu_f$  is the free spectral range of the cavity, and  $\delta'$  is the detuning from the cavity resonance. The cavity then transforms the two-photon wavefunction in Eq. (4.20) into

$$\tilde{\psi}(t_s, t_i) = \mathcal{F}_s^{-1} [C(\omega_s - \omega_{s,0} - \delta_s) \cdot \mathcal{F}_s[\psi(t_s, t_i)]] , \quad (4.22)$$

where  $\mathcal{F}_s$  denotes a Fourier transform from  $t_s$  to  $\omega_s$ , and  $\delta_s$  is the detuning of the cavity resonance from the signal photon central frequency  $\omega_{s,0}$ . If  $R_2 = 1$ , and  $R_1$  is chosen such

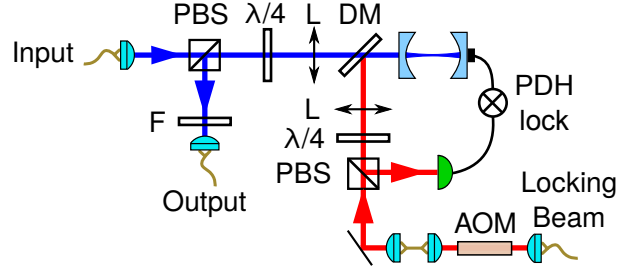


**Figure 4.4:** Cavity setup for controlling the temporal shape of the probe photon. The heralding photons are sent to an asymmetric bandwidth-matched cavity, and the reflected light is then collected into another single-mode fiber. An auxiliary 780 nm laser is used to stabilize the cavity length using the Pound-Drever-Hall (PDH) technique. The acousto-optic modulator (AOM) in the auxiliary beam path brings the cavity into or out of resonance with the input light. PBS: polarizing beam-splitter,  $\lambda/4$ : quarter-wave plate, L: lens, DM: dichroic mirror, F: interference filter.

that the cavity is bandwidth-matched to the photon, then

$$\tilde{\psi}(t_s, t_i) = \frac{A}{\sqrt{1 + 4\delta_s^2 \tau^2}} \left[ 2\delta_s \tau e^{-(t_i - t_s)/2\tau} \Theta(t_i - t_s) + e^{(t_i - t_s)/2\tau} \Theta(-t_i + t_s) \right], \quad (4.23)$$

with both exponentially rising and decaying components, weighted by the detuning  $\delta_s$ . For large  $\delta_s$ , the effect of the cavity is negligible, while for  $\delta_s = 0$  we get an inversion of the temporal envelope:

$$\tilde{\psi}(t_s, t_i) = A e^{(t_i - t_s)/2\tau} \Theta(-t_i + t_s). \quad (4.24)$$

Heralding on the signal photon now produces an idler photon with a rising exponential envelope.

### 4.3.2 Implementation

The cavity setup is illustrated in Fig. 4.4. The cavity itself comprises of a highly reflective mirror (ATFilms) and a partially reflective mirror (Layertec), and its main properties are:

Property	Value
Cavity length	125 mm
Mirror radius of curvature	200 mm
Reflectivity $R_1$ (in-coupling mirror)	0.943
$R_2$	0.9995
Finesse	$103 \pm 5$
Cavity decay time	$13.6 \pm 0.5$ ns

An auxiliary frequency-locked 780 nm laser is used to stabilize the cavity using the Pound-Drever-Hall (PDH) technique [138, 139], which is very similar to the feedback mechanism used to frequency-lock our lasers. We control the temporal shape of the probe photon via the AOM, which sets the cavity resonance frequency; by tuning the cavity on or far-off-resonance (70 MHz) with respect to the central frequency of the heralding signal photon, we obtain exponentially rising or decaying probe photons.

The input and locking beams are combined with a dichroic mirror (780 nm interference filter, Semrock MaxLine LL01-780-12.5, FWHM 3 nm). Both beams are coupled to the cavity with focusing lenses of focal lengths 300 mm and 450 mm, respectively. The coupling of light to fibers is done with aspheric lenses (Thorlabs C230TMD-B for input/output fibers, Thorlabs A375TM-B for the locking beam). The total transmission of the input light through the cavity setup is  $\approx 40\%$ .

## 4.4 Experimental Setup

Fig. 4.5 shows the joint experimental setup for the scattering experiment. The details of the single atom and FWM setups have mostly been described in Chapter 2. The detection of a signal photon heralds the presence of a probe photon in the idler mode. Prior to its detection, the heralding signal photon is sent to an asymmetric bandwidth-matched cavity which controls its temporal profile, as described in §4.3.

### 4.4.1 Optical Path of the Probe Photons

At the single atom setup, the probe light is sent along the same path as the optical pump beam, but in the opposite direction. This configuration avoids losing 99% of the probe photons at the 99:1 beam-splitter, but does not affect the collection of photons in the backward direction.

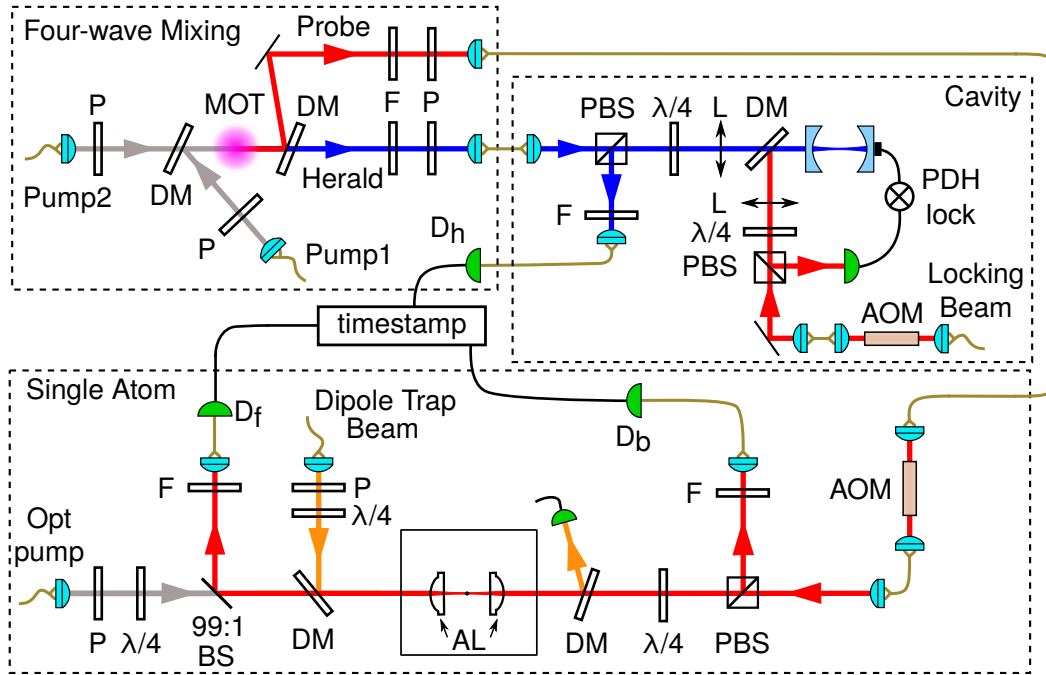


**Figure 4.5:** Schematic of the full setup for the scattering experiment, consisting of the FWM setup (top left), the cavity setup for controlling the temporal profile of the probe photon (top right), and the single atom setup (bottom). AOM: acousto-optic modulators, DM: dichroic mirrors, P: polarizers, F: interference filters,  $\lambda/4$ : quarter-wave plates, (P)BS: (polarizing) beam splitters,  $D_b$ ,  $D_f$ ,  $D_h$ : avalanche photodetectors.

The incident probe photons are circularly polarized to excite the  $\sigma^-$  transition of the single atom, and the photons emitted by the atom in the backward direction are also circularly polarized, but of the opposite handedness with respect to the propagation direction (compared to the probe photons).

Therefore, the probe light can be separated from the atomic emission in the backward direction by a QWP and a PBS; while the incoming probe photons are transmitted, the photons emitted by the atom are reflected at the PBS, and are subsequently filtered and collected into a single-mode fiber. This arrangement reduces the amount of MOT fluorescence measured at  $D_b$ , thus we use  $D_f$  to detect the presence of the trapped atom.

There are also several waveplates in the probe optical path (not shown in Fig. 4.5) which are adjusted to maximize the transmission through the PBS. The transmission does not drift by more than a few percent over several days, signifying a good passive polarization stability along the entire optical path.

#### 4.4.2 Optical Switch for the Probe Photons

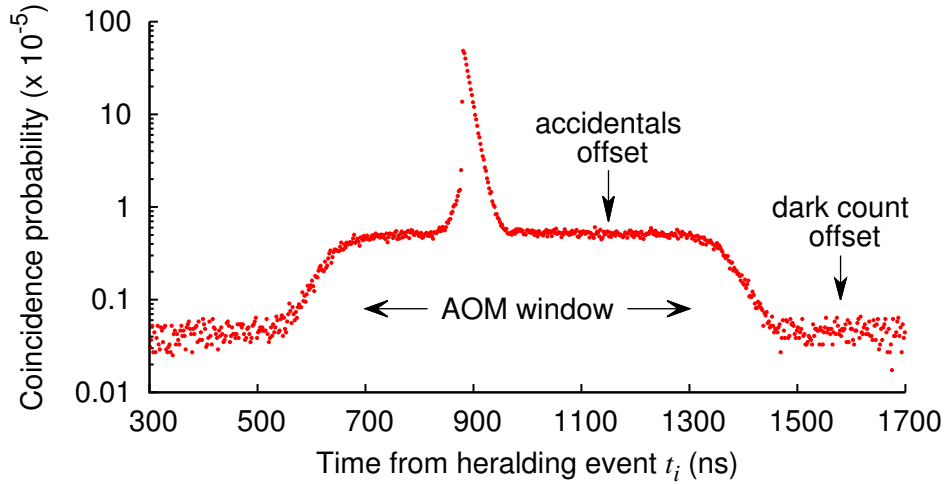
We use an AOM to shift the central frequency of the probe photons to compensate for the AC Stark shift and Zeeman shift experienced by the single atom (see Appendix A), thus ensuring that the probe photons excite the single atom on resonance. The AOM also functions as an optical switch for the probe photons, which is important for several reasons:

- The single atom should not receive any light from the FWM setup until the atomic state is correctly prepared, and the system is ready to measure the scattering of the probe photons.
- The FWM setup continually cycles between MOT cooling and photon pair generation phases. During the cooling phase, the collection mode for the probe photons contains a significant amount of MOT fluorescence at 780 nm which will interact with the atom, causing unwanted heating of the atom and interfering with its prepared state.
- During the pair generation phase, there are many photons in the probe collection mode which are uncorrelated to the detection events at the heralding detector  $D_h$  (this is due to the limited heralding efficiency). Likewise, we want to minimize the effect of these uncorrelated photons on the atom.

As such, the AOM is turned on for a 600 ns window only when the following conditions are met:

- The single atom is in the correctly prepared state, and the experimental sequence is at a measurement window (see §4.6.1).
- The FWM setup is at the pair generation phase.
- There is a heralding detection event at  $D_h$ .

However, consider a heralding event at the very end of a  $10 \mu\text{s}$  photon pair generation interval: the AOM window would still stay open for a few 100 ns after the corresponding probe photon has passed through and the MOT beams are starting to turn on, and thus some unwanted MOT fluorescence will still reach the atom. A similar situation occurs if the heralding event takes place at the very start of the photon pair generation window, and some MOT fluorescence from the previous cooling step is transmitted through the AOM. As such, we additionally insert a  $1 \mu\text{s}$  waiting time between each MOT cooling and photon pair generation step in the FWM sequence; during this waiting time, all pump and MOT beams at the FWM setup are turned off.



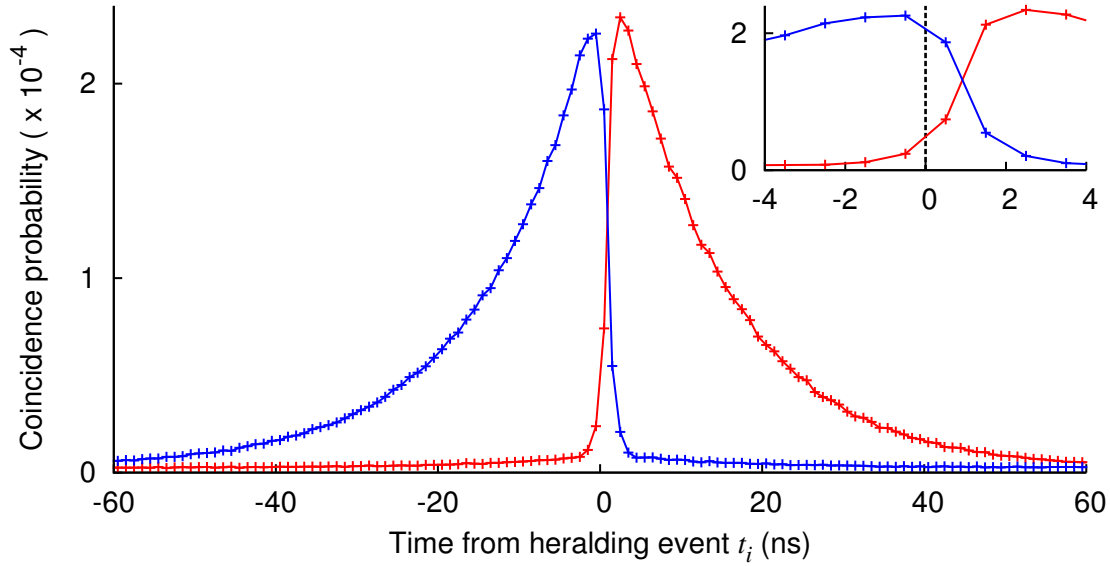
**Figure 4.6:** Coincidence probability between  $D_h$  and  $D_f$ , plotted on a semi-log scale to highlight the 600 ns AOM window and the two different offset levels: a lower level mainly caused by dark counts at  $D_f$ , and a higher level corresponding to the accidentals offset in our experimental data. The latter is primarily due to light from the FWM setup which is uncorrelated to the heralding photons. The time-bin size is 2 ns, and the probe photon decay time is  $\tau_p \approx 13.5$  ns. The detection times here have not been offset to account for electrical and optical delays.

Fig. 4.6 shows an extended temporal profile of the probe photon together with the AOM window. Accidental coincidences result in a constant offset in the measured data, above that of contributions from APD dark counts. Therefore, the window is chosen to be wider than the duration of the probe photon so that the intervals within the AOM window during which the probe photons do not contribute significantly can be used to correct for accidental coincidences (see §4.7.1).

Similar to the HOM experiment, to allow sufficient time to turn on the AOM upon the detection of a heralding photon, the probe photon travels through a 230 m long single-mode fiber to delay its arrival to the single atom setup.

## 4.5 Preliminary Characterizations

Before we embark on the actual measurement campaign, we perform a few preliminary measurements to properly characterize our setup.



**Figure 4.7:** Coincidence histograms between the heralding detector  $D_h$  and the forward detector  $D_f$  for exponentially decaying (red curve) and rising (blue curve) probe photons of decay time  $\tau_p = 13.3$  ns. We choose between the decaying and rising temporal shapes by setting the cavity detuning to 70 MHz or zero (on resonance) with respect to the heralding photon central frequency, respectively. The time-bin width is 1 ns. Due to imperfections of the cavity setup (spatial alignment, bandwidth matching, etc.), there is a residual tail in the measured profile at  $t_i < 0$  ( $t_i > 0$ ) for the decaying (rising) shape. A common offset of 879 ns is applied to account for delays introduced by optical and electrical delay lines, and the reference point  $t_i = 0$  is marked in the zoomed-in region (see inset).

#### 4.5.1 Timing References

To study the scattering dynamics, we want to measure the time-resolved atomic response in relation to the incident probe photons. In the forward direction, we can directly measure the probe photons without an atom in the trap by considering the coincidence histograms between the heralding detector  $D_h$  and the forward detector  $D_f$ , as shown in Fig. 4.7. Using these histograms as a reference, we offset all detection times at  $D_f$  by 879 ns to account for delays introduced by optical and electrical delay lines<sup>3</sup>.

<sup>3</sup> Due to the effect of the cavity, there is a  $\approx 3$  ns offset between the peaks of the exponentially rising and decaying profiles. We choose to use a common offset for both shapes instead of defining a separate  $t_i = 0$  for each shape using the peak of the each profile. The measured profiles are not perfect exponentials as described Eq. (4.8); therefore, to best match the theoretical predictions of our model with the experimental results, the offset is chosen to be slightly asymmetric with respect to the two profiles (see inset of Fig. 4.7).

However, a similar timing reference does not exist in the backward direction, as  $D_b$  does not directly measure the probe light. We are also unable to use the same offset used for  $D_f$  due to differences in optical path lengths and electronic signal propagation.

Instead, we can precisely determine the timing offset between the two detectors by exploiting the nature of the single atom as a single quantum emitter. We illuminate the trapped single atom with the MOT beams, and measure the  $g^{(2)}$  between the MOT fluorescence detected by  $D_b$  and  $D_f$ , similar to that shown in Fig. 2.5. Suppose a photon emitted by the atom is detected at  $D_f$ , then we define  $\Delta t_f$  as the time between the emission and the APD click being recorded on the timestamp unit (likewise,  $\Delta t_b$  for  $D_b$ ). As the single atom cannot emit two photons simultaneously, the coincidence histogram will yield an anti-bunching feature centered at  $\Delta t_f - \Delta t_b$ , indicating the timing offset between the APDs<sup>4</sup>.

We measure  $\Delta t_b = \Delta t_f + 12$  ns, and thus offset all detection times at  $D_b$  by 891 ns.

## 4.5.2 Collection and Detection Efficiencies

### Measurements in the Forward Direction

For the scattering measurements in the forward direction, we can deduce the atomic response by comparing the data recorded with and without the trapped atom, and normalize our results against the latter. Thus we do not require an explicit knowledge of the collection and detection efficiencies.

However, the fraction of the transmitted probe light which we collect does influence the measured extinction value [30, 140]. The extinction is the destructive interference between the incident excitation field and the scattered field (as described by Eq. 4.17); if the amplitude of the scattered field is comparable to the (small) fraction of the collected probe, it is possible to measure artificially large extinctions when the two fields interfere destructively, or a ‘transmission’ of >100% [141, 142] when the fields interfere constructively (which obviously violates energy conservation).

Therefore, the extinction is a rigorous measure of the atom-light interaction only if we collect all (or at least a macroscopic fraction of) the probe light, without preferentially filtering out more probe than scattered light. At the same time, this does not imply that the collection has to be lossless: introducing a neutral density filter into the forward collection arm would not change the measured extinction (apart from signal-to-noise issues).

<sup>4</sup> Due to the dead time limitation of our timestamp unit, we additionally introduce an extra 362 ns delay line (the extra delay is independently measured) between the timestamp and one of the APDs via a long cable. The extra delay is subtracted from the results.

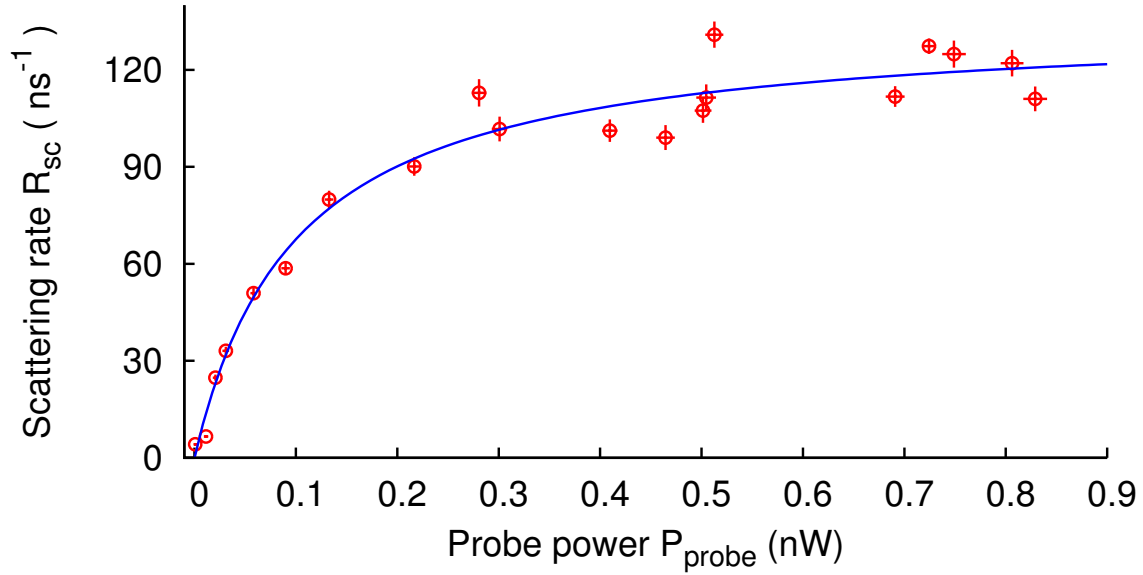


**Figure 4.8:** The measured scattering rate  $R_{\text{sc}}$  at the backward APD  $D_b$  as a function of the probe power  $P_{\text{probe}}$ , showing the saturation behaviour of the single atom as the probe power is increased. Error bars represent Poissonian statistics. The large scatter of the data points at higher  $P_{\text{probe}}$  values is likely due to parameter drifts which were not characterized.

In our setup, the forward collection efficiency is  $\eta_{f,\text{col}} = 0.46 \pm 0.01$  for the transmitted probe light. We obtain  $\eta_{f,\text{col}}$  by sending laser light down the probe beam path, and comparing its power directly after passing through the cuvette and after the collection fiber.

### Measurements in the Backward Direction

In the backward direction, we do not collect any probe light which can serve as a reference, thus we need to factor in collection and detection efficiencies in both directions to extract the excitation probability  $P_e$  from these measurements (see later section §4.7.2 for details). The APDs used in this experiment are Perkin Elmer SPCM-AQR-15 modules, with detection efficiencies of  $\eta_{f,\text{det}} = 0.52 \pm 0.01$  and  $\eta_{b,\text{det}} = 0.56 \pm 0.01$  in the forward and backward directions, respectively (see Appendix D for calibration details).

The backward collection efficiency is less straightforward to measure. Unlike in the forward direction, where we could simply use laser light and measure its power, here we need to measure the atomic emission directly in order to determine the collection efficiency.

Instead of using single photons from the FWM source, we use an attenuated laser beam to probe the same  $\sigma^- 5S_{1/2}, F=2, m_F=-2 \rightarrow 5P_{3/2}, F'=3, m'_F=-3$  transition on resonance

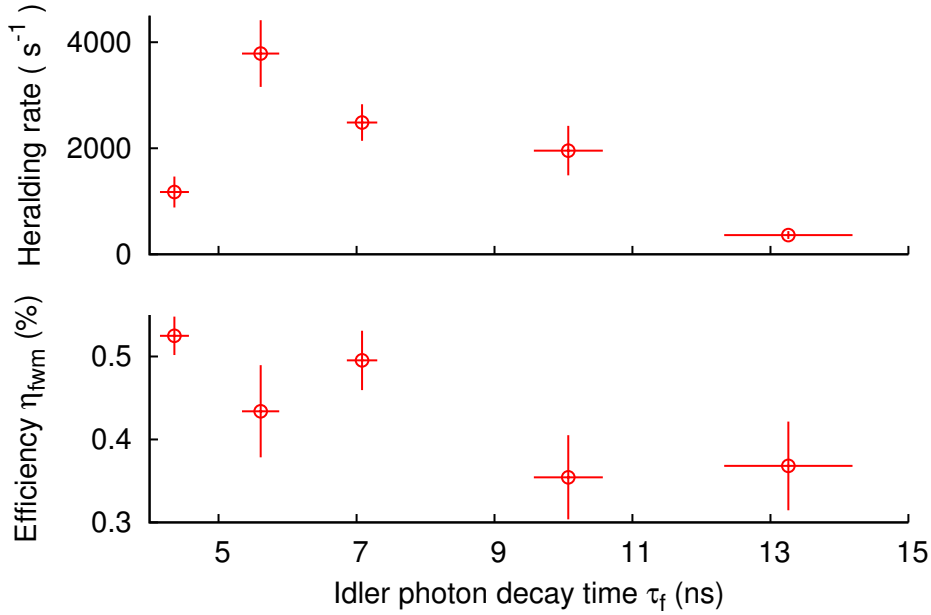


**Figure 4.9:** Heralding rates and efficiencies of the FWM source at different probe photon decay times  $\tau_p$  during the scattering experiment. Error bars reflect the standard deviation in the distribution of the measured values.

(see Fig. 4.8). The measured scattering rate at  $D_b$  is given by [39, 40]

$$R_{sc} = \eta_{b,col} \eta_{b,det} \frac{\Gamma_0}{2} \frac{P_{probe}/P_{sat}}{1 + (P_{probe}/P_{sat})}, \quad (4.25)$$

where  $P_{probe}$  and  $P_{sat}$  are the probe and saturation powers, respectively. After correcting for background counts and fitting the results to Eq. (4.25), we obtain  $\eta_{b,col} = 0.0126 \pm 0.0005$  and  $P_{sat} \approx 100$  pW.

### 4.5.3 FWM Rates and Efficiencies

The performance of the FWM source depends on the operating parameters and desired probe (idler) photon decay time  $\tau_p$ . Again we focus on  $\tau_p \approx 13.5$  ns, for which we achieve an overall heralding rate<sup>5</sup> of  $300 - 450 s^{-1}$  and a pair rate of  $1 - 1.5 s^{-1}$ . These rates are lower than during the HOM experiment due to a different sequence duty cycle, as well as the deteriorating power output of the 762 nm pump laser.

<sup>5</sup> For this experiment, the FWM setup alternates between  $140 \mu s$  of MOT cooling and  $10 \mu s$  of photon pair generation, thus the ‘instantaneous’ rate during the pair generation window itself is a factor of 15 higher.

To obtain shorter decay times, we generate an optically denser atomic ensemble by increasing the quadrupole magnetic field gradient. However, during the scattering experiment, we could only achieve decay times of down to  $\tau_p \approx 5.5$  ns with this method. To reliably generate probe photons with  $\tau_p \approx 4.5$  ns, we additionally increase the two-photon detuning  $\Delta_2$ ; this also decreases the heralding rate, but not prohibitively so.

Unlike in the HOM experiment, we do not control the pump powers to keep the heralding rate constant for different  $\tau_p$ ; here the single-photon excitation is much weaker than the intense  $\pi$  pulses sent to the atom during the HOM experiment, thus the influence of a higher rate on the atom lifetime is negligible.

The heralding efficiency is  $\eta_{\text{fwm}} = N_{\text{pairs}}/N_{\text{t}}$ , where  $N_{\text{t}}$  is the detected number of heralding photons at  $D_{\text{h}}$ , and  $N_{\text{pairs}}$  is the number of coincident detections of the heralding photons at  $D_{\text{h}}$  and probe photons at  $D_{\text{f}}$ , i.e. the detected number of photon pairs. The heralding rates and efficiencies are measured during the experiment when the atom is lost from the trap (see §4.6.3), and the results after correcting for accidentals are shown in Fig. 4.9. We note that the uncorrected  $\eta_{\text{fwm}}$  values are  $\sim 5\%$  higher than the corrected the ones.

The total transmission and detection efficiency of the probe photons (without the trapped atom) is  $\sim 0.05$ . Besides the forward collection and detection efficiencies  $\eta_{f,\text{col}}, \eta_{f,\text{det}}$  which are reported above, the other losses include (approximately): the 230 m delay fiber (40%)<sup>6</sup>, the single-pass AOM and re-coupling into the fiber (40%), and the cumulative effect of other smaller optical losses along the optical path.

#### 4.5.4 Transmission of a Weak Coherent Field

To characterize the atom-light coupling, we perform the scattering measurement not with single photons, but with a weak coherent field. Such a measurement has been done previously with an experimental geometry that is very similar to our current setup, and is reported in [28]. Thus, the ability to reproduce the results reported therein will indicate that the efficiency of the atom-light coupling in our setup is close to what we should expect, and serve as a sanity check in preparing for the scattering experiment. Additionally, it will be interesting to directly compare the results for single photon vs coherent state excitation.

#### Methods

Our methods are similar to those reported in [28]. We use a weak continuous-wave laser beam to probe the  $\sigma^- 5S_{1/2}, F=2, m_F=-2 \rightarrow 5P_{3/2}, F'=3, m'_F=-3$  transition on resonance,

<sup>6</sup> See footnote 7 in §3.4.3 (pg. 52).

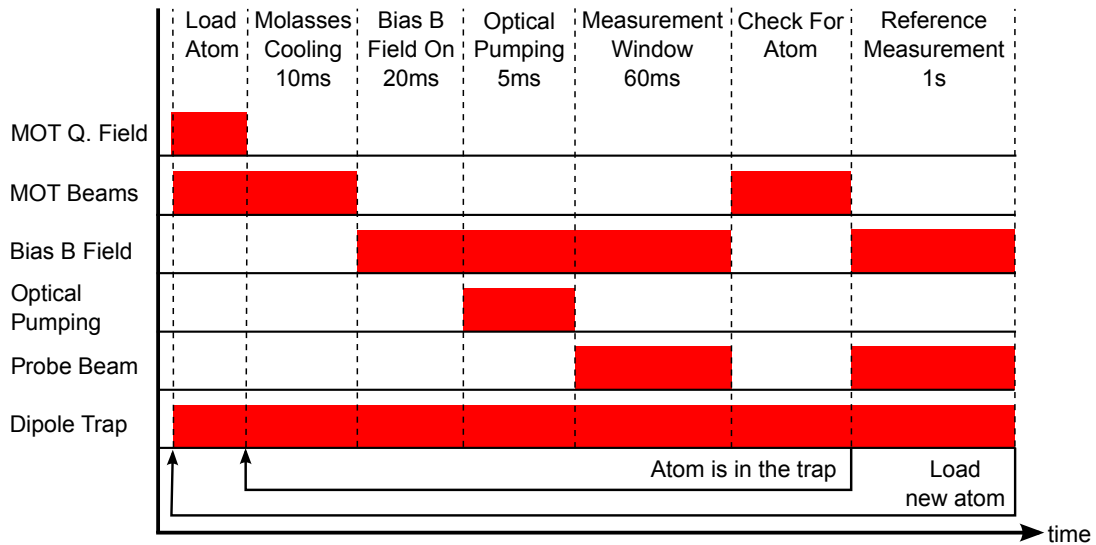


**Figure 4.10:** Experimental sequence for measuring the transmission of a weak coherent field.

and stay in the weak excitation regime with a detected probe photon rate kept at  $\sim 7000 \text{ s}^{-1}$  at the forward detector  $D_f$ .

The experimental sequence is shown in Fig. 4.10, and the steps are as follows:

1. Turn on the MOT, and wait for an atom to be loaded into the dipole trap.
2. Turn off the MOT quadrupole field, and perform molasses cooling for 10 ms.
3. Turn off the MOT beams, turn on the bias magnetic field of  $\approx 7$  Gauss, and wait 20 ms for it to stabilize<sup>7</sup>.
4. Perform 5 ms of optical pumping to the  $|g\rangle = 5S_{1/2}, F=2, m_F = -2$  dark state. Both the pumping and repump light are sent to the atom via the probe beam path.
5. Send the probe beam to the atom for 60 ms.
6. Check for the presence of the atom. The bias magnetic field is turned off, and the MOT beams (but not the quadrupole field) is turned on.

- If the atom is present, the data collected in this sequence is considered valid.

Repeat sequence from step 2.

<sup>7</sup> The step is taken as an extra precaution to ensure the quantization axis is properly set before performing to the optical pumping. For the other sequences presented in the thesis that omit this step (bias field and optical pumping beams are turned on simultaneously), the optical pumping should still work as its duration is sufficiently long.

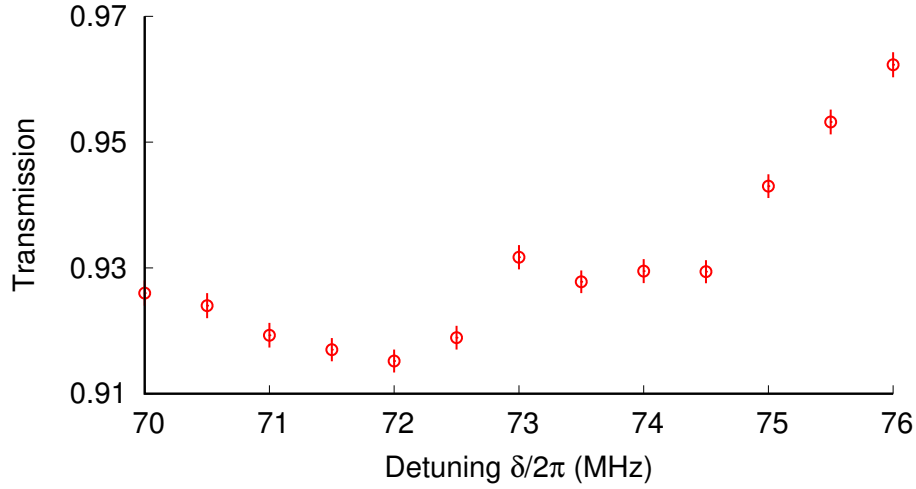


**Figure 4.11:** Transmission of a weak coherent field as a function of the detuning of the probe from the bare atomic transition, showing a maximum extinction of 8.5% on resonance at  $\delta/2\pi = 72$  MHz. Error bars represent Poissonian statistics.

- If the atom is lost, the data collected in this sequence is discarded. Perform a reference measurement without an atom in the trap, using a measurement window of 1 s. The bias magnetic field is also turned on to replicate the experimental conditions when the atom was present. After that, turn on the MOT and load another atom.

### Data Analysis

We obtain a transmission value  $T$  for each atom trapping event via the ratio of the detected count rates with and without the atom:

$$T = \frac{N_m / (n_{\text{seq}} \cdot \tau_m)}{N_r / \tau_r}, \quad (4.26)$$

where  $n_{\text{seq}}$  is the number of valid sequences,  $N_m$ ,  $N_r$  are the number of detected photons at  $D_f$  with and without the atom, respectively, and  $\tau_m = 60$  ms and  $\tau_r = 1$  s refer to the measurement times within the sequence. The overall result is then the average of  $\sim 100$  of such values, each weighted by  $\frac{(n_{\text{seq}} \cdot \tau_m) \tau_r}{(n_{\text{seq}} \cdot \tau_m) + \tau_r}$ .

The rationale behind the weight function is as follows: The probe beam power is not actively stabilized, and can drift between the measurement phases with and without the atom. Thus, each value of  $T$  is most reliable when the total measurement time  $n_{\text{seq}} \cdot \tau_m$  is equal to the reference measurement time  $\tau_r$ , and less so when one is much shorter compared to the

other. As such, we also choose  $\tau_r$  to approximately match the average lifetime of the atom during the experiment.

## Results

Fig. 4.11 shows the results as a function of the probe beam detuning  $\delta$  from the bare atomic transition. We measure a maximum extinction  $1 - T$  of  $8.5 \pm 0.2\%$  on resonance at  $\delta/2\pi = 72$  MHz. The measured value is also in fair agreement with the value of 9.8% reported in [28]; The discrepancy is most likely due to the frequency stability of the probe laser, which suffers from a slow drift in the set point of its frequency lock. Further attempts to optimize the alignment of the probe beam did not lead to significant improvements in the measured extinction values.

Thus, our results indicate that we are ready to proceed with the scattering experiment.

## 4.6 Running the Experiment

### 4.6.1 Experimental Sequence

The full experimental sequence is shown in Fig. 4.12.

#### Single Atom Setup

For the single atom setup, the steps are:

1. Turn on the MOT, and wait for an atom to be loaded into the dipole trap.
2. Turn off the MOT quadrupole field, and perform molasses cooling for 10 ms.
3. Turn off the MOT beams, turn on the bias magnetic field of  $\approx 7$  Gauss, and wait 20 ms for it to stabilize<sup>8</sup>.
4. Execute two measurement cycles, each consisting of:
  - (a) 5 ms of optical pumping to the  $|g\rangle = 5S_{1/2}, F=2, m_F = -2$  dark state. Both the pumping and repump light are sent to the atom via the probe beam path. The periodic optical pumping ensures that the atom stays in the ground state of the cycling transition throughout the whole sequence.

---

<sup>8</sup>see footnote 7 on pg. 85.

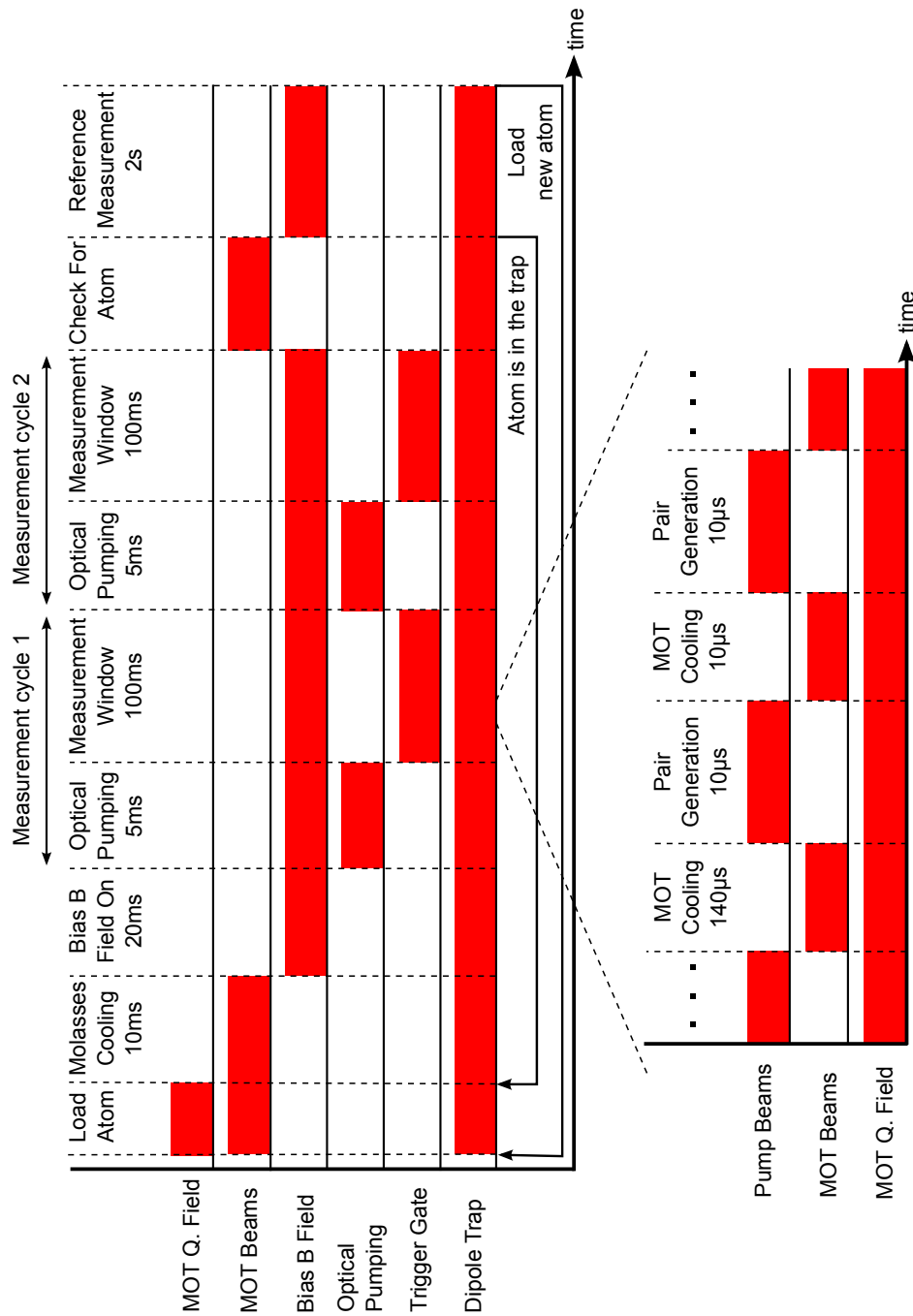


**Figure 4.12:** Experimental sequence of the scattering experiment for the single atom setup (top) and the FWM setup (bottom). The two sequences run asynchronously. When the trigger gate is opened during the 100 ms measurement window, a heralding event at  $D_h$  triggers the activation of the probe photon AOM for 600 ns.

- (b) 100 ms measurement window. The trigger gate is opened, and a heralding detection event at  $D_h$  triggers the activation of the probe photon AOM for 600 ns.
5. Check for the presence of the atom by monitoring atomic fluorescence at APD  $D_f$ . The bias magnetic field is turned off, and the MOT beams (but not the quadrupole field) is turned on.
- If the atom is present, the data collected in this sequence is considered valid. Repeat sequence from step 2.
  - If the atom is lost, the data collected in this sequence is discarded. Perform a reference measurement without an atom in the trap, using a measurement window of 2 s. The bias magnetic field is also turned on to replicate the experimental conditions when the atom was present. After that, turn on the MOT and load another atom.

The handling of these triggers is further illustrated in Fig. 4.13. If the trigger arrives at the single atom setup during the measurement window, it is recorded and used to trigger both the AOM and the gate unit. APD clicks from  $D_f$  and  $D_b$  are recorded only if they occur within a  $2 \mu\text{s}$  window starting from the arrival for a trigger signal. This avoids the recorded data files from being unnecessarily large due to APD clicks from MOT fluorescence, background light etc<sup>9</sup>.

With our choice of the number and duration of measurement cycles, the atom remains trapped for an average of  $\sim 7$  sequences before it is lost.

### FWM Setup

The FWM sequence alternates between  $140 \mu\text{s}$  of MOT cooling and  $10 \mu\text{s}$  of photon pair generation with a  $1 \mu\text{s}$  waiting time in between each step, and is run continuously without any synchronization with the single atom setup. During photon pair generation, the detection of a heralding photon generates a trigger signal which is sent to the single atom setup.

### Alternating of Photon Shapes

To avoid any systematic bias caused by slow drifts in the probe photon decay time  $\tau_p$  and the FWM heralding efficiency  $\eta_{\text{fwm}}$ , we alternate between the exponentially rising and decaying

<sup>9</sup> We actually only need to record APD clicks within the AOM window; the  $2 \mu\text{s}$  duration is simply chosen for convenience.

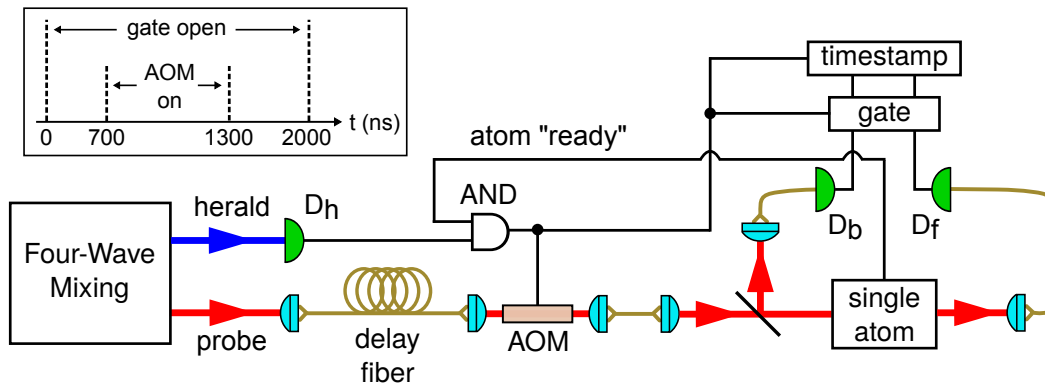


**Figure 4.13:** Signal handling scheme for the scattering experiment. Each heralding detection event at  $D_h$  generates a trigger signal. After the atom is optically pumped and the sequence is at the measurement window, the single atom setup sends a “ready” signal to the AND gate; the admitted trigger signals are then recorded, and used to trigger the AOM and the gate unit. The gate unit transmits clicks from  $D_b$  and  $D_f$  to the timestamp unit within a  $2 \mu\text{s}$  window from the trigger. The inset shows these events on a timeline starting from a trigger signal arriving at the AND gate.

photon shapes by changing the cavity resonance frequency approximately every 20 mins (see §4.3.2).

#### 4.6.2 Monitoring the Probe Photon Decay Times

To monitor the probe photon decay time  $\tau_p$ , we measure the coincidences between the heralding detector  $D_h$  and the forward detector  $D_f$  during the reference measurements, i.e. when the atom is lost from the trap. Doing so, we obtain the temporal profile of the probe photons which are unaltered by the atom, similar to those shown in Fig. 4.7, from which we can extract  $\tau_p$  from an exponential fit.

However, the inversion of the decaying photons only works exactly if the photons are bandwidth-matched to the cavity. Should  $\tau_p$  drift, the rising photons will not have a strictly exponential envelope, and thus extracting  $\tau_p$  via an exponential fit is not a useful tool for monitoring it.

Therefore, as we alternate between the photon shapes, we only monitor  $\tau_p$  for the decaying photons by performing an exponential fit on data accumulated over every 40–60 min of measurements for the decaying photons (corresponding to 2–3 alternating cycles), such that there is sufficient data for a sensible fit (fit error  $\lesssim 0.8$  ns for  $\tau_p \approx 13.5$  ns). The frequent alternation between the two photon shapes means that if the measured  $\tau_p$  for the

decaying photons is suitably close to the desired value, the rising photons would also have an exponential profile very close to what we expect.

Based on our measurements, we adjust the quadrupole coil current (and hence the OD of the cloud) at the FWM setup to keep  $\tau_p$  constant. We also discard the data recorded when  $\tau_p$  drifts too far away from the desired value.

### 4.6.3 Monitoring the FWM Rates & Efficiencies

Similar to the decay times, we also monitor the FWM rates and efficiencies using the data recorded during the reference measurements. For both decaying and rising photon shapes, we analyse the data accumulated over every 100 atom trapping events ( $\approx 15\text{--}20$  mins measurement time), during which we detect enough photon pairs to yield a value with a relative uncertainty of  $\sim 5\%$  based on Poissonian statistics.

Any deterioration in the FWM source performance usually indicates an instability in the frequency lock or power of the pump lasers, or occasionally a need to re-optimize the alignment of the pump and collection modes.

## 4.7 Results

In this section we present the results of the scattering experiment [143].

First, we focus on probe photons with a decay time of  $\tau_p = 13.3$  ns. By analyzing the measurements of the transmitted probe light in the forward direction, we investigate the atomic dynamics and overall extinction for the two photon shapes. Next, we compare the excitation probability  $P_e(t)$  inferred from the measurements in both the forward and backward directions. Finally, we consider the dependence of the overall extinction on  $\tau_p$ .

### 4.7.1 Forward Direction: Scattering Dynamics, Overall Extinction

The coincidence histograms between the heralding detector  $D_h$  and the forward detector  $D_f$  for probe photons with decay times  $\tau_p = 13.3$  ns are shown in Fig. 4.14. The total measurement time is 1500 hours, during which we record  $6 \cdot 10^8$  heralding events.

#### Reference Measurements

During the reference measurements, when no atom is trapped, we obtain the reference histograms  $G_{f,0}(t_i)$  for both exponentially decaying and rising probe photons, with time-bins

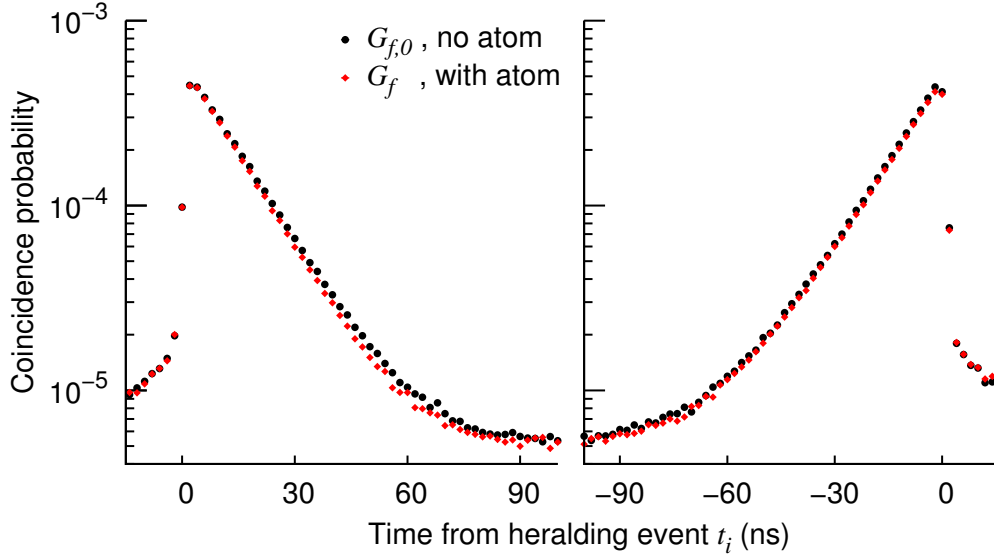


**Figure 4.14:** Coincidence histograms between the heralding detector  $D_h$  and the forward detector  $D_f$  for exponentially decaying (**left**) and rising (**right**) probe photons. Black circles ( $G_{f,0}$ ): reference measurements performed without the trapped atom. Red diamonds ( $G_f$ ): data recorded with the atom present. The decay time is  $\tau_p = 13.3 \pm 0.1$  ns obtained from a fit of  $G_{f,0}$  for the decaying photon. The time-bin width is  $\Delta t = 2$  ns. Error bars representing Poissonian statistics are smaller than the symbol size. Detection times are offset by 879 ns to account for delays introduced by electrical and optical lines.

$t_i$  of width  $\Delta t$ . Using an exponential fit to  $G_{f,0}(t_i)$  for the decaying photon, we obtain  $\tau_p = 13.3 \pm 0.1$  ns, where the uncertainty is derived from the fit<sup>10</sup>.

### Analysis Windows

Based on the reference histograms, we can also define the coincidence windows  $T_c = -14 \leq t_i \leq 100$  ns for the decaying photons and  $T_c = -100 \leq t_i \leq 14$  ns for the rising photons, corresponding to a width of  $\approx 8.5 \tau_p$ . We include the regions  $t_i < 0$  ( $t_i > 0$ ) for the decaying (rising) photons to account for the experimentally imperfect exponential profiles. By limiting our data analysis to these windows, we consider almost all relevant coincidence events, without including regions of  $t_i$  where the noise amplitude becomes significant compared to the signal.

<sup>10</sup> The uncertainty directly obtained from the overall histogram is different from the error bar of  $\pm 0.9$  ns reported in Fig. 4.9, which reflects the standard deviation in the distribution of the measured values across the whole experiment. In both cases, the principal value  $\tau_p = 13.3$  ns is the same.

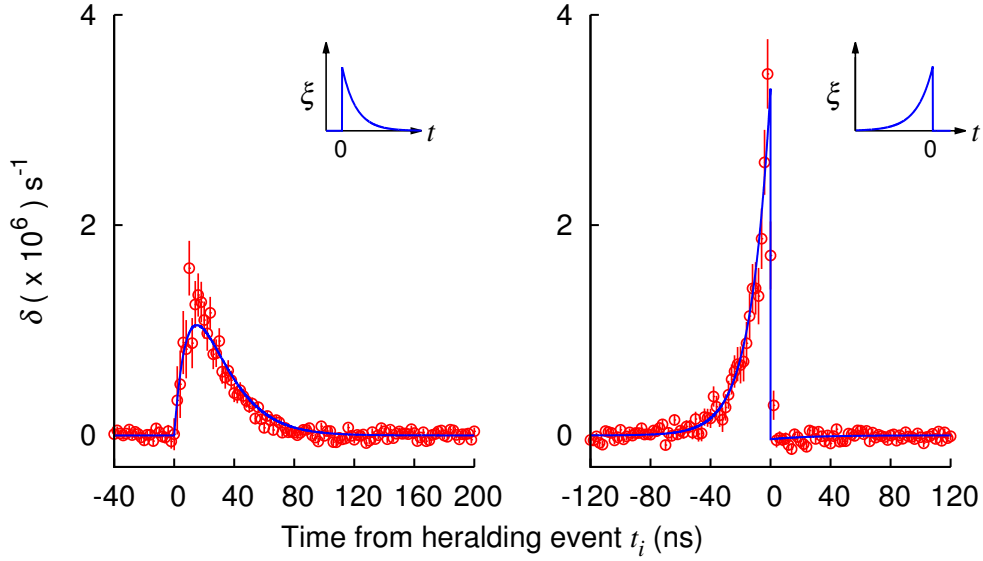


**Figure 4.15:** Differences in the detection probabilities per unit time  $\delta(t_i) = R_{f,0}(t_i) - R_f(t_i)$ , measured in the forward direction for exponentially decaying (**left**) and rising (**right**) probe photons.  $R_{f,0}(t_i)$  and  $R_f(t_i)$  are individually corrected for accidentals. The time-bin width is 2 ns. Error bars represent Poissonian statistics. Detection times are offset by 879 ns to account for delays introduced by electrical and optical lines. Solid lines are analytical solutions described by Eq. (4.18) for  $\tau_p = 13.3$  ns and  $\Lambda = 0.033$ .

Additionally, for each shape we define a combined 300 ns interval within the AOM window where the probe photons do not contribute significantly (see Fig. 4.6); we correct for accidentals by averaging the histograms across these intervals, and subtracting the value throughout.

### Scattering Dynamics

When the atom is trapped, we record the histograms  $G_f(t_i)$ . The scattering of probe photons by the atom is revealed in the differences between  $G_f(t_i)$  and  $G_{f,0}(t_i)$ ; however, the differences are rather small.

Thus, to see the scattering dynamics more clearly, we obtain the photon detection probabilities per unit time *per incident probe photon at the atom*

$$R_f(t_i) = \frac{G_f(t_i)}{\eta_{\text{fwm}} \cdot \Delta t}, \quad (4.27)$$

measured at the forward detector  $D_f$  with and without the atom, and consider the difference

$$\delta(t_i) = R_{f,0}(t_i) - R_f(t_i) \quad (4.28)$$

for both photon shapes, as shown in Fig. 4.15. Here, we normalise the measured histograms to the overall heralding efficiency  $\eta_{\text{fwm}} = \sum_{T_c} G_{f,0}(t_i) = (3.70 \pm 0.01) \cdot 10^{-3}$  (same for both shapes)<sup>11</sup>. As both  $G_f(t_i)$  and  $\eta_{\text{fwm}}$  are measured at  $D_f$ , we obtain a quantity independent of the collection and detection efficiencies in the forward direction, and is thus directly comparable to Eq. (4.18). A positive value of  $\delta(t_i)$  corresponds to net absorption, i.e. a reduction in the number of detected photons in the forward direction due to the interaction with the atom.

From our results, we clearly observe different absorption dynamics for exponentially rising and decaying photon shapes. For the decaying probe photon,  $\delta(t_i)$  rises from close to zero at  $t_i = 0$ , reaches a maximum at  $t_i \approx 15$  ns, then decays slowly. In stark contrast,  $\delta(t_i)$  for the rising probe photons follows the exponential envelope of the photon, with a peak absorption rate about twice as high as that for decaying probe photons. We can also compare our results to our theoretical model; our observations are best reproduced with the parameters  $\tau_p = 13.3$  ns and  $\Lambda = 0.033$ .

An alternative way to compare the absorption dynamics for both shapes is to consider the ratio of the photon detection rates  $R_f(t_i)/R_{f,0}(t_i)$ , as shown in Fig. 4.16. A net absorption of the probe light by the atom will result in a ratio below 1.

For the decaying probe photon, the ratio is close to 1 at  $t_i = 0$ , but steadily decreases even up till  $t_i = 60$  ns; this shows a surprisingly strong signature of the atom-light interaction even when the amplitude of the probe photon is small (for comparison, see Fig. 4.14). However, for the rising photon, the ratio stays relatively constant, again being distinctly different from that for the decaying photon.

We note that the analysis of the ratio  $R_f(t_i)/R_{f,0}(t_i)$  is only sensible for a limited range of  $t_i$ , as the noise in the obtained values quickly starts to dominate when the amplitude of the probe photon becomes too small.

## Overall Extinction

From the difference of the detection probabilities  $\delta(t_i)$ , we can also calculate the overall extinction  $\varepsilon = \Delta t \sum_{T_c} \delta(t_i) = 1 - \frac{\sum_{T_c} G_f(t_i)}{\sum_{T_c} G_{f,0}(t_i)}$ . We obtain similar extinction values  $\varepsilon_{\downarrow} = 4.21 \pm$

<sup>11</sup> Similar to footnote 10, the value here has a different uncertainty from  $\eta_{\text{fwm}} = (3.7 \pm 0.5) \cdot 10^{-3}$  reported in Fig. 4.9.

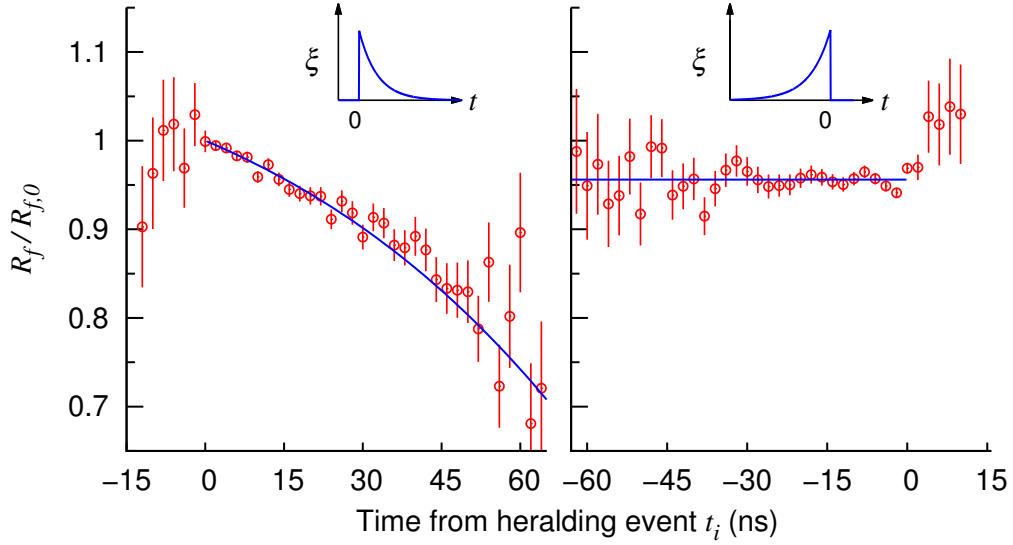


**Figure 4.16:** Ratio of the detection probabilities per unit time  $R_f(t_i)/R_{f,0}(t_i)$ , measured in the forward direction for exponentially decaying (**left**) and rising (**right**) probe photons.  $R_{f,0}(t_i)$  and  $R_f(t_i)$  are individually corrected for accidentals. The time-bin width is 2 ns. Error bars represent Poissonian statistics. Detection times are offset by 879 ns to account for delays introduced by electrical and optical lines. Solid lines are analytical solutions based on Eq. (4.17) for  $\tau_p = 13.3$  ns and  $\Lambda = 0.033$ .

0.18% and  $\varepsilon_\uparrow = 4.40 \pm 0.20\%$  for decaying and rising photons, respectively. Theoretically, from Eq. (4.15) we expect the same value  $\varepsilon = \Lambda(1 - \Lambda) \frac{4\tau_p}{\tau_0 + \tau_p}$  for both shapes. With our parameters  $\tau_p = 13.3$  ns and  $\Lambda = 0.033$ , this leads to  $\varepsilon = 4.29\%$ , in agreement with our experimental results.

We choose to calculate the extinction value from the overall histogram instead of taking the average of values obtained per single (or group of) atom loading event(s). This was done to reduce the bias in the final result; a further discussion of this issue is postponed to Appendix E.

## 4.7.2 Excitation Probability

Fig. 4.17 shows the excitation probability  $P_e(t_i)$  inferred from our measurements in both the forward and backward directions for  $\tau_p = 13.3$  ns.

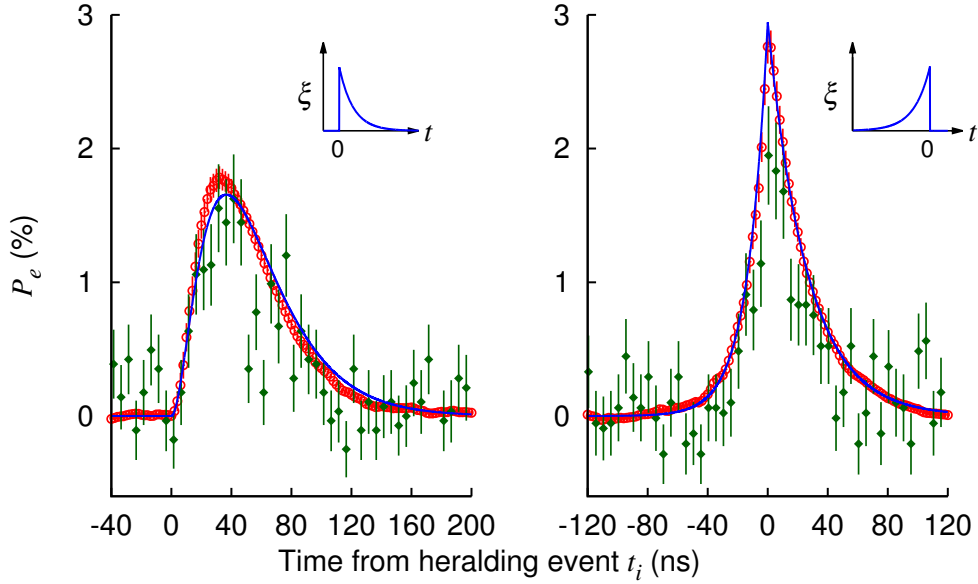


**Figure 4.17:** Atomic excited state population  $P_e(t_i)$  for exponentially decaying (**left**) and rising (**right**) probe photons. Results are obtained from the measurements in the forward (red open circles, time-bin width 2 ns) and backward (green filled diamonds, time-bin width 5 ns) directions, and are corrected for accidental coincidences. Error bars represent Poissonian statistics. Detection times in the forward (backward) directions are offset by 879 ns (891 ns) to account for delays introduced by electrical and optical lines. Solid lines are calculated from Eq. (4.9) and (4.11) for  $\tau_p = 13.3$  ns and  $\Lambda = 0.033$ .

### Forward Direction

To obtain  $P_e(t_i)$  from the measurements in the forward direction, we numerically integrate  $\delta(t_i)$  according to Eq. (4.18). The observed evolution of  $P_e(t_i)$  share several qualitative similarities with  $\delta(t_i)$ . As before, for the decaying photon,  $P_e(t_i)$  rises from the initial ground state to a maximum value before a slow decay; for the rising photon,  $P_e(t_i)$  also rises sharply, following the exponential envelope of the probe photon, but here we observe the free decay of the excited state population after the probe photon envelope ‘ends’ at  $t_i = 0$ . Again we find good agreement with analytical solutions, given by Eq. (4.9) and (4.11) for our parameters  $\tau_p = 13.3$  ns and  $\Lambda = 0.033$ .

The observed values of  $P_e(t_i)$  are relatively modest due to the limited spatial mode overlap  $\Lambda$ ; nonetheless, consistent with the predictions of the time-reversal argument, we observe a higher peak excited state population for exponentially rising probe photons  $P_{e,\max,\uparrow} = 2.77 \pm 0.12\%$  compared to that for the decaying photons  $P_{e,\max,\downarrow} = 1.78 \pm 0.09\%$ . The measured  $P_{e,\max,\uparrow}$  is a factor of  $1.56 \pm 0.11$  larger than  $P_{e,\max,\downarrow}$ , in fair agreement with the theoretically predicted factor of 1.78.

### Backward Direction

The excited state population  $P_e(t_i)$  can also be directly determined from the atomic fluorescence measured in the backward direction, by considering the coincidence histograms  $G_b(t_i)$  between the heralding detector  $D_h$  and the backward detector  $D_b$ .

From Eq. (4.16),

$$P_e(t_i) = \frac{R_b(t_i)}{\eta_{b,\text{col}} \eta_{b,\text{det}} \Gamma_0} , \quad (4.29)$$

where  $R_b(t_i)$  is the time-dependent probability to detect a photon at  $D_b$  *per incident probe photon at the atom*. Thus to convert  $G_b(t_i)$  to  $R_b(t_i)$ , in addition to normalising to the overall heralding efficiency  $\eta_{\text{fwm}}$  (which would yield the detection probability at  $D_b$  *per detected probe photon at  $D_f$* ), we also have to account for the collection and detection efficiencies in the forward direction, i.e.

$$R_b(t_i) = \frac{G_b(t_i)}{\Delta t} \frac{\eta_{f,\text{col}} \eta_{f,\text{det}}}{\eta_{\text{fwm}}} . \quad (4.30)$$

Again, from these results we find a qualitatively different transient atomic excitation for both photon shapes, in agreement with the theoretical model. However, the detection statistics in the backward direction is much worse compared to the measurements in the forward direction, as indicated by the wider time-bins and larger error bars.

### Forward vs Backward

Our results for  $P_e(t_i)$  obtained from the measurements in the backward direction have much larger uncertainties compared to those in the forward direction. Here we discuss this discrepancy by performing some simple back-of-the-envelope comparisons.

Our spatial overlap parameter  $\Lambda \approx 0.03$  is small, thus from Eq. (4.15) we approximate  $\varepsilon \approx \Lambda$  as an order-of-magnitude estimate and use it to characterize the strength of the atom-light interaction. The backward collection efficiency  $\eta_{b,\text{col}}$  is also  $\sim \Lambda$ . Therefore the measured signal amplitude for  $N \sim 10^6$  incident probe photons is  $S_b \sim N\Lambda^2$ . For the forward direction, we consider the difference of the measurements with and without the atom, for which the signal amplitudes are approximately  $(1 - \Lambda)N$  and  $N$ , respectively, and thus  $S_f \sim N\Lambda$ . As such, the signal in the backward direction is a factor of  $\Lambda$  smaller.

However, a naive comparison of the signal amplitudes is insufficient; the essential figure of merit is the signal-to-noise ratio (SNR). Considering only Poissonian counting statistics, the characteristic noise in the backward direction is  $\Delta S_b \sim \sqrt{N\Lambda^2}$ ; in the forward direction, we consider the errors contributed by the measurements with and without the atom (for which

the signal amplitude is  $\sim N$ ), and obtain  $\Delta S_f \sim \sqrt{N}$ . Thus, in this simplified treatment, the SNR in both directions have comparable orders of magnitude:  $S_b/\Delta S_b = S_f/\Delta S_f \sim \sqrt{N}\Lambda$ .

The discrepancy between the two measurements becomes apparent only after factoring in accidental coincidences, which behave as a noise floor in the coincidence histograms. For  $G_f(t_i), G_{f,0}(t_i)$  measured in the forward direction, the accidentals offset is roughly 2 orders of magnitude lower than the peak, and does not significantly influence the SNR. In contrast, for the backward direction, the accidentals offset in  $G_b(t_i)$  is almost the same as the peak height (corrected for accidentals), i.e. the SNR is  $\sim 1$ .

Therefore, the fundamental limitation of directly measuring  $P_e(t_i)$  in the backward direction is not the smaller signal amplitude in itself, but rather the contributions from the accidental coincidences which become comparable to the signal amplitude. Nonetheless, we acknowledge the following points:

- The accidental coincidences in the backward measurements are mainly due to dark counts of detector  $D_b$ , which is  $\sim 50 \text{ s}^{-1}$ . It is difficult to obtain conventional Si APDs with significantly lower dark count rates.
- Despite the lengthy data acquisition (1500 hours), we barely have enough counts per time-bin in the backward histograms to resolve  $P_e(t_i)$  in time. Even if we completely disregard accidental coincidences, the peak of  $G_b(t_i)$  would only have  $\sim 50$  counts for a time-bin width of 5 ns. Thus, such a direct measurement would be unfeasible for similar setups and efficiencies if time is limited.

### 4.7.3 Extinction vs Decay Time

Having established that the overall extinction  $\varepsilon$  does not depend on whether the probe photon is exponentially rising or decaying, we choose to use only decaying probe photons and investigate the dependence of the extinction on the decay time  $\tau_p$ . Experimentally, we bypass the cavity setup and send the collected heralding photons straight to detector  $D_h$ . By avoiding the  $\approx 60\%$  loss of the heralding photons through the cavity setup, we significantly speed up the measurement process. We also account for the slight changes in the delay offsets during the data analysis.

The results are shown in Fig. 4.18. The methods for obtaining  $\varepsilon$  via  $\delta(t_i)$  is already presented in §4.7.1. As before, we use  $T_c \approx -\tau_p \leq t_i \leq 7.5\tau_p$ , and scale the coincidence windows accordingly for different  $\tau_p$  values.

We observe a decrease in the extinction  $\varepsilon$  for smaller  $\tau_p$  due to an increase in the bandwidth mismatch between the probe photon and the natural linewidth of the probe

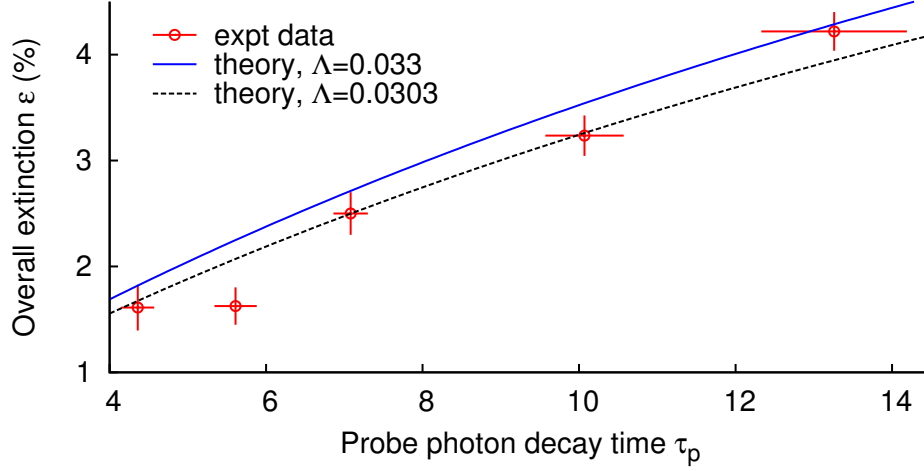


**Figure 4.18:** Overall extinction values for exponentially decaying probe photons of different decay times  $\tau_p$ . Vertical error bars represent Poissonian statistics, while horizontal error bars reflect the standard deviation in the distribution of the measured  $\tau_p$  values. Black dashed line represents a fit to Eq. (4.15), which yields  $\Lambda = 0.0303$ . Blue solid line represents Eq. (4.15) calculated with  $\Lambda = 0.033$ , which best describes the observations for  $\tau_p = 13.3$  ns presented in previous sections.

transition. A fit of our data to Eq. (4.15) yields  $\Lambda = 0.0303$ , which is slightly different to the value of  $\Lambda = 0.033$  that best describes the observations for  $\tau_p = 13.3$  ns presented in previous sections. Despite this discrepancy, our results still show very good agreement with the theoretical model (except for an outlying point at  $\tau_p = 5.6$  ns).

## 4.8 Conclusion

We have observed the time-resolved scattering of single photons by a single atom, using photons of exponentially rising and decaying temporal profiles. Although the two photon shapes have identical power spectra, they display different transient atomic excitations. As predicted by the time-reversal argument, we measure a higher peak excited state population of  $P_{e,\max,\uparrow} = 2.77 \pm 0.12\%$  for the rising photon, which is a factor of  $1.56 \pm 0.11$  higher compared to that for the decaying photon  $P_{e,\max,\downarrow} = 1.78 \pm 0.09\%$ .

Although we observe a dependence of the overall extinction on the probe photon bandwidth, the extinctions for both photon shapes with the same decay time are very similar:  $4.21 \pm 0.18\%$  and  $4.40 \pm 0.20\%$  for decaying and rising photons, respectively.

Our results demonstrate the precise control of the atom-photon interaction by tailoring the temporal envelope of the single photons. By using exponentially rising photons over the decaying ones, we achieve a higher excitation probability at well-defined instants in time. Combined with a better synchronization of the excitation process, this can be applied to the design and implementation of more efficient quantum networks.

# Chapter 5

## Conclusion & Outlook

We have experimentally demonstrated the interfacing of a single atom with single photons. Two main approaches are presented: indirect interaction via Hong-Ou-Mandel (HOM) interference, and direct scattering of the single photons by the atom. We measure a HOM interference visibility of  $62 \pm 4\%$  (without accidental corrections) and  $93 \pm 6\%$  (with accidental corrections); for the scattering experiment, we observe a peak excitation of  $2.77 \pm 0.12\%$  for exponentially rising probe photons, which is a factor of  $1.56 \pm 0.11$  higher than the value of  $1.78 \pm 0.09\%$  for the exponentially decaying photon.

Here, let us take stock of our results and do a reality check: where does our atom-photon interface stand within the larger context of the ‘quantum internet’ laid out at the start of this thesis? Although we have demonstrated substantial atom-light interaction in our experiments, the efficiency of the interface is still rather modest. Besides, beyond developing building blocks for a quantum network, we have to move towards connecting multiple nodes of the network and implementing practical quantum information protocols (by only exciting the cycling transition of the atom, we have not actually performed any quantum information transfer between the atom and the single photons).

In response to these challenges, our research group is actively pursuing new developments in several areas, with some preliminary progress already being made as this manuscript is prepared.

### Improving the Single Atom System

To increase the atom-light interaction strength, an obvious improvement would be to focus the light more strongly using lenses with a higher numerical aperture (NA). Currently, we have built a separate free-space trap for single  $^{87}\text{Rb}$  atoms using an aspheric lens pair with

NA = 0.75 (compared to the current NA = 0.55), and measured an extinction of up to  $\sim 18\%$  for a weak coherent field (compared to  $\sim 10\%$  with this setup). Further characterization and optimization is ongoing.

It is also worth considering how the free-space single-atom system can continue to be improved in the long term. We can already identify several issues if we continue to pursue higher NA lenses.

- The effect of the atomic motion becomes more significant with greater focusing [1]. As such, to improve the atom-light coupling, we may need to improve the molasses cooling, or employ additional cooling techniques such as Raman sideband cooling [68, 144] to bring the atom to the vibrational ground state of the trap. However, performing Raman cooling is difficult with a circularly-polarized dipole trap, which our experiments require (see §2.1.3); a circularly-polarized trap leads to spatially inhomogeneous AC Stark shifts, which cause decoherence that hinders the cooling process.
- An increased NA also restricts the optical access for the vertical MOT beams, and it may eventually become unfeasible to create the MOT between the aspheric lenses. It is possible to trap the atom cloud above the lenses, and transport the atom cloud to the dipole trap via free-fall [145] or with an additional transport beam [146], but doing so would greatly complicate the setup.
- For an aspheric lens, the effective focal lengths for the probe and dipole trap wavelengths are different; to overlap the foci of the two beams in the current setup, the incident dipole trap beam is not collimated but slightly converging, which results in a larger focal spot with a lower trap depth (for the same dipole trap beam power). This effect is more severe for NA = 0.75, and ironically we would require a larger optical power to obtain the same trap depth in the new setup despite the higher NA. We circumvent this issue in the new setup by using 850 nm instead of 980 nm as the dipole trap wavelength (which makes the trap less far-off-resonant), but adopting a similar trap geometry for even higher NA lenses might not be trivial for simple aspheric lenses.

Nonetheless, we are optimistic that the solutions to these issues will become more apparent as we understand the new setup better.

Another possible approach would be to split the single photon (at a 50:50 beam-splitter) and focus it onto the atom using both aspheric lenses. It might seem counter-intuitive that splitting up a photon leads to increased interaction, but if the light fields approaching the

atom from both lenses interfere constructively, the spatial overlap is doubled compared to using only one lens.

A more radical idea aims to obtain (almost) full spatial overlap in free space with a deep parabolic mirror, which has so far been used with trapped single ions [147, 148]. If this geometry could be successfully adapted to trap a single neutral atom, we can achieve (near-)perfect single-photon excitation of the single atom.

### **Increasing Single-Photon Generation Efficiency**

We can increase the generation rate of the four-wave mixing (FWM) photon source by increasing the optical density (OD) of the atom cloud, but doing so would also decrease the decay time of the heralded single photon, and increase the bandwidth mismatch with the cycling transition of the atom. The atom cloud in the FWM setup is (more-or-less) spherical, thus increasing the OD, which is a function of the total number of atoms in the path of the pump beams, by using a larger quadrupole magnetic field gradient would also result in a larger atomic spatial density.

Suppose the photon bandwidth is actually only dependent on the atomic density (spacing between atoms) but not the OD (overall number of atoms): if so, then by using an elongated atom cloud and sending the pump beams along the elongated axis, we can achieve a larger OD for the same atomic density, i.e. for the same photon decay time, the elongated cloud would have a higher photon pair rate compared to the spherical cloud.

We have produced an elongated atom cloud by using a pair of racetrack coils to generate the quadrupole field, and are currently working on preparing the system to perform FWM.

### **Scaling Up**

With the FWM setup, we can obtain single photons by heralding on one photon of a photon pair. We are also modifying the FWM setup to produce heralded photon pairs via six-wave mixing, with which we can potentially entangle two separate single-atom qubits.

As our photon source is an atomic system also based on  $^{87}\text{Rb}$ , we can conveniently generate single photons with compatible properties for efficient interaction with a single  $^{87}\text{Rb}$  atom. Moving forward, it would also be interesting to demonstrate the efficient interfacing of the single atom with a more diverse range of quantum systems. The ability to realize quantum networks composed of different physical systems would allow us to fully harness the capabilities of each, and move towards implementing practical quantum information protocols on a larger scale.

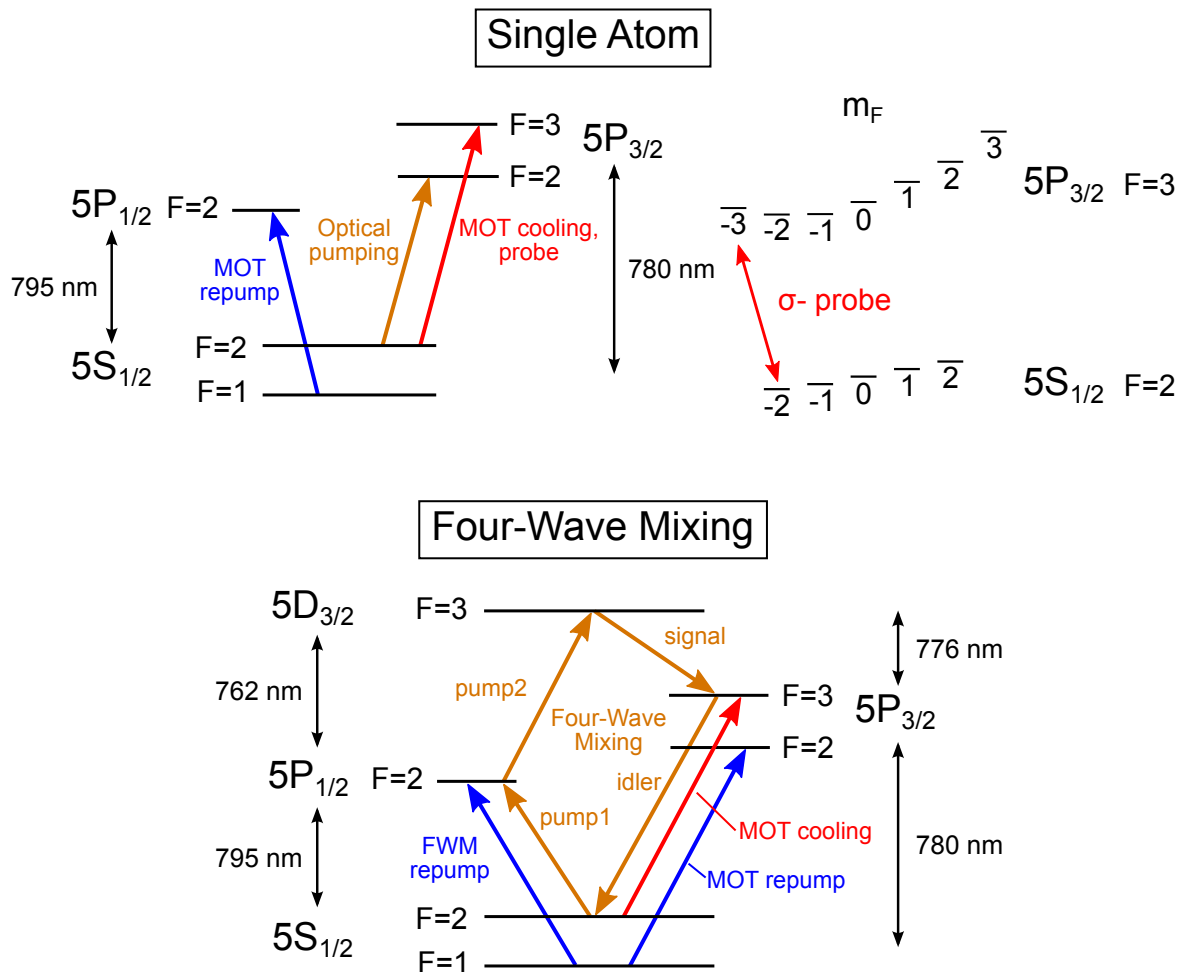


# Appendix A

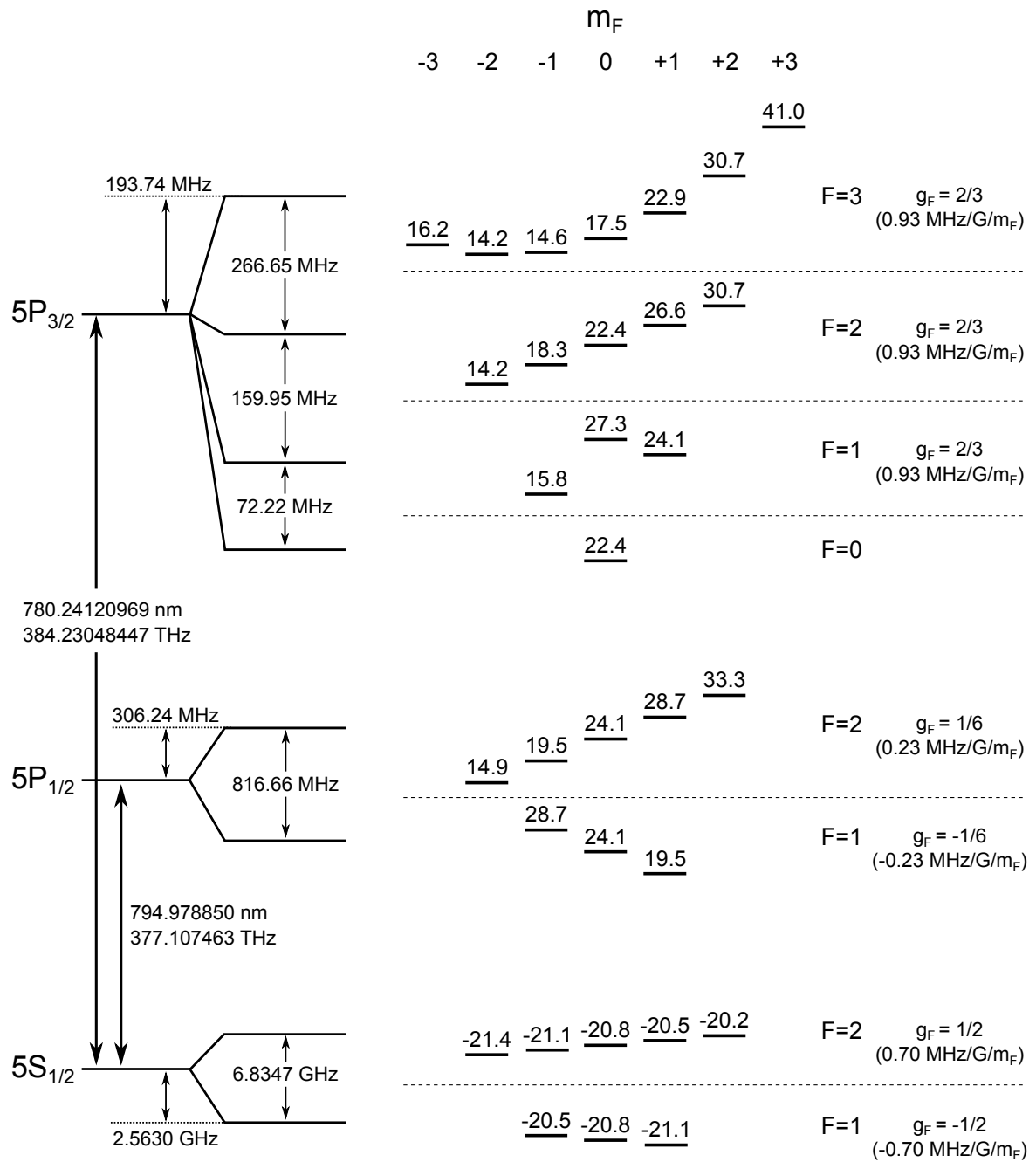
## Energy Levels of $^{87}\text{Rb}$

Fig. A.1 shows all transitions of  $^{87}\text{Rb}$  used in the single atom and four-wave mixing (FWM) systems. Fig. A.2 shows the D1 and D2 transition lines in greater detail, including the hyperfine and Zeeman manifolds, as well as calculated values for the AC Stark shifts.

The calculations have been outlined in the appendix of [1], and require the lifetimes (or, equivalently, the oscillator strengths) of the numerous transitions in  $^{87}\text{Rb}$ . Ref. [149] contains theoretical calculations for many of the values we require in one single, consistent source; for the remainder, we refer to the NIST database values [150] if they exist, or try to make intelligent estimates, as described in [1]. We also found a more complete database in Ref. [151], but the predictions made with those values show large discrepancies with the measurement results.



**Figure A.1:** Transitions of  $^{87}\text{Rb}$  used in the single atom and four-wave mixing (FWM) systems.



**Figure A.2:** Energy levels of the  $^{87}\text{Rb}$  atom for the D1 and D2 lines, showing the hyperfine and Zeeman manifolds. The number above each  $m_F$  level is the calculated AC Stark shift, in MHz, per mK of dipole trap depth; the AC Stark shift scales linearly with the trap depth. For each hyperfine level, we also state the approximate Landé  $g$ -factor and the Zeeman shift per Gauss per  $m_F$ . Other values are taken from [5].



# Appendix B

## Alignment Procedure

For the single atom setup, careful alignment of multiple beam paths is required to generate a stable MOT, load the optical dipole trap, and optimize the coupling of the single atom to the tightly focused probe and collection modes. Although the demands on the alignment precision and stability may not as stringent as compared to cavity-based setups, we have nonetheless established a systematic procedure to align the MOT beams, MOT quadrupole magnetic field, dipole trap, and probe/collection modes with respect to each other. When properly aligned, the setup is typically stable for months, and does not require active stabilization or frequent re-alignment (barring a catastrophic bump against the optical table).

This chapter presents the alignment procedure for the ‘basic’ single atom setup shown in Fig. 2.1.

We omit a separate detailed description for the FWM setup: very briefly, the principles of the MOT alignment are similar, except that we work with much larger beams (diameter  $\approx 15$  mm). The alignment of the pump and signal/idler collection modes is simplified by the collinear geometry and optimized on the photon pair rate and efficiency.

### B.1 Probe, Collection, Dipole Trap

#### Probe Beam

When starting from scratch, the first task is to align the 780 nm probe beam. This establishes a useful reference as the beam path within the vacuum chamber is easily visible via atomic fluorescence (as opposed to the 980 nm dipole trap), and also pinpoints the desired location of the trapped atom.

For optimal coupling between the trapped atom and the probe mode, the foci of the probe and dipole trap beams must coincide. The naive approach would be to collimate both beams and send them through the lenses; if the back planes of the lens pair are separated by exactly twice the working distance ( $2 \times 2.91$  mm), then the output beams should also be collimated, with the focus at the midpoint between the lenses.

However, possible lens defects/aberrations and limited precision in both the machining of the lens holder and in mounting the lens pair meant that this scenario might not necessarily be the case at the lens design wavelength of 780 nm. Besides, the aspheric lens has a focal length shift of  $\sim 50$   $\mu\text{m}$  between the two wavelengths. As such, simply sending in collimated beams at both 780 nm and 980 nm would not lead to overlapping foci.

Instead, we rely on symmetry: we adjust the beam divergences such that their propagation profiles are symmetric outside the vacuum chamber on either side of the confocal aspheric lens pair; we then conclude that the beam profile between the lenses is also symmetric, with the focus at the midpoint of both lenses. This would apply for both wavelengths. We note that the beam waist of either beam at the focus depends on the divergence of the incident beam.

As such, we align the probe beam such that it propagates in a straight line through the lens pair, aided by infrared camera images of the atomic fluorescence within the chamber (the probe beam has to be tuned on resonance), and adjust the beam divergence until we obtain the desired symmetry. The beam radii measured at 13 cm and 30 cm from the midpoint between the lenses are 1.21 mm and 1.19 mm, respectively, on both sides of the vacuum chamber.

### **Collection Modes**

After propagating through the lens pair, the aligned probe beam is coupled into a single-mode fiber: this serves as a rough alignment for the forward collection mode (transmission). Light is then sent backwards through the forward collection fiber and coupled into another single-mode fiber in the backward collection mode (reflection).

### **Dipole Trap**

Similar to the probe beam, we rely on symmetry to set the divergence of the dipole trap beam. The beam radii measured at 13 cm and 30 cm from the midpoint between the lenses are 1.19 mm and 1.39 mm, respectively, on both sides of the vacuum chamber.

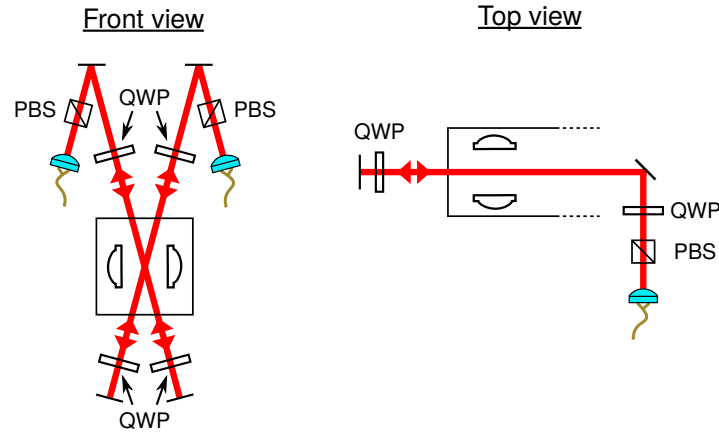


**Figure B.1:** Simplified sketch of the MOT beams. **(Left)** Front view of the cuvette, showing the vertical MOT beams. **(Right)** Top view, showing the horizontal MOT beams. PBS: polarizing beam-splitter, QWP: quarter-wave plate.

The overlap of the dipole trap and probe beams is achieved imaging the beams with a camera in the ‘near-field’ (few cm before the cuvette) and ‘far-field’ (projected onto the wall on the far side of the lab,  $\approx 7$  m away), and adjusting the alignment till the center of the beam profiles coincide at both the near- and far-field.

## B.2 Magneto-Optical Trap (MOT)

The goal is to align the MOT so as to trap a cloud of cold  $^{87}\text{Rb}$  atoms, centered at the focus of the aspheric lens pair. A simplified sketch of the MOT beams is shown in Fig. B.1.

### B.2.1 Preparing the MOT Beams

Before aligning the beams, there are several considerations:

#### Angles

We want to trap the atom cloud between the lenses to coincide with the position of the trapped atom at the focus of the aspheric lens pair, but the simplest geometry of having 3 orthogonal beam pairs is impossible as the MOT beams cannot go through the aspheric lenses. The size of the atom cloud depends on the intersection volume of the 3 beam pairs; with strongly focusing beams, the generated atom cloud (if at all possible) will be too small.

As such, the horizontal MOT beam travels along the length of the cuvette, while the vertical MOT beams have enter through the gap in the lens holder (see Fig. 2.2), and are limited to a maximum of  $\sim 20^\circ$  from the vertical axis.

### Size and Divergence

Instead of 6 individual beams, we use 3 beams and retro-reflect them to obtain the required beam geometry. However, the retro-reflected beams have a lower power due to additional losses from passing through the inner uncoated cuvette surface twice. To ensure that the incident and retro-reflected beams have equal intensities at the position of the MOT, they are made to be slightly focusing; the required beam parameters are calculated from the optical path lengths and the cuvette losses ( $\approx 9\%$  for two passes). The spatial mode of the beams are defined by single-mode fibers and their divergences are adjusted with an aspheric lens (Thorlabs A375TM-B), with radii of  $\approx 0.6$  mm at the position of the MOT.

### Polarization

The circular polarization of each MOT beam must have the same handedness (with respect to the direction of beam propagation) as its retro-reflected pair. The correct handedness depends on the polarity of the current in the quadrupole field coils, and can be easily verified by swapping the latter; only the correct polarity will lead to an atom cloud being trapped.

To generate circularly polarized beams, a PBS after the fiber cleans up the polarization, and a QWP sets the circular polarization. After passing through the cuvette, a second QWP converts the circular polarization to linear; the retro-reflected beam is then converted back to having a circular polarization of the same handedness by the second QWP. As such, the second QWP needs no alignment with respect to the beam.

We note that the required handedness of the horizontal beam, which travels along the axis of the quadrupole field coils, is the opposite of the other two beams.

### Power

The MOT cooling beam powers are typically maintained at about  $150 \mu\text{W}$  for each vertical beam and  $130 \mu\text{W}$  for the horizontal beam. The total repump power in the horizontal and two vertical beams is  $\simeq 150 \mu\text{W}$ ; the distribution of repump power across the beams is not important. Due to instabilities in the laser output and beam polarizations, the MOT beam powers suffer drifts of  $\sim 10\%$ . However, this is not deemed to affect single atom loading rates significantly, and thus a power lock was not implemented.

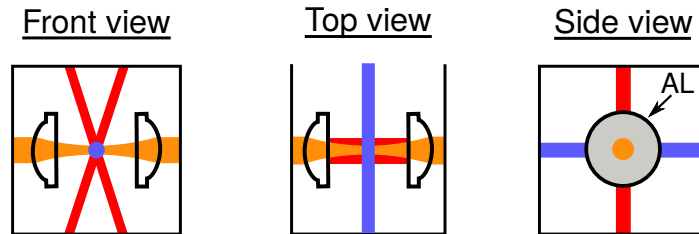


**Figure B.2:** Sketch of the beam paths marked by atomic fluorescence, as seen on the IR camera images. Orange, red, and blue lines represent the probe beam, vertical MOT beams and horizontal MOT beam, respectively. For the side view, the camera is aligned to a weak probe beam sent through the aspheric lens (AL). When the MOT beam passes through the focus of the AL, the fluorescence fills the lens homogeneously.

## B.2.2 Aligning the MOT

### Magnetic Fields

The first step is to align the magnetic field coil holder, on which we mount a pair of anti-Helmholtz coils to generate the quadrupole field, as well as three sets of Helmholtz coils to compensate for stray magnetic fields. The coil holder is maneuvered in place via a 3-axis micrometer stage such that it is centered at the dipole trap focus.

Next, we want to zero the magnetic field at the center of trap. Any stray magnetic fields will displace the magnetic field minimum and hence the position of the MOT. Since we cannot physically access the interior of the vacuum chamber with a magnetic field probe, we measure the field along each axis on both sides of the chamber, and adjust the compensation coil currents until we measure equal magnitudes but in opposite directions; we then infer that the field at the center is close to zero.

### MOT Beams

The initial goal is to have all 3 beams (without retro-reflection) intersect with the focus of the probe beam, which serves as our reference. We run the dispenser at a high current and tune the beams on resonance with an atomic transition. The beam paths are then marked by atomic fluorescence and imaged by infra-red (IR) cameras (see Fig. B.2). After these beams are aligned, they are retro-reflected and coupled back into the fiber.

### Hunting for the Atom Cloud

Now we want to try to see the atom cloud trapped by the MOT on the IR camera. We turn off the probe beam and lower the dispenser current to its typical value (or slightly above). The

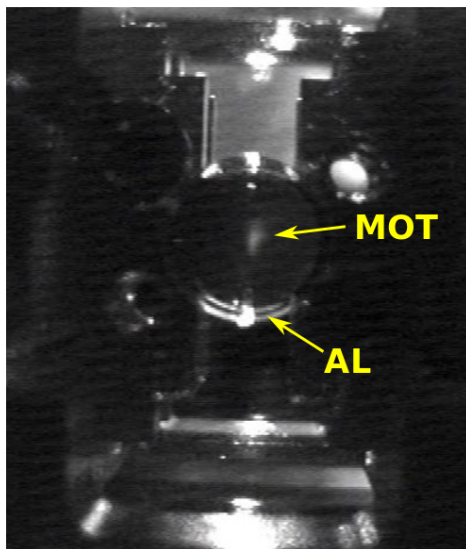


**Figure B.3:** IR camera image of the side view of the cuvette, showing a small cloud of cold atoms (labelled MOT) through the aspheric lens (AL). The alignment has yet to be optimized for obtaining a bright and stable atom cloud.

cooling beam is slightly red-detuned ( $1-2\Gamma_0$ ) and the quadrupole coil current is increased from the typical operating value ( $\sim 1.1\text{ A} \rightarrow 1.5\text{ A}$ ); a smaller cooling beam detuning and having a higher quadrupole field should produce a brighter, denser atom cloud which is more clearly visible.

With luck, the atom cloud will appear, but if not, tweaking the beam alignments and/or the position of the quadrupole field coils slightly should produce small flickers of fluorescence that hint at an existence of a trapped atom cloud (see Fig. B.3).

Once the atom cloud is visible, we continue to optimize the beam and quadrupole field alignments using the criteria of brightness, stability, and position (the atom cloud should remain centered at the focus of the aspheric lens pair). We note that at the optimal beam alignment, the retro-reflected MOT beams are not necessarily well-coupled back into the fiber.

### B.3 Trapping the Single atom

With a stable MOT, we return to our typical operating parameters: the cooling beam red-detuning is increased to  $\sim 4\Gamma_0$  and the quadrupole coil current decreased to  $\sim 1.1\text{ A}$ . We should be able to load single atoms into the trap and observe the fluorescence of the trapped atom in both forward and backward collection modes. We then adjust our operating parame-

---

ters and beam alignments in order to maximize the collected fluorescence signal, loading rate, and the lifetime of the atom in the trap. We typically detect  $\sim 7000$  photons per second of fluorescence from the MOT beams in each collection arm. The probe beam alignment also has to be optimized on the signal from the atom itself, usually by measuring the transmission of a weak coherent field (see §4.5.4).



# Appendix C

## Timestamp Correction

The nominal 125 ps resolution of the timestamp unit is achieved by multiplying a 10 MHz input reference from the rubidium clock to a 500 MHz clock signal (2 ns period), which is further subdivided into 16 “bins” via a phase interpolation stage, i.e. these bins provide the high-resolution timing information within each 2 ns clock cycle. However, the subdivision is not strictly uniform, and this results in a small oscillation of period 2 ns on top of the expected signal in our coincidence measurements.

To characterize this effect, we perform an autocorrelation measurement of a random source (see Fig. C.1). Instead of a flat line, the coincidence histogram shows spikes with a periodicity of 2 ns, reflecting the tendency for input signals to be erroneously concentrated into certain bins. This can also be seen by directly analyzing the distribution of recorded counts in each bin (see Fig. C.2).

Using this distribution, we can correct for this error by probabilistically redistributing each recorded timestamp among the neighbouring bins. The correction provides the uniform bin distribution as expected, at the expense of an increase in the timing uncertainty of each timestamp. This timestamp correction is only performed for coincidence measurements in the scattering experiment (Chapter 4).

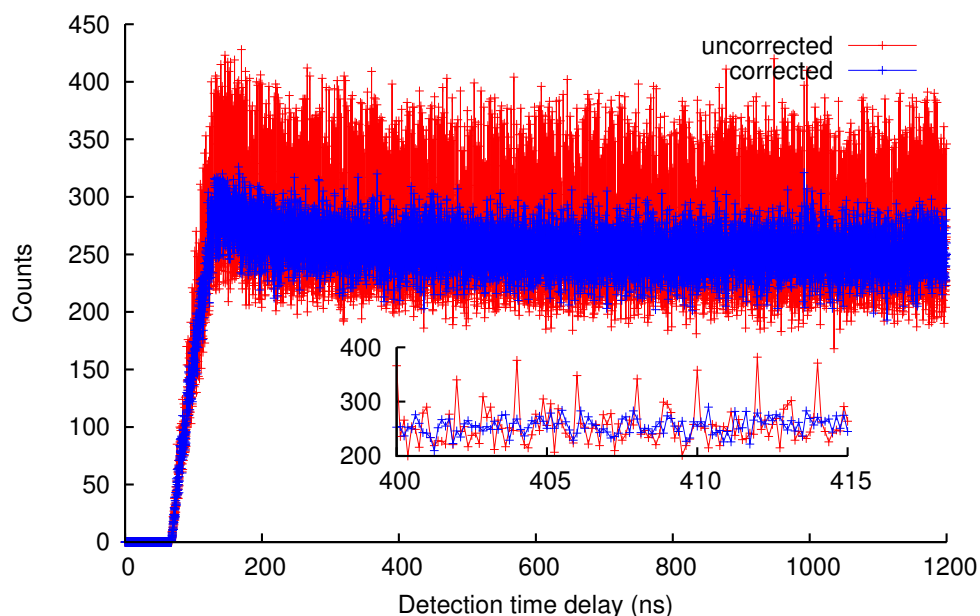


**Figure C.1:** Autocorrelation histogram of recorded timestamp signals from an APD, with a random light source (a fluorescent lamp) as the input. The results with and without correcting for unequal timestamp bins are shown. The inset displays a portion of the same data at a finer time resolution. For a random input, the measured counts should be uniform across all detection time delays; the uncorrected version shows periodic peaks every 2 ns, a consequence of the bins being unequal. The corrected version shows a more uniform distribution and a smaller spread in counts. The rising slope during the first 200 ns is due to the timestamp dead time. The time bin width is 125 ps, which is the nominal resolution of the timestamp unit.

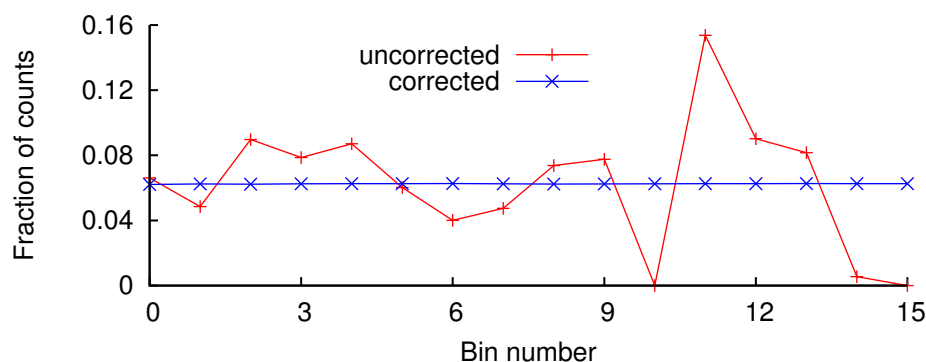


**Figure C.2:** Distribution of recorded counts from Fig. C.1 across the 16 timestamp “bins”, with and without correction. The correction provides a uniform distribution, as expected for a random input.

# Appendix D

## Calibrating APD Efficiencies

Here we describe the calibration of the avalanche photodetectors (APDs). To obtain an absolute measurement of the APD detection efficiency, we require a reliable reference; in our case, we use a photodiode (Hamamatsu S5107) which has been calibrated by the National Metrology Centre, Singapore.

The calibration setup is shown in Fig. D.1. An 810 nm laser enters the setup via a single-mode fiber and is split at a 50:50 beam-splitter; one output arm goes to a fixed photodiode (also Hamamatsu S5107), while the other arm is attenuated by a stack of 6 neutral density filters (NDFs), coupled to a multi-mode fiber, and sent to the test device.

We first set the calibrated photodiode as the test device, remove the NDFs, and measure the photocurrents of both photodiodes using separate Agilent 34401A 6½-digit multimeters. From the calibration data, we obtain

$$R = \frac{P_{\text{in}}}{I_f}, \quad (\text{D.1})$$

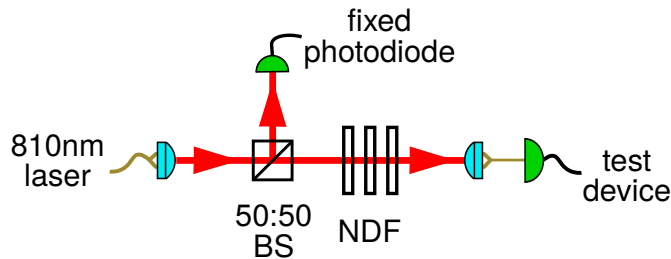


**Figure D.1:** Schematic of the APD calibration setup. The 810 nm input laser is split at a 50:50 beam-splitter (BS); one output arm goes to a fixed photodiode, while the other is attenuated by a stack of 6 neutral density filters (NDF) before being sent to the APD being tested. To avoid etalon effects, the NDFs are slightly tilted with respect to the beam.

where  $P_{\text{in}}$  is the optical power collected into the multi-mode fiber, and  $I_f$  is the photocurrent of the fixed photodiode. The quantity  $R$  now serves as the calibration reference, and is expected to stay constant throughout the measurements.

Next, we calibrate the NDFs one by one by placing them between the beam-splitter and the output fiber coupler, and measuring its transmission with the calibrated photodiode. The measurement is done one by one as the dynamic range of the photodiode is not wide enough to measure the combined optical density of  $D \approx 10$ . To avoid etalon effects, the NDFs are slightly tilted with respect to the beam, and we additionally verify that the insertion of the NDFs into the beam path does not significantly affect the coupling of light into output multi-mode fiber.

We then insert all the NDFs, and replace the calibrated photodiode with the APDs as the test device. The laser power is adjusted such that the measured APD count rate is  $\sim 5 \cdot 10^4 \text{ s}^{-1}$ , which is low enough to avoid APD saturation effects. For a single measurement, we count the number of APD clicks in 1 s, and simultaneously record the photocurrent of the fixed photodiode  $I_f$ . We perform 200 such measurements, then repeat the same number without any input light to measure the APD dark count rate. The APD efficiency is then the ratio of the detected and input powers, calculated via

$$\text{Efficiency} = \frac{P_{\text{det}}}{P_{\text{in}}} = \frac{(\langle N \rangle - \langle N_d \rangle) \cdot (h \cdot c / \lambda)}{I_f \cdot R \cdot 10^{-D}}, \quad (\text{D.2})$$

where  $\langle N \rangle$ ,  $\langle N_d \rangle$  are the average APD count rate and dark count rate, respectively,  $h$  is the Planck constant,  $c$  is the speed of light, and  $\lambda = 810 \text{ nm}$  is the wavelength of the input light.

Although the APDs are used to measure light at 780 nm in our experiments instead of 810 nm, we assume that the APD efficiency does not differ significantly between the two wavelengths, and that the calibration values are still valid.

# Appendix E

## Ratio of Means vs Mean of Ratios

Here we consider the calculation of the extinction  $\varepsilon$ , or equivalently the transmission ratio  $T = 1 - \varepsilon$ , and discuss two possible methods for obtaining this value from our data. We first provide a mathematical description of the two methods, and justify the choice in our data analysis (as shown in §4.7.1).

### Ratio Estimators

Consider two variables  $X$  and  $Y$ , for which we measure multiple pairs of values  $x_i$  and  $y_i$ . We are interested in the ratio  $Y/X$ , which can be estimated from our data via *ratio estimators*, two of which are the ‘ratio of means’:

$$R_1 = \frac{\sum_i y_i}{\sum_i x_i}, \quad (\text{E.1})$$

and the ‘mean of ratios’:

$$R_2 = \sum_i \frac{y_i}{x_i}. \quad (\text{E.2})$$

The two estimators are not equivalent; for a sample size of  $n = 2$ , we see that  $\frac{y_1+y_2}{x_1+x_2}$  and  $(\frac{y_1}{x_1} + \frac{y_2}{x_2})$  are not necessarily equal. Though we might naively assume that the difference is negligible as long as there are sufficient statistics, sampling theory shows that *both* estimators are biased [152–154]. The bias of  $R_1$  asymptotically approaches 0 as  $n \rightarrow \infty$ , while that of  $R_2$  converges to a non-zero value which cannot be trivially corrected for [152]. Thus  $R_2$  is an ‘inconsistent’ estimator, and  $R_1$  would typically have a smaller bias; this has also been observed in empirical statistical tests [154, 155].

We note that it is possible to construct unbiased estimators, but we choose not to do so as it would greatly complicate the data analysis.

### Simple Simulations

The bias can be illustrated with a simple numerical simulation. We define  $X$  and  $Y$  as independent normal distributions with a mean of 1 and standard deviation of 0.1. For a sample size of  $10^6$ , we find  $R_1 \sim 1 \pm 10^{-4}$  while  $R_2 \sim 1 + 10^{-2} \pm 10^{-4}$ ; the positive bias in  $R_2$  does not decrease even if we increase the sample size.

Interestingly, if the values of  $x_i$  and  $y_i$  are strongly correlated within each pair  $i$ , the bias in  $R_2$  seemingly becomes negligible. For instance, if we set  $y_i = A_i x_i + B_i$ , where  $A_i, B_i$  are normally distributed with means of 1, 0 and standard deviations of 0.1, 0.1, both  $R_1$  and  $R_2$  produce similar values of  $\sim 1 \pm 10^{-4}$ .

### Calculating the Transmission Ratio

For the scattering experiment, we obtain the transmission ratio from the overall coincidence histograms via the ratio of means:

$$T_1 = \frac{\sum_{T_c} G_f(t_i)}{\sum_{T_c} G_{f,0}(t_i)}. \quad (\text{E.3})$$

Alternatively, we could also use the mean of ratios to calculate  $T$ :

$$T_2 = \frac{1}{n_k} \sum_k T_k = \frac{1}{n_k} \sum_k \left( \frac{\sum_{T_c} G_{f,k}(t_i)}{\sum_{T_c} G_{f,0,k}(t_i)} \right), \quad (\text{E.4})$$

where  $k$  is now a measurement consisting of 100 atom trapping events, and  $n_k$  is the number of sets of 100 atoms. The choice of 100 atoms per set is motivated by there being sufficient photon counts within each set to obtain a sensible value for  $T_k$ ; during the experiment, we also monitor the FWM rates and efficiencies using data accumulated over every 100 atom trapping events (see §4.6.3).

From our data, we find that the extinction  $\varepsilon_2 = 1 - T_2$  is consistently smaller than  $\varepsilon_1$  by  $\sim 10\%$ ; this difference is larger than the relative error of  $\sim 5\%$  in the extinction values.

We rule out drifting experimental parameters as a source of potential bias leading to the difference between  $\varepsilon_1$  and  $\varepsilon_2$ . As the coincidence histograms  $G_f$  and  $G_{f,0}$  are normalized to the number of heralding events, the ratio  $(\sum_{T_c} G_f(t_i))/(\sum_{T_c} G_{f,0}(t_i))$  is not biased by drifts in the heralding rate. Via numerical simulations on our data, we also verify that drifts in the heralding efficiency (using the distribution of measured efficiencies shown in Fig. 4.9) do not significantly bias the end result.

As such, we attribute the discrepancy between  $\varepsilon_1$  and  $\varepsilon_2$  to the inherent bias in the mean of ratios. Thus we present  $\varepsilon_1$ , calculated with the ratio of means, as our experimental result. The additional advantage is that  $\varepsilon_1$  is obtained directly from the overall coincidence histograms, which is consistent with what we use to analyse the scattering dynamics and excitation probability in §4.7.



# Appendix F

## Setup Photographs

Here we include a selection of photographs of the setups.

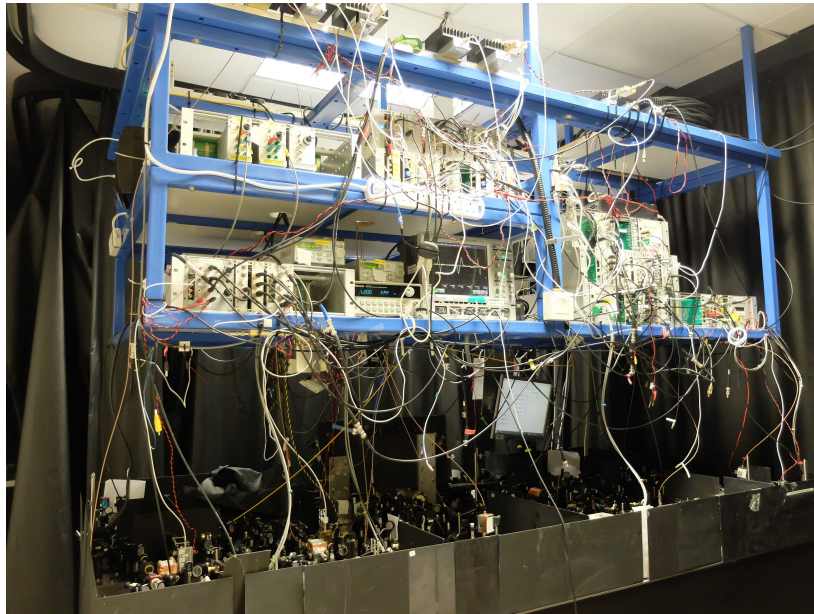


**Figure F.1:** The single atom setup.

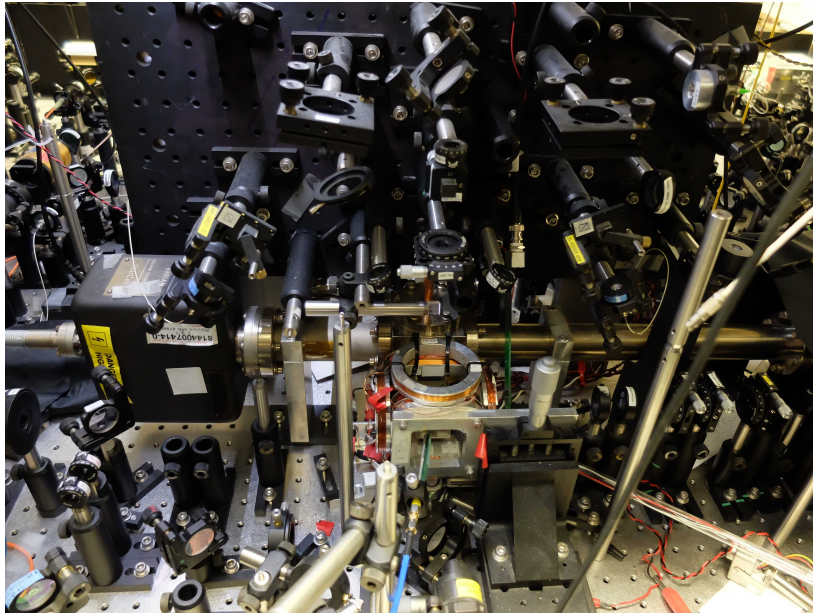


**Figure F.2:** Vacuum chamber, cuvette (within the magnetic field coil structure), and surrounding optics of the single atom setup.

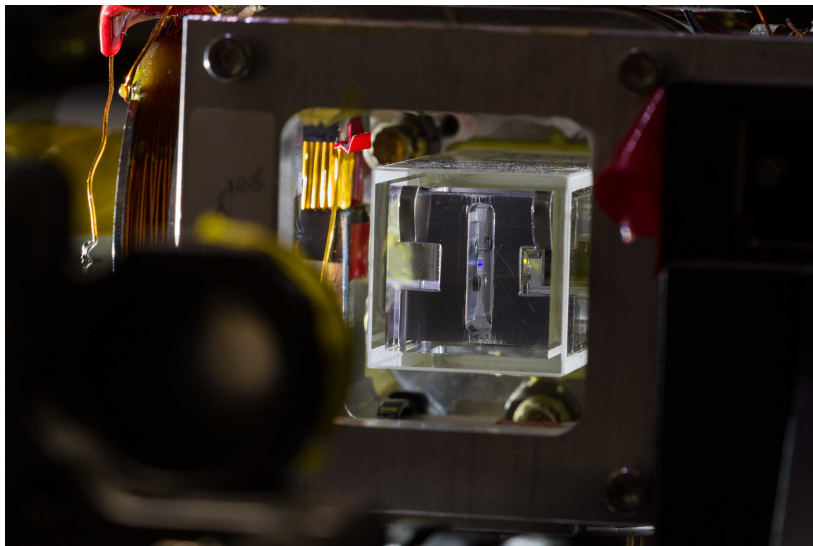


**Figure F.3:** Close-up of the cuvette at the single atom setup. Photo credit: Alessandro Cerè.

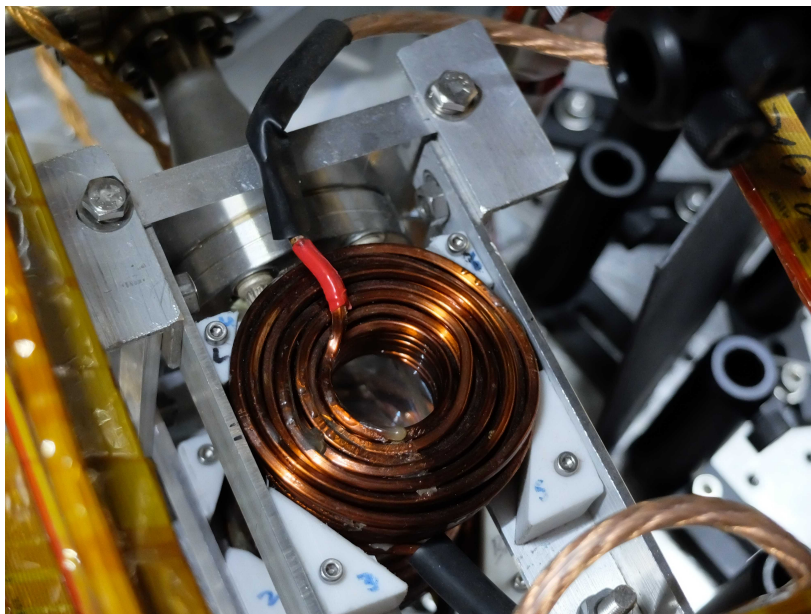


**Figure E.4:** Close-up of the cuvette at the FWM setup, showing the quadrupole field coils.

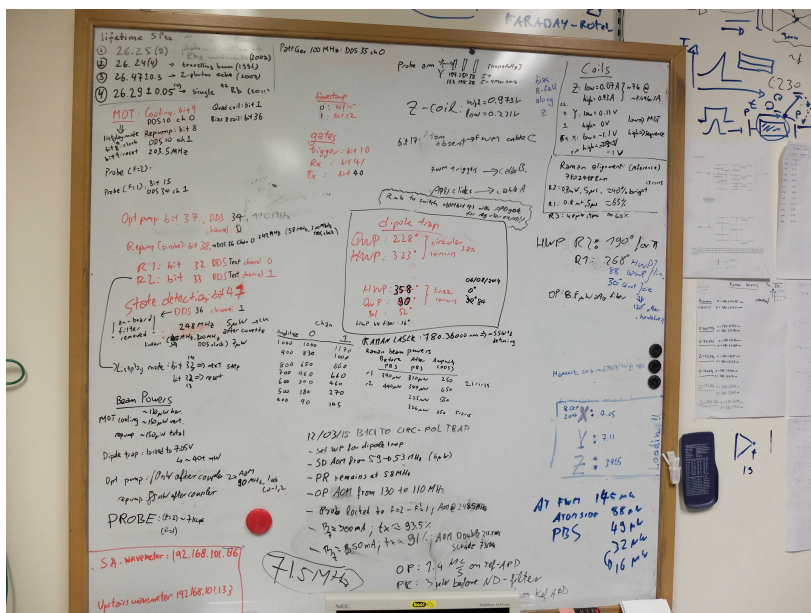


**Figure E.5:** The master record of all our experimental parameters.

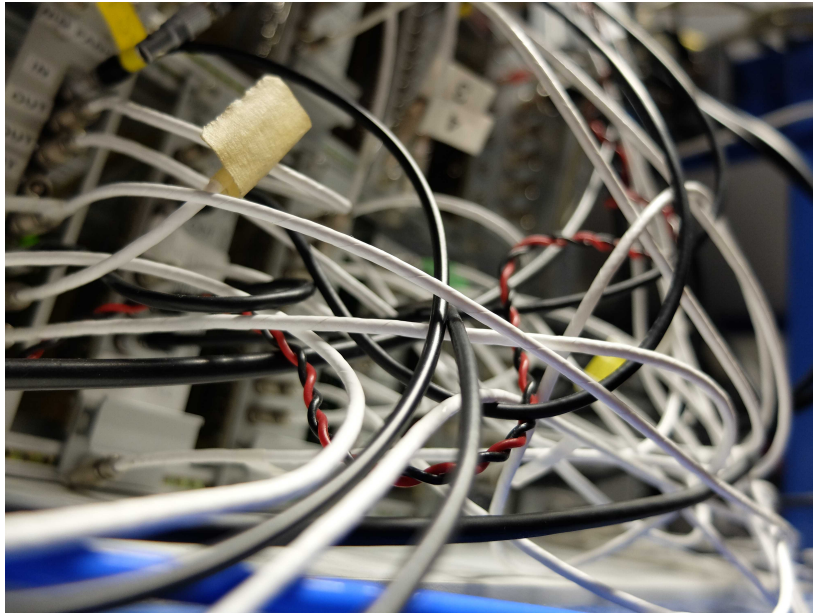


**Figure F.6:** Entanglement of wires is much easier than the entanglement of qubits...



**Figure F.7:** Precision alignment required...

# References

- [1] M. K. Tey. *Interfacing light and a single quantum system with a lens*. PhD thesis, National University of Singapore, (2009). URL <http://www.qolah.org/publications.html#theses>.
- [2] B. Srivathsan. *Heralded single photons for efficient interaction with single atoms*. PhD thesis, National University of Singapore, (2015). URL <http://www.qolah.org/publications.html#theses>.
- [3] Z. J. Lim. *Characterisation of Single Photon Avalanche Detectors*. Undergraduate Final Year Project Thesis, National University of Singapore, (2016).
- [4] Wikimedia Commons. Photons displaying the hong-ou-mandel effect. URL [https://en.wikipedia.org/wiki/File:Photons\\_displaying\\_the\\_Hong-Ou-Mandel\\_effect.png](https://en.wikipedia.org/wiki/File:Photons_displaying_the_Hong-Ou-Mandel_effect.png). Accessed 2016-04-05.
- [5] D. Steck. Rubidium 87 d line data. URL <http://steck.us/alkalidata/rubidium87numbers.pdf>. Accessed 2016-03-24.
- [6] P. W. Shor. Polynomial-time algorithms for prime factorization and discrete logarithms on a quantum computer. *SIAM review* **41**, 303 (1999).
- [7] E. Waks, K. Inoue, C. Santori, D. Fattal, J. Vuckovic, G. S. Solomon, and Y. Yamamoto. Secure communication: Quantum cryptography with a photon turnstile. *Nature* **420**, 762 (2002).
- [8] V. Giovannetti, S. Lloyd, and L. Maccone. Quantum-enhanced measurements: beating the standard quantum limit. *Science* **306**, 1330 (2004).
- [9] R. P. Feynman. Simulating physics with computers. *International journal of theoretical physics* **21**, 467 (1982).
- [10] D. Wecker, B. Bauer, B. K. Clark, M. B. Hastings, and M. Troyer. Gate-count estimates for performing quantum chemistry on small quantum computers. *Phys. Rev. A* **90**, 022305 (2014).
- [11] D-Wave Systems Inc. D-wave 2x technology review. URL [http://www.dwavesys.com/sites/default/files/D-Wave%20X%20Tech%20Collateral\\_0915F.pdf](http://www.dwavesys.com/sites/default/files/D-Wave%20X%20Tech%20Collateral_0915F.pdf). Accessed 2016-05-10.
- [12] T. F. Rønnow, Z. Wang, J. Job, S. Boixo, S. V. Isakov, D. Wecker, J. M. Martinis, D. A. Lidar, and M. Troyer. Defining and detecting quantum speedup. *Science* **345**, 420 (2014).

- [13] S. W. Shin, G. Smith, J. A. Smolin, and U. Vazirani. How "quantum" is the d-wave machine?. (2014). arXiv:1401.7087.
- [14] H. J. Kimble. The quantum internet. *Nature* **453**, 1023 (2008).
- [15] J. Clarke and F. K. Wilhelm. Superconducting quantum bits. *Nature* **453**, 1031 (2008).
- [16] D. Loss and D. P. DiVincenzo. Quantum computation with quantum dots. *Phys. Rev. A* **57**, 120 (1998).
- [17] H.-R. Wei and F.-G. Deng. Scalable quantum computing based on stationary spin qubits in coupled quantum dots inside double-sided optical microcavities. *Scientific Reports* **4**, 7551 (2014).
- [18] P. Neumann, N. Mizuochi, F. Rempp, P. Hemmer, H. Watanabe, S. Yamasaki, V. Jacques, T. Gaebel, F. Jelezko, and J. Wrachtrup. Multipartite entanglement among single spins in diamond. *Science* **320**, 1326 (2008).
- [19] J. I. Cirac and P. Zoller. Quantum computations with cold trapped ions. *Phys. Rev. Lett.* **74**, 4091 (1995).
- [20] H. Häffner, C. F. Roos, and R. Blatt. Quantum computing with trapped ions. *Physics reports* **469**, 155 (2008).
- [21] H.-J. Briegel, T. Calarco, D. Jaksch, J. Cirac, and P. Zoller. Quantum computing with neutral atoms. *Journal of modern optics* **47**, 415 (2000).
- [22] L. Isenhower, E. Urban, X. Zhang, A. Gill, T. Henage, T. A. Johnson, T. Walker, and M. Saffman. Demonstration of a neutral atom controlled-not quantum gate. *Phys. Rev. Lett.* **104**, 010503 (2010).
- [23] A. Reiserer, N. Kalb, G. Rempe, and S. Ritter. A quantum gate between a flying optical photon and a single trapped atom. *Nature* **508**, 237 (2014).
- [24] T. D. Ladd, F. Jelezko, R. Laflamme, Y. Nakamura, C. Monroe, and J. L. O'Brien. Quantum computers. *Nature* **464**, 45 (2010).
- [25] Q. A. Turchette, C. J. Hood, W. Lange, H. Mabuchi, and H. J. Kimble. Measurement of conditional phase shifts for quantum logic. *Phys. Rev. Lett.* **75**, 4710 (1995).
- [26] A. Boca, R. Miller, K. M. Birnbaum, A. D. Boozer, J. McKeever, and H. J. Kimble. Observation of the vacuum rabi spectrum for one trapped atom. *Phys. Rev. Lett.* **93**, 233603 (2004).
- [27] J. McKeever, A. Boca, A. D. Boozer, J. R. Buck, and H. J. Kimble. Experimental realization of a one-atom laser in the regime of strong coupling. *Nature* **425**, 268 (2003).
- [28] M. K. Tey, Z. Chen, S. A. Aljunid, B. Chng, F. Huber, G. Maslennikov, and C. Kurtz. Strong interaction between light and a single trapped atom without the need for a cavity. *Nature Physics* **4**, 924 (2008).

- [29] H. Zheng, D. J. Gauthier, and H. U. Baranger. Cavity-free photon blockade induced by many-body bound states. *Phys. Rev. Lett.* **107**, 223601 (2011).
- [30] S. J. van Enk and H. J. Kimble. Strongly focused light beams interacting with single atoms in free space. *Phys. Rev. A* **63**, 023809 (2001).
- [31] S. A. Aljunid, M. K. Tey, B. Chng, T. Liew, G. Maslennikov, V. Scarani, and C. Kurtsiefer. Phase shift of a weak coherent beam induced by a single atom. *Phys. Rev. Lett.* **103**, 1 (2009).
- [32] S. A. Aljunid, G. Maslennikov, Y. Wang, D. H. Lan, V. Scarani, and C. Kurtsiefer. Excitation of a single atom with exponentially rising light pulses. *Phys. Rev. Lett.* **111**, 103001 (2013).
- [33] B. Srivathsan, G. K. Gulati, B. Chng, G. Maslennikov, D. Matsukevich, and C. Kurtsiefer. Narrow band source of transform-limited photon pairs via four-wave mixing in a cold atomic ensemble. *Phys. Rev. Lett.* **111**, 123602 (2013).
- [34] B. Srivathsan, G. K. Gulati, A. Cerè, B. Chng, and C. Kurtsiefer. Reversing the temporal envelope of a heralded single photon using a cavity. *Phys. Rev. Lett.* **113**, 163601 (2014).
- [35] G. K. Gulati, B. Srivathsan, B. Chng, A. Cerè, D. Matsukevich, and C. Kurtsiefer. Generation of an exponentially rising single-photon field from parametric conversion in atoms. *Phys. Rev. A* **90**, 033819 (2014).
- [36] G. K. Gulati, B. Srivathsan, B. Chng, A. Cerè, and C. Kurtsiefer. Polarization entanglement and quantum beats of photon pairs from four-wave mixing in a cold 87 rb ensemble. *New Journal of Physics* **17**, 093034 (2015).
- [37] E. L. Raab, M. Prentiss, A. Cable, S. Chu, and D. E. Pritchard. Trapping of neutral sodium atoms with radiation pressure. *Phys. Rev. Lett.* **59**, 2631 (1987).
- [38] M. Weber, J. Volz, K. Saucke, C. Kurtsiefer, and H. Weinfurter. Analysis of a single-atom dipole trap. *Phys. Rev. A* **73**, 043406 (2006).
- [39] C. J. Foot. *Atomic physics*. Oxford University Press (2005). ISBN 9780198506966.
- [40] H. J. Metcalf and P. van der Straten. *Laser Cooling and Trapping*. Springer (1999). ISBN 0387987282.
- [41] D. J. Wineland and W. M. Itano. Laser cooling of atoms. *Phys. Rev. A* **20**, 1521 (1979).
- [42] P. D. Lett, R. N. Watts, C. I. Westbrook, W. D. Phillips, P. L. Gould, and H. J. Metcalf. Observation of atoms laser cooled below the doppler limit. *Phys. Rev. Lett.* **61**, 169 (1988).
- [43] A. Aspect, E. Arimondo, R. Kaiser, N. Vansteenkiste, and C. Cohen-Tannoudji. Laser cooling below the one-photon recoil energy by velocity-selective coherent population trapping. *Phys. Rev. Lett.* **61**, 826 (1988).
- [44] J. Dalibard and C. Cohen-Tannoudji. Laser cooling below the doppler limit by polarization gradients: simple theoretical models. *J. Opt. Soc. Am. B* **6**, 2023 (1989).

- [45] S. Chu, J. E. Bjorkholm, A. Ashkin, and A. Cable. Experimental observation of optically trapped atoms. *Phys. Rev. Lett.* **57**, 314 (1986).
- [46] J. J. Sakurai. *Modern Quantum Mechanics (Revised Edition)*. Addison-Wesley (1994). ISBN 9780201539295.
- [47] R. Grimm, M. Weidemüller, and Y. B. Ovchinnikov. Optical dipole traps for neutral atoms. volume 42 of *Advances In Atomic, Molecular, and Optical Physics*, pages 95 – 170. Academic Press, (2000).
- [48] S. A. Aljunid. *Interaction of a Strongly Focused Light Beam with Single Atoms*. PhD thesis, National University of Singapore, (2012). URL <http://www.qolah.org/publications.html#theses>.
- [49] J. Lee. *Towards Resolved-Sideband Raman Cooling of a Single  $87\text{Rb}$  Atom in a FORT*. Master's thesis, National University of Singapore, (2010). URL <http://www.qolah.org/publications.html#theses>.
- [50] N. Schlosser, G. Reymond, I. Protsenko, and P. Grangier. Sub-poissonian loading of single atoms in a microscopic dipole trap. *Nature* **411**, 1024 (2001).
- [51] N. Schlosser, G. Reymond, and P. Grangier. Collisional blockade in microscopic optical dipole traps. *Phys. Rev. Lett.* **89**, 023005 (2002).
- [52] B. Ueberholz, S. Kuhr, D. Frese, D. Meschede, and V. Gomer. Counting cold collisions. *Journal of Physics B: Atomic, Molecular and Optical Physics* **33**, L135 (2000).
- [53] S. J. M. Kuppens, K. L. Corwin, K. W. Miller, T. E. Chupp, and C. E. Wieman. Loading an optical dipole trap. *Phys. Rev. A* **62**, 013406 (2000).
- [54] R. Loudon. *The Quantum Theory of Light*. Oxford University Press, 3rd edition (2000). ISBN 0198501765.
- [55] M. Scully and M. Zubairy. *Quantum optics*. Cambridge University Press (1997). ISBN 9780521435956.
- [56] U. M. Titulaer and R. J. Glauber. Correlation functions for coherent fields. *Phys. Rev.* **140**, B676 (1965).
- [57] V. Gomer, B. Ueberholz, S. Knappe, F. Strauch, D. Frese, and D. Meschede. Decoding the dynamics of a single trapped atom from photon correlations. *Applied Physics B* **67**, 689 .
- [58] R. J. Glauber. The quantum theory of optical coherence. *Phys. Rev.* **130**, 2529 (1963).
- [59] R. J. Glauber. Coherent and incoherent states of the radiation field. *Phys. Rev.* **131**, 2766 (1963).
- [60] F. Diedrich and H. Walther. Nonclassical radiation of a single stored ion. *Phys. Rev. Lett.* **58**, 203 (1987).
- [61] K. Levenberg. A method for the solution of certain non-linear problems in least squares. *Quarterly Journal of Applied Mathematics* **2**, 164 (1944).

- [62] D. W. Marquardt. An algorithm for least-squares estimation of nonlinear parameters. *Journal of the Society for Industrial and Applied Mathematics* **11**, 431 (1963).
- [63] T. Williams, C. Kelly, et al. Gnuplot: An interactive plotting program. URL <http://sourceforge.net/projects/gnuplot>.
- [64] E. Jones, T. Oliphant, P. Peterson, et al. SciPy: Open source scientific tools for Python. URL <http://www.scipy.org/>.
- [65] M. Newville, T. Stensitzki, D. B. Allen, and A. Ingargiola. LMFIT: Non-linear least-square minimization and curve-fitting for Python.
- [66] J. J. Moré, B. S. Garbow, and K. E. Hillstom. User guide for MINPACK-1, argonne national laboratory report anl-80-74. URL <http://www.mcs.anl.gov/~more/ANL8074a.pdf>.
- [67] C. Tuchendler, A. M. Lance, A. Browaeys, Y. R. P. Sortais, and P. Grangier. Energy distribution and cooling of a single atom in an optical tweezer. *Phys. Rev. A* **78**, 033425 (2008).
- [68] A. M. Kaufman, B. J. Lester, and C. A. Regal. Cooling a single atom in an optical tweezer to its quantum ground state. *Phys. Rev. X* **2**, 041014 (2012).
- [69] G. K. Gulati. *Narrowband photon pairs from a cold atomic vapour for interfacing with a single atom*. PhD thesis, National University of Singapore, (2015). URL <http://www.qolah.org/publications.html#theses>.
- [70] A. R. McMillan, J. Fulconis, M. Halder, C. Xiong, J. G. Rarity, and W. J. Wadsworth. Narrowband high-fidelity all-fibre source of heralded single photons at 1570 nm. *Opt. Express* **17**, 6156 (2009).
- [71] M. Halder, J. Fulconis, B. Cerny, A. Clark, C. Xiong, W. J. Wadsworth, and J. G. Rarity. Nonclassical 2-photon interference with separate intrinsically narrowband fibre sources. *Opt. Express* **17**, 4670 (2009).
- [72] R. T. Willis, F. E. Becerra, L. A. Orozco, and S. L. Rolston. Correlated photon pairs generated from a warm atomic ensemble. *Phys. Rev. A* **82**, 053842 (2010).
- [73] Q. feng Chen, B.-S. Shi, M. Feng, Y.-S. Zhang, and G.-C. Guo. Non-degenerated nonclassical photon pairs in a hot atomic ensemble. *Opt. Express* **16**, 21708 (2008).
- [74] J. K. Thompson, J. Simon, H. Loh, and V. Vuletić. A high-brightness source of narrowband, identical-photon pairs. *Science* **313**, 74 (2006).
- [75] T. Chanelière, D. N. Matsukevich, and S. D. Jenkins. Quantum telecommunication based on atomic cascade transitions. *Phys. Rev. Lett.* **96**, 093604 (2006).
- [76] A. Kuzmich, W. P. Bowen, A. D. Boozer, A. Boca, C. W. Chou, L.-M. Duan, and H. J. Kimble. Generation of nonclassical photon pairs for scalable quantum communication with atomic ensembles. *Nature* **423**, 731 (2003).
- [77] R. W. Boyd. *Nonlinear Optics (Second Edition)*. Academic Press, 2 edition (2003). ISBN 0121216829.

- [78] A. Walther, A. Amari, S. Kröll, and A. Kalachev. Experimental superradiance and slow-light effects for quantum memories. *Phys. Rev. A* **80**, 012317 (2009).
- [79] H. H. Jen. Positive- $p$  phase-space-method simulation of superradiant emission from a cascade atomic ensemble. *Phys. Rev. A* **85**, 013835 (2012).
- [80] K. Liu and M. G. Littman. Novel geometry for single-mode scanning of tunable lasers. *Opt. Lett.* **6**, 117 (1981).
- [81] A. S. Arnold, J. S. Wilson, and M. G. Boshier. A simple extended-cavity diode laser. *Review of Scientific Instruments* **69**, 1236 (1998).
- [82] G. C. Bjorklund. Frequency-modulation spectroscopy: a new method for measuring weak absorptions and dispersions. *Opt. Lett.* **5**, 15 (1980).
- [83] J. L. Hall, L. Hollberg, T. Baer, and H. G. Robinson. Optical heterodyne saturation spectroscopy. *Applied Physics Letters* **39**, 680 (1981).
- [84] E. A. Donley, T. P. Heavner, F. Levi, M. O. Tataw, and S. R. Jefferts. Double-pass acousto-optic modulator system. *Review of Scientific Instruments* (2005).76(6): 063112.
- [85] C. K. Hong, Z. Y. Ou, and L. Mandel. Measurement of subpicosecond time intervals between two photons by interference. *Phys. Rev. Lett.* **59**, 2044 (1987).
- [86] H. J. Briegel, W. Dür, J. Cirac, and P. Zoller. Quantum repeaters: The role of imperfect local operations in quantum communication. *Phys. Rev. Lett.* **81**, 5932 (1998).
- [87] A. M. Dyckovsky and S. Olmschenk. Analysis of photon-mediated entanglement between distinguishable matter qubits. *Phys. Rev. A* **85**, 052322 (2012).
- [88] H. M. Meyer, R. Stockill, M. Steiner, C. Le Gall, C. Matthiesen, E. Clarke, A. Ludwig, J. Reichel, M. Atatüre, and M. Köhl. Direct photonic coupling of a semiconductor quantum dot and a trapped ion. *Phys. Rev. Lett.* **114**, 123001 (2015).
- [89] C. H. Bennett, G. Brassard, C. Crépeau, R. Jozsa, A. Peres, and W. K. Wootters. Teleporting an unknown quantum state via dual classical and einstein-podolsky-rosen channels. *Phys. Rev. Lett.* **70**, 1895 (1993).
- [90] D. Bouwmeester, J. Pan, K. Mattle, M. Daniell, A. Zeilinger, and H. Weinfurter. Experimental quantum teleportation. *Nature* **390**, 575 (1997).
- [91] F. De Martini, V. Bužek, F. Sciarrino, and C. Sias. Experimental realization of the quantum universal not gate. *Nature* **419**, 815 (2002).
- [92] M. Żukowski, A. Zeilinger, M. Horne, and A. Ekert. “event-ready-detectors” bell experiment via entanglement swapping. *Phys. Rev. Lett.* **71**, 4287 (1993).
- [93] J.-W. Pan, D. Bouwmeester, H. Weinfurter, and A. Zeilinger. Experimental entanglement swapping: Entangling photons that never interacted. *Phys. Rev. Lett.* **80**, 3891 (1998).

- [94] J. G. Rarity. Interference of Single Photons from Separate Sources. *Annals of the New York Academy of Sciences* **755**, 624 (1995).
- [95] H. De Riedmatten, I. Marcikic, W. Tittel, H. Zbinden, and N. Gisin. Quantum interference with photon pairs created in spatially separated sources. *Phys. Rev. A* **67**, 022301 (2003).
- [96] R. Kaltenbaek, B. Blauensteiner, M. Żukowski, M. Aspelmeyer, and A. Zeilinger. Experimental Interference of Independent Photons. *Phys. Rev. Lett.* **96**, 240502 (2006).
- [97] T. Legero, T. Wilk, M. Hennrich, G. Rempe, and A. Kuhn. Quantum beat of two single photons. *Phys. Rev. Lett.* **93**, 070503 (2004).
- [98] J. Beugnon, M. P. A. Jones, J. Dingjan, B. Darquié, G. Messin, A. Browaeys, and P. Grangier. Quantum interference between two single photons emitted by independently trapped atoms. *Nature* **440**, 779 (2006).
- [99] J. Hofmann, M. Krug, N. Ortegel, L. Gérard, M. Weber, W. Rosenfeld, and H. Weinfurter. Heralded entanglement between widely separated atoms. *Science* **337**, 72 (2012).
- [100] C. Santori, D. Fattal, J. Vučković, G. S. Solomon, and Y. Yamamoto. Indistinguishable photons from a single-photon device. *Nature* **419**, 594 (2002).
- [101] R. B. Patel, A. J. Bennett, I. Farrer, C. A. Nicoll, D. A. Ritchie, and A. J. Shields. Two-photon interference of the emission from electrically tunable remote quantum dots. *Nature Photonics* **4**, 632 (2010).
- [102] H. Bernien, L. I. Childress, L. Robledo, M. Markham, D. Twitchen, and R. Hanson. Two-photon quantum interference from separate nitrogen vacancy centers in diamond. *Phys. Rev. Lett.* **108**, 043604 (2012).
- [103] A. Kiraz, M. Ehrl, T. Hellerer, Ö. Müstecaplıoğlu, C. Bräuchle, and A. Zumbusch. Indistinguishable photons from a single molecule. *Phys. Rev. Lett.* **94**, 223602 (2005).
- [104] R. Lettow, Y. L. A. Rezus, A. Renn, G. Zumofen, E. Ikonen, S. Götzinger, and V. Sandoghdar. Quantum interference of tunably indistinguishable photons from remote organic molecules. *Phys. Rev. Lett.* **104**, 123605 (2010).
- [105] T. Chaneliere, D. Matsukevich, S. Jenkins, S. Y. Lan, R. Zhao, T. Kennedy, and A. Kuzmich. Quantum interference of electromagnetic fields from remote quantum memories. *Phys. Rev. Lett.* **98**, 113602 (2007).
- [106] P. Maunz, D. Moehring, S. Olmschenk, K. Younge, D. Matsukevich, and C. Monroe. Quantum interference of photon pairs from two remote trapped atomic ions. *Nat. Phys.* **3**, 538 (2007).
- [107] C. Lang, C. Eichler, L. Steffen, J. M. Fink, M. J. Woolley, A. Blais, and A. Wallraff. Correlations, indistinguishability and entanglement in hong-ou-mandel experiments at microwave frequencies. *Nature Physics* **9**, 345 (2013).

- [108] S. V. Polyakov, A. Muller, E. B. Flagg, A. Ling, N. Borjemscaia, E. Van Keuren, A. Migdall, and G. S. Solomon. Coalescence of Single Photons Emitted by Disparate Single-Photon Sources: The Example of InAs Quantum Dots and Parametric Down-Conversion Sources. *Phys. Rev. Lett.* **107**, 157402 (2011).
- [109] A. R. McMillan, L. Labonté, A. S. Clark, B. Bell, and O. Alibart. Two-photon interference between disparate sources for quantum networking. *Scientific reports* **3**, 2032 (2013).
- [110] Z. Y. Ou and L. Mandel. Derivation of reciprocity relations for a beam splitter from energy balance. *American Journal of Physics* **57**, 66 (1989).
- [111] E. Hecht. *Optics*. Addison-Wesley, 3 edition (1998). ISBN 0201838877.
- [112] D. Steck. Quantum and atom optics. URL <http://steck.us/teaching>. revision 0.10.2, 16 October 2015.
- [113] Z. Ficek and S. Swain. *Quantum Interference and Coherence, Theory and Experiments*. Springer (2005). ISBN 0387229655.
- [114] P. Nisbet-Jones. *Shaping Single Photons*. PhD thesis, University of Oxford, (2012). URL <http://www2.physics.ox.ac.uk/research/the-atom-photon-connection/other-publications>.
- [115] T. Legero, T. Wilk, A. Kuhn, and G. Rempe. Characterization of single photons using two-photon interference. **53**, 253 (2006).
- [116] T. Legero, T. Wilk, A. Kuhn, and G. Rempe. Time-resolved two-photon quantum interference. *Applied Physics B* **77**, 797 (2003).
- [117] A. Cerè, V. Leong, S. Kosen, B. Srivathsan, G. K. Gulati, and C. Kurtsiefer. Controlling the interference of single photons emitted by independent atomic sources. *Proc. SPIE* **9615**, 96150Q (2015).
- [118] V. Leong, S. Kosen, B. Srivathsan, G. K. Gulati, A. Cerè, and C. Kurtsiefer. Hong-Ou-Mandel interference between triggered and heralded single photons from separate atomic systems. *Physical Review A* **91**, 063829 (2015).
- [119] G. Grynberg, A. Aspect, and C. Fabre. *Introduction to Quantum Optics, From the Semi-classical Approach to Quantized Light*. Cambridge University Press (2010). ISBN 9780521559140.
- [120] R. Kaltenbaek, J. Lavoie, D. Biggerstaff, and K. Resch. Quantum-inspired interferometry with chirped laser pulses. *Nature Physics* **4**, 864 (2008).
- [121] R. Kaltenbaek, J. Lavoie, and K. J. Resch. Classical analogues of two-photon quantum interference. *Phys. Rev. Lett.* **102**, 243601 (2009).
- [122] N. Piro, F. Rohde, C. Schuck, M. Almendros, J. Huwer, J. Ghosh, A. Haase, M. Henrich, F. Dubin, and J. Eschner. Heralded single-photon absorption by a single atom. *Nature Physics* **7**, 17 (2010).

- [123] Y. L. A. Rezus, S. G. Walt, R. Lettow, A. Renn, G. Zumofen, S. Götzinger, and V. Sandoghdar. Single-photon spectroscopy of a single molecule. *Phys. Rev. Lett.* **108**, 093601 (2012).
- [124] J. Brito, S. Kucera, P. Eich, P. Müller, and J. Eschner. Doubly heralded single-photon absorption by a single atom. *Applied Physics B* **122**, 36 (2016).
- [125] D. Pinotsi and A. Imamoglu. Single photon absorption by a single quantum emitter. *Phys. Rev. Lett.* **100**, 093603 (2008).
- [126] M. Stobińska, G. Alber, and G. Leuchs. Perfect excitation of a matter qubit by a single photon in free space. *EPL (Europhysics Letters)* **86**, 14007 (2009).
- [127] Y. Wang, J. Minář, L. Sheridan, and V. Scarani. Efficient excitation of a two-level atom by a single photon in a propagating mode. *Phys. Rev. A* **83**, 063482 (2011).
- [128] M. Bader, S. Heugel, A. L. Chekhov, M. Sondermann, and G. Leuchs. Efficient coupling to an optical resonator by exploiting time-reversal symmetry. *New Journal of Physics* **15**, 123008 (2013).
- [129] S. Heugel, A. S. Villar, M. Sondermann, U. Peschel, and G. Leuchs. On the analogy between a single atom and an optical resonator. *Laser Physics* **20**, 100 (2010).
- [130] V. Weisskopf and E. Wigner. Berechnung der natürlichen linienbreite auf grund der diracschen lichttheorie. *Zeitschr. Phys.* **63**, 54 (1930).
- [131] C. Liu, Y. Sun, L. Zhao, S. Zhang, M. M. T. Loy, and S. Du. Efficiently loading a single photon into a single-sided fabry-perot cavity. *Phys. Rev. Lett.* **113**, 133601 (2014).
- [132] G. Zumofen, N. M. Mojarad, V. Sandoghdar, and M. Agio. Perfect reflection of light by an oscillating dipole. *Phys. Rev. Lett.* **101**, 180404 (2008).
- [133] P. Kolchin, C. Belthangady, S. Du, G.-Y. Yin, and S. E. Harris. Electro-optic modulation of single photons. *Phys. Rev. Lett.* **101**, 103601 (2008).
- [134] S. Zhang, C. Liu, S. Zhou, C.-S. Chuu, M. M. T. Loy, and S. Du. Coherent control of single-photon absorption and reemission in a two-level atomic ensemble. *Phys. Rev. Lett.* **109**, 263601 (2012).
- [135] J. D. Franson. Nonlocal cancellation of dispersion. *Phys. Rev. A* **45**, 3126 (1992).
- [136] N. Hodgson and H. Weber. *Optical Resonators: Fundamentals, Advanced Concepts, and Applications*. Springer-Verlag (1997). ISBN 978-1-4471-3597-5.
- [137] G. S. Agarwal and S. D. Gupta. Filtering of two-photon quantum correlations by optical cavities: Cancellation of dispersive effects. *Physical Review A* **49**, 3954 (1994).
- [138] R. W. P. Drever, J. L. Hall, F. V. Kowalski, J. Hough, G. M. Ford, A. J. Munley, and H. Ward. Laser phase and frequency stabilization using an optical resonator. *Applied Physics B* **31**, 97 (1983).

- [139] E. D. Black. An introduction to pound–drever–hall laser frequency stabilization. *American Journal of Physics* **69**, 79 (2001).
- [140] G. Wrigge. *Coherent and Incoherent Light Scattering in the Resonance Fluorescence of a Single Molecule*. PhD thesis, ETH Zurich, (2008). URL <http://e-collection.library.ethz.ch/eserv/eth:31016/eth-31016-02.pdf>.
- [141] I. Gerhardt, G. Wrigge, P. Bushev, G. Zumofen, M. Agio, R. Pfab, and V. Sandoghdar. Strong extinction of a laser beam by a single molecule. *Phys. Rev. Lett.* **98**, 033601 (2007).
- [142] G. Wrigge, I. Gerhardt, J. Hwang, G. Zumofen, and V. Sandoghdar. Efficient coupling of photons to a single molecule and the observation of its resonance fluorescence. *Nature Physics* **4**, 60 (2008).
- [143] V. Leong, M. A. Siedler, M. Steiner, A. Cerè, and C. Kurtsiefer. Time-resolved scattering of a single photon by a single atom. (2016). arXiv:1604.08020.
- [144] J. D. Thompson, T. G. Tiecke, A. S. Zibrov, V. Vuletić, and M. D. Lukin. Coherence and raman sideband cooling of a single atom in an optical tweezer. *Phys. Rev. Lett.* **110**, 133001 (2013).
- [145] J. Ye, D. Vernooy, and H. Kimble. Trapping of single atoms in cavity qed. *Phys. Rev. Lett.* **83**, 4987 (1999).
- [146] A. Neuzner, M. Körber, O. Morin, S. Ritter, and G. Rempe. Interference and dynamics of light from a distance-controlled atom pair in an optical cavity. *Nature Photonics* **10**, 303 (2016).
- [147] R. Maiwald, A. Golla, M. Fischer, M. Bader, S. Heugel, B. Chalopin, M. Sondermann, and G. Leuchs. Collecting more than half the fluorescence photons from a single ion. *Phys. Rev. A* **86**, 043431 (2012).
- [148] M. Fischer, M. Bader, R. Maiwald, A. Golla, M. Sondermann, and G. Leuchs. Efficient saturation of an ion in free space. *Applied Physics B* **117**, 797 (2014).
- [149] M. S. Safronova and U. I. Safronova. Critically evaluated theoretical energies, lifetimes, hyperfine constants, and multipole polarizabilities in  $^{87}\text{Rb}$ . *Phys. Rev. A* **83**, 052508 (2011).
- [150] NIST atomic spectra database. URL <http://www.nist.gov/pml/data/asd.cfm>.
- [151] P. L. Smith, C. Heise, J. R. Esmond, and R. L. Kurucz. 1995 atomic line data (r.l. kurucz and b. bell) kurucz cd-rom. URL <https://www.cfa.harvard.edu/amp/ampdata/kurucz23/sekur.html>. Accessed 2016-04-19.
- [152] C. R. Rao. *Advanced Statistical Methods in Biometric Research*. Wiley (1952).
- [153] M. N. Murthy. *Sampling: theory and methods*. Statistical Publishing Society, Calcutta (1967).
- [154] W. G. Cochran. *Sampling Techniques*. Wiley, 3rd edition (1977). ISBN 978-0-471-16240-7.

- 
- [155] H. N. Hamdan, J. L. Szarka III, and A. M. Jacks. Comparing ratio estimators based on systematic samples. *Journal of Statistical Research* **40**, 1 (2006).

